Interfacial Atomistics and Bonding Involved in Gold-Mediated Growth of Rutile Nanostructures

By

Minghui Lin

A Thesis Submitted to the Faculty of Graduate Studies of

The University of Manitoba

In partial fulfilment of the requirements of the degree of

MASTER OF SCIENCE

Department of Mechanical Engineering

University of Manitoba

Winnipeg, Manitoba

ABSTRACT

One-dimensional oxide nanostructures such as nanowires have received great attention as potential candidates for the construction of nanoscale electronic and catalytic devices because of their unique physical properties. In seed-mediated growth of oxide nanostructures, seed/oxide interfaces are essential in guiding directional growth of oxides under the seeds and require further investigation. The aim of this thesis is to study the seed/oxide interface involved in seed-mediated growth of oxide nanostructures in order to develop a better understanding of oxide growth. We selected Au/TiO_2 as the understudied system because TiO_2 nanowires have important applications in photoelectrochemical water splitting and solar cells. A systematic investigation was performed on three types of interfaces including their crystallographic orientations, atomic structure, and local bonding environment.

The Au/TiO_2 interfaces, including the interface between dewetted Au particles and TiO_2 single crystal substrates, and the interface between Au seeds and TiO_2 nanowires, were investigated using X-ray diffraction and atomic-resolved scanning transmission electron microscopy. Interface orientation relationships between Au seeds and TiO_2 nanowires, identified from selected area electron diffraction are consistent with those discovered in dewetted Au particles on TiO_2 single crystal substrates. New irrational orientation relationships were identified and were found to be promoted at temperature >800 ℃. According to their lattice structures, geometrical models, such as coincidence site lattice (CSL) and constrained coincidence site lattice (CCSL) theories, predicted the occurrence of these irrational orientation relationships with the aid of constrained lattices. These orientation relationships corresponded to various atomic structures from atomic-flat interface to significant interface reconstructions.

Another interface is the interface between an TiO_x overlayer and Au seed. A TiO_x layer with a thickness of 1-2 nm was detected on the surface of Au seeds and proved to be essential for the growth of TiO_2 nanowires. The local environment of Au at Au-TiO_x interface was further investigated with X-ray absorption spectroscopy. Au L3-edge spectra indicated Au-Au and Au-Ti bonding present at the interface, showing bonding length characteristics of Au/TiO_2 interface.

ACKNOWLEDGEMENTS

First and foremost, I owe my sincere thanks to my supervisor Prof. Guozhen Zhu for her remarkable support and guidance throughout my graduate education, without which the completion of this thesis would not be possible. In addition to her scientific expertise and open mind, she has also taught me how to discover and solve problems, which will benefit me whatever challenges I may encounter. I am very grateful to her for all the patience, encouragement and help. I would also like to thank my committee members, Prof. Derek Oliver and Prof. Chuang Deng. They have provided practical suggestions and feedback for my research project and thesis work.

My research would not have been possible without support from department of Mechanical Engineering, Manitoba Institutes for Materials, and Canadian Light Source. I would like to thank all the staff and technicians who have kindly offer assistance on my studies and research. Particularly, I would like to thank Dr. Abdul Khan and Dr. Ravinder Sidhu for assistance with TEM and SEM, Dr. Ning Chen for his invaluable suggestions and help in experiment setup and data analysis of XAS, Dr. Xinfu Gu for help in analyzing with CLS model, Dr. Wei Zhou for XRD experiment, Mr. Paul Krueger for assistance with the assembly of tube sealing system, and Dr. Lina Zhang for help with heat treatment in furnace.

I am fortunate to have met many excellent individuals during my time at University of Manitoba. Special thanks go to Yushun Liu who have spent lots of time helping and discussing with me on TEM experiment, and Wangwang Kuang and Yijian Liu for their generous assistance on many occasions. It has been a pleasure working and sharing unforgettable memories with all my treasured friends.

Finally, I would like to express my deepest gratitude to my family. Their constant and unconditional support and love have always encouraged me to try new things over the years and will also continue to inspire me in the future. I truly cherish their patience and companionship on me and wish them good luck and all the best.

TABLE OF CONTENT

LIST OF TABLES

LIST OF FIGURES

LIST OF ACRONYMS

1D	one-dimensional
2D	two-dimensional
CLS	Canadian Light Source
CSL	coincidence site lattice
CCSL	constrained coincidence site lattice
CN	coordination number
DFT	density functional theory
DW	Debye-Waller factor
FT	Fourier transform
EBSD	electron backscattered diffraction
EDX	energy-dispersive X-ray spectroscopy
EXAFS	extended X-ray absorption fine structure
FCC	face-centered cubic
FFT	fast Fourier transform
FIB	focused ion beam
HAADF	high-angle angular dark field
HRTEM	high-resolution transmission electron microscopy
LCF	linear combination fitting
NCS	near-coincidence sites
NP	nanoparticle
NW	nanowire

OR	orientation relationship
SAED	select area electron diffraction
SEM	scanning electron microscopy
SMSI	strong metal-support interaction
STEM	scanning electron microscopy
TEM	transmission electron microscopy
TPB	triple phase boundary
VLS	vapor-liquid-solid
VSS	vapor-solid-solid
XAFS	X-ray fine structure
XANES	X-ray absorption near-edge structure
XAS	X-ray absorption spectroscopy
XRD	X-ray diffraction

LIST OF SYMBOLS

a, c	lattice parameters of crystal
α	contact angle of particle
d	lattice spacing
δ	lattice misfit
δ_c	phase shift of X-ray scattering
E	energy of X-ray photons
E_0	edge energy in XAS spectrum
f	backscattering amplitude of X-rays
$\gamma_{interface}$	interface energy
γ_{metal}	surface energy of metal
γ_{oxide}	surface energy of oxide
γ_s	surface energy of substrate
γ_{vs}	vapor-solid interface energy
γ_{vl}	vapor-liquid interface energy
γ_{ls}	liquid-solid interface energy
g	reciprocal vector of a lattice plane
$h\ k\ l$	Miller indices of lattice plane
I	intensity of transmitted X-rays
I_f	intensity of fluorescence X-rays
I_0	intensity of incident X-rays
I_2	intensity of X-rays after transmitting reference foil
χ	EXAFS function

k	wave number
λ	wavelength
M	model of Au-Ti alloys
μ	absorption coefficient of X-ray
$\omega, \chi_g, \phi, \psi$	Eulerian angles for X-ray goniometer
p	mean free path of photoelectrons
R	distance between absorbing center and scattering shell
R_1, R_2	length measured in modified Wulff construction
r	Radius of particle
S_{ii}	area of growth interface
S_{iii}	area of gold-adsorbates interface
σ_j	Debye-Waller factor
θ	angle of diffraction
u v w	Miller indices of lattice direction
W_{ad}	work of adhesion
x	thickness of the sample
$\boldsymbol{X}$	transformation matrix between gold and rutile
X, Y, Z	coordination of samples in the space

Chapter 1 Introduction

1.1 Research Background

Over the past decades, rapid development of nanotechnology advances the understanding of materials' structure and properties at atomic level. Traditionally, metal oxides are widely applied in chemical sensors, catalytic reactions, energy conversion and storage, etc. because of their excellent stability, tunable bandgap, low cost, and abundant source [1–4]. When size is reduced to nanoscale, oxides show novel fascinating properties that stem from large surface area and quantum confinement effect [5]. In particular, one-dimensional (1D) nanostructures provide a confined path for the transportation of electrons and holes, giving rise to high efficiency of charge separation and collection which is desirable for electronic devices. Therefore, considerable efforts have been devoted to the fabrication of oxide nanomaterials to improve the quality and controllability of synthesizing routes.

In order to obtain 1D nanostructures, the key point is to design directional growth of target materials. One common strategy is to introduce a seed into the system which will confine the growth direction by creating a precipitation interface. This metal-mediated growth technique was first developed by Wagner and Ellis in 1964 to clarify the growth of silicon whiskers with the presence of Au impurity and was known as vapor-liquid-solid (VLS) mechanism [6]. Since then, metal-mediated growth including VLS and its analogies has been used to fabricate 1D nanostructures especially for nanowires of group IV, group III-V, and group II-VI semiconductors. Correspondingly, microscopic processes during growth are carefully examined to reveal the mass transport path from sources to growth interface. However, the success of metal-mediated growth in producing oxide nanostructures is still limited currently to a few examples such as ZnO [7–9] and SnO_2 [10,11]. In addition, the proposed growth mechanism is still controversial due to insufficient experiment evidence. Thus, further study on the growth behavior of oxide nanostructures mediated by seeds is required.

TiO_2 was chosen as the understudied system this work, because it is a representative semiconductor with broad applications in catalysis and energy-related devices. For instance, dye-sensitized solar cells were constructed with vertically aligned TiO_2 nanowire arrays [12]. Therefore, it is important to understand the growth mechanism and to fabricate TiO_2 nanowires with high quality.

1.2 Research Motivation

Despite the efforts devoted to improving the quality of metal-mediated TiO_2 nanowires, the obtained nanowires usually have irregular shape and non-uniform size. Recently, we developed a feasible approach to fabricate single-crystal TiO_2 (rutile) nanowires with uniform size and well-defined shape with tens of microns in length. We proposed a vapor-adsorbate-solid growth mechanism [13], in which Ti-O vapors generated by thermal vaporization of bulk TiO_2 were adsorbed on Au nanoparticles, transferred to the growth front via surface diffusion, and then crystallized to high-quality nanowires.

Two interfaces, the interface between Ti-O adsorbates and Au nanoparticle surface and the interface at the growth front (between Au nanoparticles and TiO_2 nanowires) determine the adsorption, diffusion, and crystallization process of growth species for TiO_2 nanowires, and therefore, are essential to the growth of TiO_2 nanowires. In spite of the importance of these interfaces, their structure information was poorly extracted, additionally weakening the proposed growth mechanism. Therefore, this work aims to study these interfaces involved in Au-assisted growth of TiO_2 nanostructures to further understand and guide the growth of TiO_2.

In order to facilitate the crystallographic analysis and atomic structure characterization of the interface at the growth front of TiO_2 nanowires, a simplified model consisting of dewetted Au nanoparticles on single-crystal TiO_2 substrates was studied. This simplified model is similar to the initial state of the growth of TiO_2 nanowires, since they were both prepared using thermal dewetting method. Accordingly, the preferential orientation relationships and atomistics at Au-TiO_2 interface were examined. Since Ti-O adsorbates might not have well-defined lattice structure, the goal of investigating Au-adsorbates interface was to extract structural information such as the first-nearest neighboring atoms and bonding configurations.

1.3 Structure of the Thesis

This thesis is organized as follows. In Chapter 2, previous work on VLS-like growth of nanowires is reviewed with an emphasis on the role of growth interface and research progress of Au-TiO_2 interface. Chapter 3 describes the experiment design of this work and the characterization techniques involved. Primary results and discussion on three Au-TiO_2 interfaces involved in the growth of TiO_2 nanostructures are presented in Chapter 4, Chapter 5 and Chapter 6. Finally, major conclusions and future outlook are summarized in Chapter 7 to give an overall view of the entire project.

Chapter 2 Literature Review

It has long been recognized that metals can be used to mediate the growth of nanowires. In order to extend our current understanding of this directional growth, it is of great importance to study the nature of interfaces involved in the growth process. In this chapter, methods based on VLS-like mechanism and the essential role of growth interfaces especially triple phase boundary are introduced in Section 2.1. Section 2.2 covers the application of VLS-like growth to oxide nanowires and current challenges in understanding corresponding growth mechanism. The research progress of interfaces in our model system, Au-TiO_2, is summarized in Section 2.3 in which the growth of TiO_2 nanowires and Au-TiO_2 interface are discussed. Finally, critical comments and research objectives are given in the end of this chapter.

2.1 VLS-Like Growth of Nanowires

2.1.1 VLS-Like Growth

Particles of element or compounds have been extensively employed in the growth of nanowires following the VLS mechanism proposed by Wagner and Ellis in 1964 [6]. In conventional VLS growth (Figure 2.1), seed particles, e.g. Au, absorb growth species from vapor precursors and form a liquid alloy. Once it is supersaturated, precipitation of growth component in the alloy takes place at liquid-solid interface, leading to directional growth of nanowires confined by the interface. In some systems, the alloy droplets may catalyze the decomposition or reaction of vapor precursors to produce the growth materials, thus the seed is also referred to as 'catalyst' in some reports. Since this catalysis effect has not been confirmed as a general rule, we will avoid 'catalyst' in this thesis and use 'seed' instead.

Over last decades, VLS has evolved to a variety of variants such as vapor-solid-solid (VSS) growth in which solid particles rather than liquid droplets are used as the seeds, and solution-liquid-solid growth where the precursors are supplied in solvent [14]. Compared to lithography, a traditional top-down technique that reduces the size of materials by carving a bulk piece into desirable nanoscale structures, VLS-like methods have following advantages: (i) smaller size of nanostructures can be achieved without limitation of beam wavelength; (ii) nanowires produced by VLS-like routes can be well-controlled in size, crystallization, growth orientations, and doping etc. by tuning experiment conditions including seeds, substrates, and growth materials [15,16].

With VLS and its analogous, a great many nanowires have been fabricated particularly for semiconductors with a wide range of applications in sensors [17], photocatalysis [18], solar cells [19], etc.

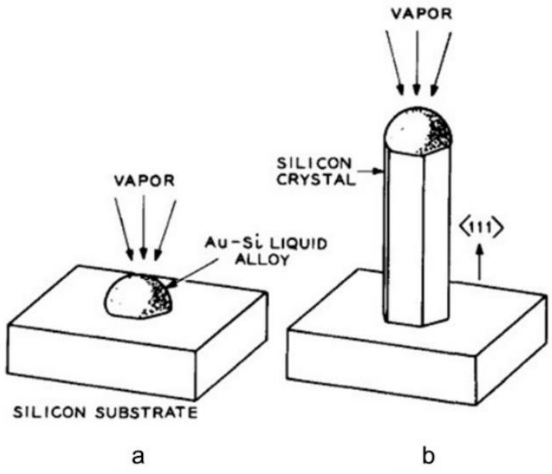

Figure 2.1 VLS growth of silicon nanowires assisted by Au on silicon substrate. Image courtesy of Wagner and Ellis [6]. Used with permission.

2.1.2 Interface at Growth Front

In order to understand the growth mechanism in VLS model, extensive research has been carried out. In a typical example of VLS, mass transfer of growth materials generally contains following steps: (i) diffusion from vapor source to seed surface; (ii) mass transport from seed surface to growth front via either surface or internal diffusion; (iii) incorporation of growth component into seed/nanowire interface where the growth of nanowires is initiated [20]. Although practical mass transfer path may vary with the state of precursors and seeds in the system, it is generally believed that growth front plays a critical role as the sink for atoms. The growth of nanowires tends to proceed in a layer-by-layer fashion of ledge flow at the interface.

Energies at growth interfaces are pivotal factors that influence the feasibility of VLS. Line tension is usually neglected for droplet larger than a few nanometers because it is typically 9-11 orders of magnitude smaller than surface tension that is on the order of 1 J/m^2 [21]. For VLS growth to be thermodynamically favorable, the increment of Gibbs free energy during growth should be negative. With the model proposed by Nebol'sin and Shchetinin, this requires the ratio between surface energies of the solid phase and liquid phase less than a critical value. Thus seed with a high surface tension favors the proceeding of VLS growth [22]. This theory is not specific to VLS but can also be used in other analogous models.

When solid particles are used as the seeds, seed/nanowire interface has more constraints on the orientation and grow rate of nanowires. VSS has been successfully applied to several systems including $TiSi_2$-mediated growth of Si nanowires [23], Pd_2Si-mediated growth of Si nanowires [24], η′-Cu_3Si-mediated growth of Si nanowires [25], $CoSi_2$-mediated growth of Si nanowires [26], $AlAu_2$-mediated growth of Si and Ge nanowires [27], etc. In these studies, interfacial epitaxial relationships between solid seeds and nanowires were observed, which determined the growth directions of nanowires. For the case with low-symmetry at the interface, e.g. η′-Cu_3Si-Si interface, η′-Cu_3Si particles with different orientations could change the growth direction of Si nanowires accordingly. For ZnO, Sn seeds were successfully used to guide the growth of ZnO nanowires in $[0001]$ direction and ZnO nanobelts in $[01\bar{1}0]$ and $[2\bar{1}\bar{1}0]$ directions corresponding to various interfacial orientation relationships [7]. If lattice mismatch existed between the particles and nanowires, interface defects were produced which might slow or halt the propagation of ledge.

On account of its importance in nanowire growth, the morphology and structure of growth interface have been investigated in several systems. However, in VLS growth the migration of ledge is too fast to be captured so that it can only be confirmed by a flat growth front [22,28,29]. In VSS growth, the propagation rate of ledges is much lower than that of VLS, thus they can be well-resolved from in situ environment TEM. Nonetheless, there still remains discrepancies in the step height and occurrence of interface ledges for VSS. For example, for Si nanowires aided with Pd_2Si, the steps at the growth front were as large as ~10 Si$\{111\}$ spacing and multiple ledges were observed simultaneously. While in the case of η′-Cu_3Si, the ledge was comparably one Si$\{111\}$ bilayer and multiple-ledge growth was rarely observed. In addition, the interaction between seeds and nanowires at the interface is also far less examined. Akiyama et al. performed *ab initio* study on the formation of wurtzite structure rather than zinc blende in Au-mediated growth of GaAs nanowires on GaAs-(111)B substrates [30]. They proposed that Au atoms could incorporate into the interstitial sites of interfacial GaAs layers and stabilize the wurtzite structure through hybridization with interfacial As atoms. In Sakong's DFT atomistic modelling of Au seed-GaAs nanowire interface, incorporation of Au was not found in relaxed interface configurations.

However, no experiment evidence has been reported so far to confirm the atomic structure of Au-GaAs interface in VLS growth. Therefore, investigations on the structure of seed-nanowire interface are desired in order to further reveal the characteristics and mechanism of VLS-like growth.

2.1.3 Triple Phase Boundary

At seed/nanowire interface, triple phase boundary (TPB) has attracted great interest due to its essential role in nucleation and growth. Assuming two-dimensional (2D) nuclei on various interfaces in a VLS system, changes of Gibbs free energy during nucleation, which were determined by supersaturation and interface energies involved, were estimated by Wacaser et al [31]. According to their work, nucleation at TPB could achieve minimization of Gibbs free energy by adjusting the shape and position of the nucleus. Thus nucleation at TPB was more energetically favored compared to seed surface or crystal surface, promoting 1D growth of nanowires while suppressing lateral growth [32,33]. Additionally, if the interface in the vicinity of TPB was rough, preferential incorporation of atoms on interface steps or kinks also occurred due to lower supersaturation required for crystal growth [31]. This effect of TPB was also found in nucleation of ice from water on foreign particles where nucleation rate at TPB was orders of magnitude higher than that at other surfaces or interfaces [32].

On the other hand, force balance at TPB also influences the shape of nanowires. For an initially flat interface, unbalanced force at TPB drives the rise of droplet, leading to the contraction of cross section of the nanowire. Similarly, this effect sometimes caused a truncated morphology of growth interface in which additional edges were observed near TPB [34]. Another common feature of VLS grown nanowires is tapered bases at the bottom of nanowires. With the assumption of fixed volume for the droplet, Dubrovskii calculated the increase of surface energy in forming a monolayer at Au-GaAs interface corresponding to various contact angles at triple junction and found that narrowing monolayer had the lowest surface energy when contact angle was small, giving rise to a tapering shape at the initial stage of nanowire growth [35]. This is consistent with the triangular bases observed in Au-assisted GaAs nanowires [33]. In the aspect of surface tension, balance of surface force at TPB also causes the shrinking of diameter at the beginning of growth [21]. Figure 2.2 shows an example of Si nanowires with a tapered base. Although models based on diffusion of adatoms on substrate and nanowire surface have been suggested as well to account for the pyramid bases at nanowire bottom [36,37], they are usually for long nanowires where the bases are mainly contributed by appreciable adatom flux.

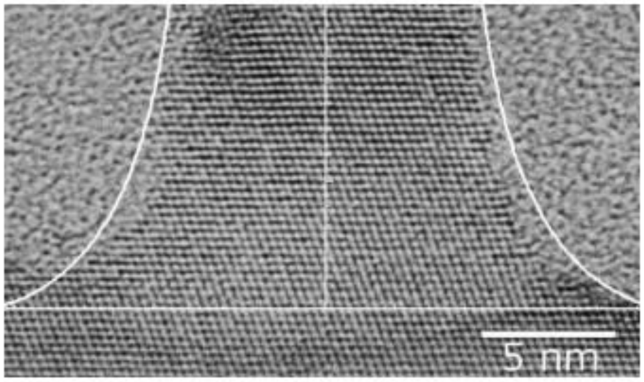

Figure 2.2 Base of a Si nanowire grown by VLS method. The white line is calculated shape from balance of surface tension at TPB [21]. Used with permission.

It is worth noting that the growth of pyramid-like bases under Au seeds was also observed in oxide supported Au particles after annealing at high temperature. A typical example of Au-$MgAl_2O_4$ is shown in Figure 2.3 [38]. However, despite the resembling shape, the formation of these oxide bases is different from those in VLS growth. Since no Mg, Al, and O atoms were found in Au particles, the growth of $MgAl_2O_4$ nanostructures mainly originated from surface diffusion of $MgAl_2O_4$ substrates instead of VLS growth. Reconfiguration of oxide surface at the triple junction with a metal liquid was also reported for Cu droplets on single-crystal Al_2O_3 substrates [39]. This phenomenon is similar to the grooving of grain boundaries. At initial state, elastic stress is introduced in the substrate to balance the force at TPB. After annealing treatment is applied, mass diffusion of substrate becomes significant, resulting in the formation of ridge at the triple line [40,41]. In particular, an interfacial bilayer consisting of mixed Au and $MgAl_2O_4$ was observed at the interface accompanying with twins in Au particles [38]. Therefore, a twin-assisted growth mechanism was proposed to explain the growth of $MgAl_2O_4$ bases [42]. Briefly, at the intersect of twin planes and $MgAl_2O_4$ substrates, steps are generated from which the interfacial bilayer starts and extends to $MgAl_2O_4$ lattice. The regrowth of $MgAl_2O_4$ substrates is thus facilitated by lateral growth of interfacial layer and migration of these steps.

Similar temperature-induced growth of oxide nanostructures was also reported in another lattice-matched metal-oxide system, Au-$SrTiO_3$ (lattice parameter is 4.078 Å for Au, and 3.905 Å for

$SrTiO_3$) [43]. Likewise, $SrTiO_3$ bases with a height of ~20 nm were found under Au particles. The growth mechanism of oxide bases in both Au-$MgAl_2O_4$ and Au-$SrTiO_3$ systems was evaluated from aspects of energy in which the reduction of total energy, mainly originating from changes of Au surface and interface, was assumed to compensate the increased surface energy of oxide bases during growth. Accordingly, the estimated height of oxide bases was consistent with experiment measurement, confirming the validity of the predictions. Although the growth mechanism of these $MgAl_2O_4$ and $SrTiO_3$ bases is not VLS, it is shown that for metal-mediated growth of nanostructures, growth behavior is closely related to the structure of growth interface and TPB.

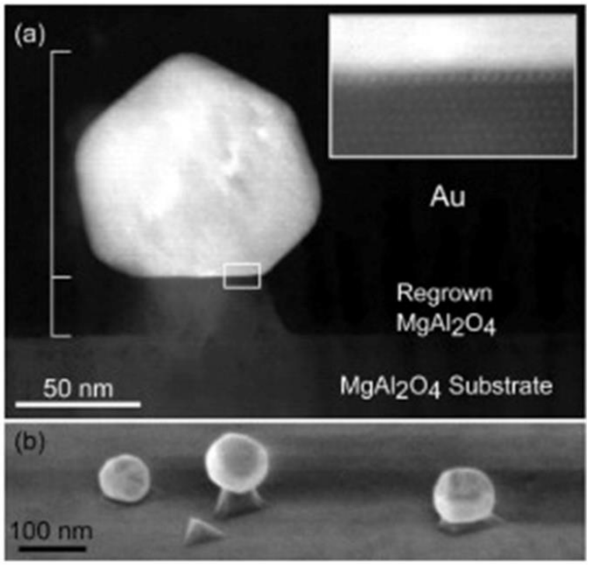

Figure 2.3 Regrowth of $MgAl_2O_4$ bases under Au. (a) STEM image of regrown $MgAl_2O_4$ nanostructure under Au particle with Au- $MgAl_2O_4$ interface inserted. (b) SEM image of dewetted Au particles on $MgAl_2O_4$ substrate. Image courtesy of Majdi et al. [38]. Used with permission.

2.2 VLS-like Growth of Oxide Nanowires

Although great success has been achieved in the application of VLS-like methods to Si and Ge nanowires, the growth of compound nanowires especially oxides is limited with much more complex mechanism. On the one hand, dissolution of compounds is different from elemental nanowires. Many binary compounds may not form ternary liquid alloys with seeds except for GaAs which has a pseudobinary phase diagram with Au [44]. Instead, it is commonly encountered that only one component of the compounds can be detected in the seeds. For group III-V materials, this is generally group III element [16]. While for oxides such as ZnO, O is rarely detected in the seeds [9]. In general, the concentration of O is low in Au (10^{-13} at 400 K, and 10^{-5} at 1000 K [45]). This increases debates on how O is incorporated into the growth front. On the other hand, the formation of liquid alloy does not necessarily mean the growth of nanowires progresses in a VLS-like manner. Therefore, the nature of multi-component systems needs to be taken into account to clarify the precipitation of compounds. However, thermodynamic data of multi-component systems such as ternary phase diagrams is limited, which impedes the development of growth theory for oxide nanowires.

Notwithstanding the issues in the growth of oxide nanowires, a few attempts have been made to explain the mass transfer path in seed-assisted growth of oxide nanowires, but mechanisms reported are varied in different systems. Oh et al. investigated the growth of Al_2O_3 nanowires with Al as the seed [46]. From in situ experiment, oscillating growth and dissolution were observed for the edge facets near TPB throughout the entire growth. They proposed that in continuous growth of Al_2O_3 nanowires, Al was provided by the Al seeds and O atoms diffused from TPB into the interfacial layer to accomplish the growth. In addition, Au-assisted VLS growth of ZnO nanorods was also studied by Hejazi et al [47]. Considerable amount of Zn was present in the droplet, indicating that incorporation of Zn to growth front likely occurred through bulk diffusion in alloy seeds. They believed that Zn islands were formed at Au/Zn-ZnO interface and oxidized by CO/CO_2 mixture that diffused across the interface. However, in another work where ZnO nanowires were prepared with similar carbothermal method, energy-dispersive X-ray spectroscopy (EDX) analysis showed that Zn was not found in the particles except on the surface. Thus they proposed that Zn atoms in the vapor were transported to TPB by forming a liquid Au/Zn layer on Au surface. With dissociated O_2, ZnO nucleus formed at the periphery of Au-ZnO interface and grew laterally with ledge mechanism [48]. For TiO_2 nanowires on sapphire substrates, VLS growth was only allowed in a narrow materials flux window compared to other MgO and SnO_2 [49]. These results show that the growth of oxide nanostructures and corresponding mechanisms are very sensitive to specific growth conditions such as vapor pressure even if similar approach is applied. If more complex oxides are involved such as transparent indium−tin oxide (ITO), the growth process could be even more complicated with competing nucleation events at the interface [50]. Considering the wide range of oxides, it is difficult to establish a general theory for the growth of oxide nanowires at present. For individual case, direct evidence such as interface structure still lacks to confirm the fundament processes of oxide growth, e.g. the transport of metal and oxygen atoms.

2.3 Au-TiO_2 Interface

Among the oxide nanowires that have been synthesized with VLS-like growth, interest in TiO_2 has been stimulated by its potential applications such as gas sensing [51]. Although success of seed-mediated growth has been achieved for TiO_2 in some cases, corresponding growth mechanism is far from well understood due to limited experiment evidence. In spite of the observation of seeds at nanowire tip, it is not appropriate to conclude that VLS mechanism is responsible for the growth without detailed characterization of the nanowires [52–54]. For some studies that provided the composition of seed particles, both Au-Ti alloy and pure Au were reported in the absence of other information that could confirm the growth process [55,56]. Particularly, it was found that P impurities in the furnace could promote the growth of TiO_2 nanowires assisted with Ni. Amorphous materials containing Ti and O were observed on the surface of Ni_3P shell that coated Ni seeds. Thus they proposed the growth of TiO_2 nanowires originated from the adsorption, diffusion, and reaction of Ti and O on the shell [57]. This special case is obviously different from conventional VLS growth with the unexpected influence of P. These studies suggest multiple possibilities for the growth of TiO_2 nanowires with the assistance of seeds, but the formation of TiO_2 from Ti and O sources, which is linked to mass transport at interfaces between seeds and vapor/nanowires, is still unanswered.

In this work, we chose Au, the most commonly used seeds in the VLS growth of nanostructures because of its inertness and stability as the seed element and focused on the structure and chemistry of Au-TiO_2 interface. The important characteristics of Au-TiO_2 interface in the literature are reviewed including the crystallographic orientation relationship, atomistics, and interactions between Au and TiO_2.

2.3.1 Au and TiO_2

Au is a noble metal with an atomic number of 79. It has face-centered cubic (FCC) structure with a lattice parameter of 4.078 Å at room temperature. The surface energy of gold depends on the arrangement of atoms in the surface plane. Surfaces with lowest energy are (111), (100), and (110) corresponding to energies of 1.283 J/m^2, 1.627 J/m^2, and 1.700 J/m^2 as given by Vitos [58].

Although exact values in the references can be varied depending on methodology [59], this trend remains the same.

As for TiO_2, it has three major polymorphs including anatase, rutile and brookite. Among them rutile is the most stable phase, belonging to tetragonal system with a space group of P42/mnm. Lattice constants of rutile adopted here are 4.594 Å for *a* and 2.959 Å for *c* [60]. Each Ti atom is six-fold coordinated in an octahedral unit of O. In rutile, The energy of low-index terminations follows (110)<(100)< (101)<(001)[61]. (110) surface has the lowest energy with experiment values in the range of 0.28-0.38 J/m^2, while theoretical energies can be overestimated due to sensitivity to lattice relaxation [62,63]. In this study, we used 0.33 J/m^2 for TiO_2 (110) following Sivaramakrishnan et al [64]. The unit cells and most stable surfaces of the two crystals are shown in Figure 2.4.

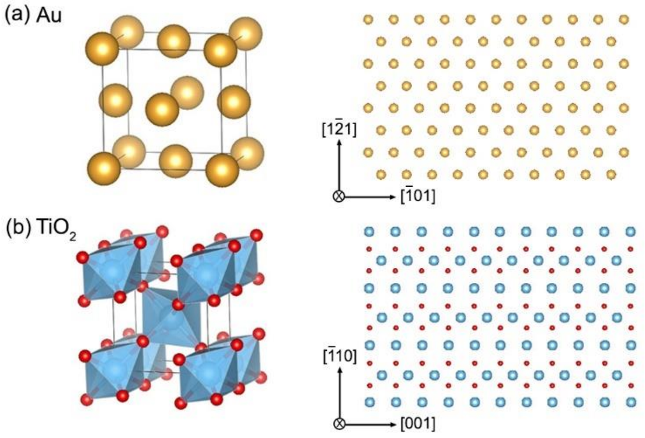

Figure 2.4 Atomic models of Au and TiO_2. (a) Unit cell of gold and (111) plane. (b) Unit cell of rutile and (110) plane.

2.3.2 Interface Orientation Relationship

Au-TiO_2 interface can be obtained by a variety of methods including deposition-precipitation, ion implantation, and vacuum deposition. The epitaxy orientation relationship (OR) between Au and TiO_2 was reviewed by Cosandey [65]. To date, there are in general four types of OR reported in the literature. They are designated as ORa, ORb, ORc, ORd herein and listed as follows:

ORa: $\{111\}_{Au}//\{110\}_{TiO_2}, \langle 1\bar{1}0\rangle_{Au}//[001]_{TiO_2}$

ORb: $\{112\}_{Au}//\{110\}_{TiO_2}, \langle 1\bar{1}0\rangle_{Au}//[001]_{TiO_2}$

ORc: $\{001\}_{Au}//\{110\}_{TiO_2}, \langle 1\bar{1}0\rangle_{Au}//[001]_{TiO_2}$

ORd: $\{110\}_{Au}//\{110\}_{TiO_2}, \langle 1\bar{1}0\rangle_{Au}//[001]_{TiO_2}$

It is noteworthy that for some particles, their ORs are different from the ORa-ORd above, but detailed index or information of their ORs is not given by authors. Besides, it is possible that the ORs above can be found between Au and TiO_2 but the interface plane is not flat $TiO_2(110)$ [66]. The existence of these uncertain ORs is not summarized here. ORs identified from experiment observations mainly come from two sources: (i) direct identification of OR from TEM characterization on individual Au particles; (ii) OR analysis with electron backscattered diffraction (EBSD) or X-ray diffraction (XRD) for a large number of particles. Among these known ORs, ORa is the most common one at Au-TiO_2 interface regardless sample preparation and treatment procedures. In contrast, few examples of ORb-ORd have been reported. ORb and ORd were found in direct deposition of Au on TiO_2 with higher substrate temperature for ORb [64,67], while ORc was reported in Au/TiO_2 catalyst prepared by deposition-precipitation method with aqueous $HAuCl_4$ solution and TiO_2 powder [68]. Besides, implantation of Au^{2+} into $TiO_2(110)$ followed by annealing at 1275 K in air for 10 h could produce embedded Au clusters in TiO_2. ORa-ORd were observed on the edge of Au clusters [69]. It is worth noting that all these four ORs correspond to low-index lattice planes at the interface. One possible reason for lack of high-index ORs in experiment might be the small size of Au clusters or particles involved in most studies due to their high catalytic activity [70]. Nanocrystals of a few nanometers in size might not be enough to form an interface with high-index OR.

Although it is still not clear whether sample preparation method has direct correlation with preferred ORs at Au-TiO_2 interface due to limited data, temperature effect on the distribution of ORs has been supported by a few studies. For Au clusters deposited on $TiO_2(110)$ at room temperature, Shibata discovered ORd for clusters <3 nm in size, most of which were coherently attached to TiO_2. As size increased, interface coherence was lost with new ORs although they could not be exactly determined [67]. In contrast, in Sivaramakrishnan's study, annealing at temperature >500 °C for more than 2 hours was additionally applied to as-deposited sample. As a result, particles within the range of 4-11 nm had an ORa epitaxy with rutile support, and the interface maintained coherent for all particles [64]. This difference between the two studies indicates that ORa is likely closer to equilibrium state than ORd.

In addition, Cosandey et al. investigated the influence of substrate temperature on ORs by examining two samples deposited at different temperature with EBSD as shown in Figure 2.5 [71]. For the first sample, Au films were deposited at 300 K followed by annealing in vacuum at 775 K for 1 hour. For the second sample, Au films of 12 nm were directly deposited to TiO_2 substrate that was maintained at 775 K. From the pole figure, most Au particles in the first sample were orientated at ORa. The scattering of poles indicates a deviation of in-plane orientations. While for the second sample, ORb was observed from the EBSD pattern in which Au(112) is parallel to TiO_2(110). Besides, twins in Au particles were also observed in both samples.

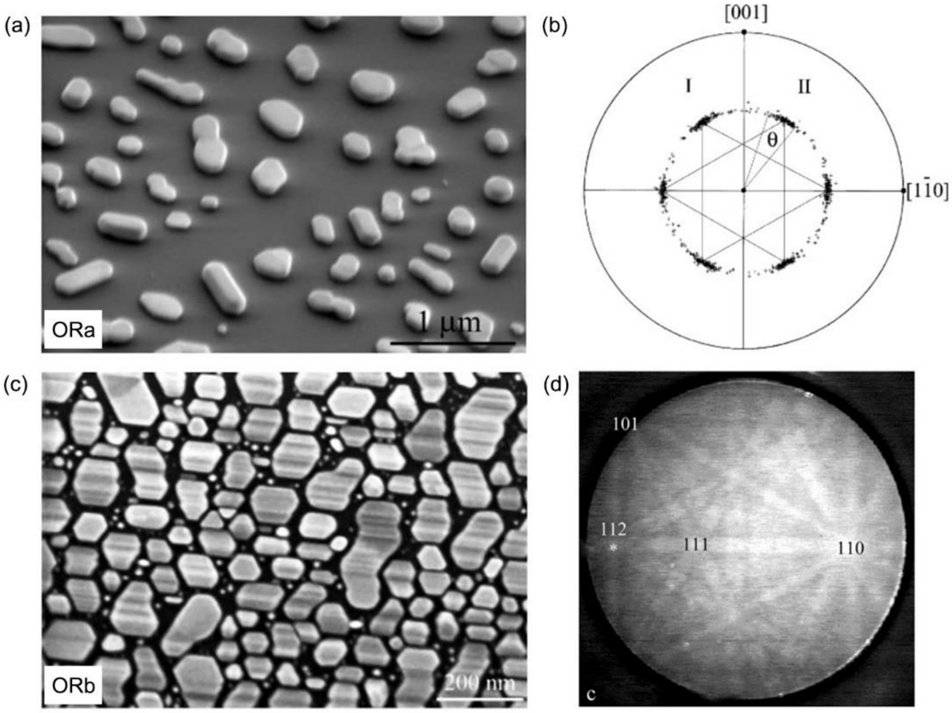

Figure 2.5 Dewetted Au particles on TiO_2 substrates at different deposition and annealing conditions. (a)-(b) Gold particles and corresponding $\{111\}$ pole figure of sample prepared by room temperature deposition and annealing at 775 K. (c)-(d) Morphology and EBSD of ORb particles that were obtained from direct deposition at 775 K. Modified from Cosandey et al. [71]. Used with permission.

The evolution of ORs with annealing temperature was additionally studied by Chen et. al [72]. Well-defined ORa was observed after annealing at 750 ℃. With temperature rising from 200 ℃ to 750 ℃, the intensity of Au(222) peak in in situ reflection high-energy electron diffraction was continuously increased, indicating the enhancement of interface epitaxy at high temperature. However, for thin Au films with thickness <0.1 nm, the intensity of Au diffraction dropped or even appeared at >730 ℃. Although this unusual behavior may be attributed to melting or sublimation of Au nanocrystals, it has not been well elucidated thus far.

However, the effect of temperature on OR evolution does not necessarily hold true. For Au islands growing on $TiO_2(110)$ substrates, ORa and ORb were detected by in situ grazing incidence small-angle X-ray scattering at 300 K and 600 K. The ratio of the two ORs was nearly 1:1, which was not affected by the temperature [73].

Despite the experiment evidence of various ORs, rare analysis has been carried out to understand the nature of preferred ORs at Au-TiO_2 interface. To estimate possible preferential ORs, Akita and coauthers performed coincidence of reciprocal lattice point calculation on Au and TiO_2 (rutile) lattices. In detail, the reciprocal lattice points were constructed for the two crystals and replaced with a sphere [74]. With rutile lattice fixed, gold was rotated about two axes. i.e. a and c direction of rutile, from 0° to 90° respectively. At each orientation, the total volume of overlap in spheres, which represented the degree of good matching between gold and rutile, was calculated and assigned to corresponding rotation angle. In this way, a three-dimensional diagram including overlapped volume and two angles in space was created. There were many peaks in the diagram, each of which corresponded to an OR with good match and thus possibly a preferred OR. Although the exact indices of these ORs were not given, nor were they observed in TEM experiment, these results suggest the existence of other preferential ORs at Au-TiO_2 interface in addition to the known ORa-ORd.

2.3.3 Interface Atomistics

The atomic structure of stoichiometric 1×1 rutile(110) surface is illustrated in Figure 2.6. Rows of fivefold-coordinated Ti atoms (Ti_{5C}) and twofold protruding bridging O atoms (O_b) along $[001]$ direction alternate to form $TiO_2(110)$ surface. These undercoordinated atoms can be easily removed by thermal annealing, resulting in a reduced 1×1 surface with vacancy defects. In the first layer, major relaxation occurs along the perpendicular direction except for in-plane oxygens that may move laterally [75]. Surface Ti and O can also reconstruct to new configurations, some of which include add-row Ti_2O_3 1 × 2 reconstruction, TiO 1 × 2 reconstruction, and Ti_2O 1 × 2 reconstruction [76,77].

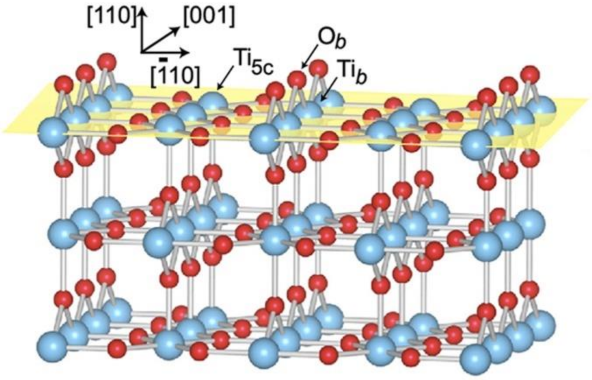

Figure 2.6 Ball-and-stick model of stoichiometric rutile (110) surface. Figure adapted from Moses et al. [78]. Used with permission.

The interface between Au and TiO_2 depends on the lattice planes of both crystals. Considering ORa is the most common orientation relationship thus far, the interface between Au(111) and TiO_2(110) has been extensively studied. Density functional theory (DFT) calculations were performed by Yu et al. to predict the structure and adhesion energy of Au-TiO_2 interface for different TiO_2 terminations [76]. As shown in Figure 2.7, for stoichiometric TiO_2(110), a separation between interfacial Au and Ti-O layer exists after relaxation with a distance of 3.90 Å between Au and Ti layers, and 2.63 Å between Au and bridging-O layers. These spacings change to 2.79 Å for Au-Ti and 2.70 Å for Au-O (in-plane) in reduced TiO_2 with a much higher adhesion energy. If various Ti and O rows are removed on TiO_2 surface, reconstruction configurations can be introduced. A principal characteristics of these reconstructed interface is the position of Au in interfacial layer. Au atoms sit at the vacant sites surrounded by Ti and O, resulting in a mixed layer of Au, Ti, and O. Simultaneously, interplanar distance between Au and Ti-O layer is further reduced. According to their calculations, Au(111)-reduced TiO_2(110) interface has the largest adhesion energy, but it has not been confirmed experimentally. In terms of reconstructed interface, TiO reconstruction is the most stable one with interface separation of 2.45 Å and adhesion work of 29 meV/Å^2.

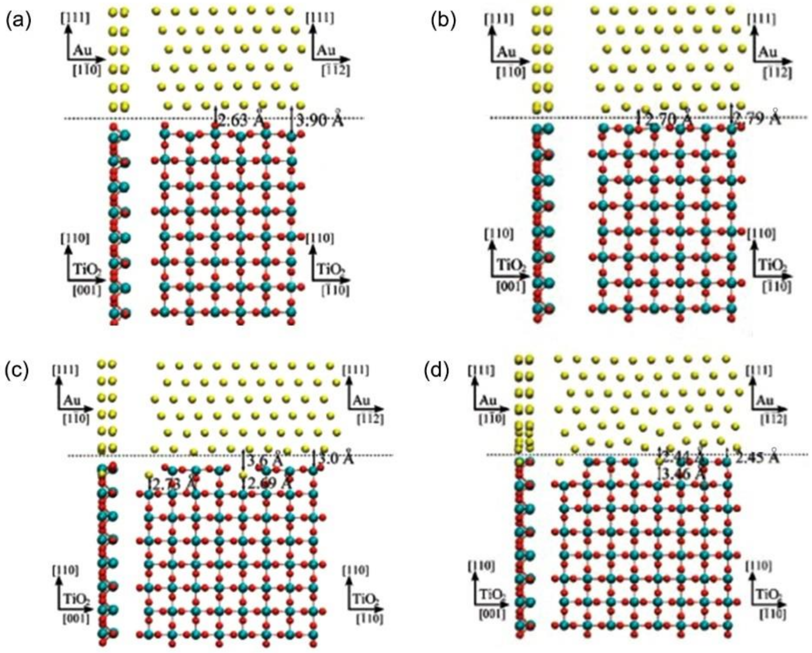

Figure 2.7 Atomistics of four types of ORa Au-TiO_2 interfaces. (a) Au(111) on stoichiometric TiO_2(110) surface after relaxation. (b) Au(111) on reduced TiO_2(110) surface after relaxation. (c) Au(111) on add-row reconstructed TiO_2(110) surface after relaxation. (d) Au(111) on TiO reconstructed TiO_2(110) surface after relaxation. Adapted with permission from [76]. Copyright (2020) American Chemical Society.

To confirm the atomic structure of Au-TiO_2 interface, atom-resolved imaging techniques such as high-resolution transmission electron microscopy (HRTEM) and scanning transmission electron microscopy (STEM) have been utilized especially when aberration is corrected. ORa interface with stoichiometric TiO_2 was reported as confirmed by the bridging O atoms in HRTEM and the 0.33 nm distance between Au and Ti layers [79,80]. Gao et al. used depth sectioning to confirm the existence of Au atoms in the interfacial layer by recording STEM-HAADF images at a series of focus [81]. Through analysis of intensity profiles, they showed that observed interface was in line with the added-row reconstruction model with a measured interfacial distance of 2.35±0.16 Å. However, instead of replacing all Ti atoms as in the calculated model, most interfacial columns along TiO_2[001] only had 1-8 Au atoms embedded. A shift upward or downward by 92.4±40 pm was also observed for the interfacial layer.

ORb interface was reported in [65]. Despite the limitation of resolution which made it difficult to identify individual atoms at the interface, the distance between topmost Au and Ti-O layer was measured as 0.327 nm if bridging O was neglected. The authors proposed an atomic model of the interface in which Au atoms sat on the top of Ti_{5c} atoms and are locked between O rows.

As for ORc interface, interfaces were constructed with both stoichiometric and reduced $TiO_2(110)$ [76]. For defect-free TiO_2 surface, the interfacial distance is 3.63 Å between Au and Ti layers, and 2.33 Å between Au and O. For reduced surface, the distances were decreased 2.64 Å and 2.55 Å. This influence of reduced substrate is analogous to the characteristics of ORa.

ORd interface was also calculated with a model of nine-layer Au on reduced $TiO_2(110)$ [67]. Mixing of Au and Ti-O was not observed with only slight lateral relaxation of first Au layer. Although the distance between Au and Ti layer was not given, it could be roughly estimated to be ~2.66 Å from electron density profiles across the interface.

2.3.4 Interface Chemistry

One important issue concerns the bonding between Au and TiO_2 at the interface, i.e. which atom in Ti and O forms a stronger bond with Au. For atomic oxygen, the bonding of oxygen on Au is weak as evidenced by the endothermic dissociation of O_2 on stepped Au (211) surface [82]. This weak bonding is mainly caused by two effects: (i) higher occupation of antibonding orbitals due to low energy of d-bands in Au; and (ii) Pauli repulsion between valence state of oxygen and d states of Au [83,84]. When Ti and O coexist, i.e. at Au-TiO_2 interface, the situation is more complicated. For Au clusters supported on single-crystal TiO_2 support, the surface of TiO_2 has great influence on the nature of interface bonding. On stoichiometric TiO_2 surface, Au binds with bridging O with a weak interaction. The distance of Au-O and the shortest distance between Au and Ti were ~2.2 Å and 3.9 Å respectively as given by Liu [85]. On reduced TiO_2, Au clusters prefer to nucleate and growth at vacancy sites of bridging O, and the bond tends to be covalent. Adsorption of single Au atom on TiO_2 showed that adsorption on vacancies was 0.45 eV more stable than on top of bridging O in defect-free TiO_2, and 0.8 eV more stable than on top of fivefold coordinated Ti [86]. However, in some systems, Au-O bonding was also detected. For instance, from X-ray absorption spectrum of Au L3 edge, Au-containing complexes, $Au(CH_3)_2(C_5H_7O_2)$, adsorbed on TiO_2 powder surface by Au-O with a coordination number of 2 and a distance of 2.16 Å [87].

In addition, the state of Au at Au-TiO_2 interface is also subject to debates. There are a variety of experiment conditions that may influence the chemical states of Au such as substrate conditions, atmosphere, particle size and temperature. On a reduced TiO_2 surface, Au at the vacancy sites binds strongly with the nearby cations of Ti and excess charge is transferred from TiO_2 to Au, resulting negatively charged Au species ($Au^{\delta-}$). In contrast, an oxidized surface leads to electron transfer from Au to TiO_2 and consequently cationic Au exists ($Au^{\delta+}$) [88]. Strong Au-O bond forms through hybridization of Au 5d and O 2p orbitals [85]. On stoichiometric surface, charge transfer is negligible at Au-TiO_2 interface, corresponding to a small adhesion energy [89,90].

A special interaction between Au and TiO_2 is the strong metal-support interaction (SMSI). To account for the suppression of H_2 or CO adsorption of metal-support catalyst after reduction treatment at high temperature, SMSI was proposed and studied since 1970s [91]. Although SMSI effect has been discovered for a few noble metals (e.g. Pt and Ru) and transition metal oxides (e.g. TiO_2, CeO_2) for a long time, direct evidence of SMSI in Au/TiO_2 was not reported until in 2017 by Tang et al [92]. This suppression of molecule adsorption is attributed to encapsulation of TiO_x overlayer on Au caused by migration of reduced TiO_2 to Au surface. As presented in Figure 2.8, encapsulation layer can be observed on the surface of Au after reduction treatment at 500 °C. Electron energy loss spectra (EELS) confirm the existence of Ti^{3+} in the layer. SMSI is sensitive to sample preparation history. When melamine was used to modify Au followed by pretreatment in nitrogen, TiO_x encapsulation layer could also be formed. However, this layer was different from classic SMSI with permeability to reactants and stability under oxidative conditions [93].

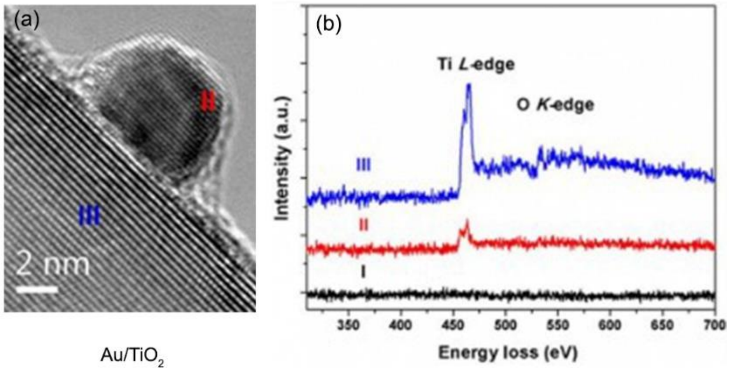

Figure 2.8 Encapsulation layer in Au-TiO_2 system. (a) HRTEM image and (b) EELS spectra of Au/TiO_2 sample after being reduced by H_2 at 500 °C for 1 hour. From [92]. Reprinted with permission from AAAS.

In SMSI, metal-metal bond forms between Au and cations of Ti with charge transfer at the interface. For classic SMSI generated by reduction in H_2 atmosphere or Ti^{3+} reduction in wet-chemical approach, electrons were transferred from TiO_x overlayer to Au at the interface. Therefore, negatively charged Au species ($Au^{\delta-}$) were detected in addition to metallic Au (Au^0) [94]. While in oxidized conditions, electrons transfer from Au to TiO_2 was observed [93]. Liu et al. used X-ray photoelectron spectroscopy to investigate charge transfer at Au-TiO_2 interface when exposed to an alternating atmosphere of H_2 and O_2 [95]. The percentage of $Au^{\delta+}$ species increased when being pre-treated with H_2 and decreased with O_2. In addition, this oscillation of charge states also varied with temperature and the crystal plane of TiO_2 surface. For treatment at 250 ℃ and 300 ℃, oscillation of the percentage of $Au^{\delta+}$ was significant for TiO_2 $\{100\}$ and $\{101\}$, while it was much more stable for Au/TiO_2 $\{001\}$. For higher temperature at 350 ℃, irreversible encapsulation, which is different from classic SMSI, occurred for Au/ TiO_2 $\{100\}$ and Au/ TiO_2 $\{101\}$ with a stable $Au^{\delta+}$. Despite the appearance of oscillating $Au^{\delta+}$ in Au/ TiO_2 $\{001\}$ at the same temperature, no encapsulation layer was observed. Thus SMSI is also influenced by crystal plane of TiO_2.

2.4 Critical Comments and Research Objective

As the sites where nucleation and growth take place, the interface between seeds and grown nanostructures has been proven to play a crucial role in the diffusion and incorporation of growth units. However, the nature of this interface during growth has been far less investigated in metal-oxide systems. For our model system, Au-TiO_2, the interface is incommensurate due to the mismatch of lattice symmetry and constants. This increases the complexity of interface structure. Although Au-TiO_2 interface has been examined in the literature regarding crystallography, atomisitcs and chemistry, it shows strong dependence on sample preparation methods and treatment history. In addition, experiment evidence is still insufficient to confirm the rationality of theoretical calculations in the literature. Therefore, refinement of realistic Au-TiO_2 interface needs to be performed to gain better understanding of the growth of TiO_2 nanowires.

In the present work, TiO_2 nanostructures were fabricated on TiO_2 substrates via thermal growth with Au particles as the seeds. After applying heat treatment of various temperature and time, two types of rutile nanostructures were obtained under gold seeds including short rutile bases and long rutile nanowires. Our objective is to investigate the Au-TiO_2 interfaces in these samples which may share similar features. Preferential ORs, atomic structures and local bonding status of these interfaces as well as the growth of nanowires were examined in detail.

Chapter 3 Experiment Design and Techniques

This chapter reviews the details of experiment design and characterization techniques. First, methods selected for preparing samples are presented including pretreatment of starting materials and settings of heat treatment in Section 3.1. Section 3.2 and Section 3.3 introduce the choice of characterization tools used for the two types of interfaces, that is, the interface between gold particles and rutile support, and the interface between gold seeds and TiO_x adsorbates. For the latter one, special experiment set-up was applied to better reveal structural features at the interfaces. This chapter ends with a brief summary in Section 3.4.

3.1 Sample Preparation

3.1.1 Sample Preparation Procedures

In order to facilitate structural characterization of interfaces, thermal dewetting of gold solid films on single-crystal rutile substrates was selected in our work. Briefly, thin films of gold were deposited on single-crystal substrates and heated to high temperature at which the films broke up and formed isolated islands driven by the minimization of total surface and interface energy. Thermal dewetting has following advantages over direct deposition of nanoparticle suspensions to oxide substrates and deposition-precipitation of Au from Au-containing solutions. First, only oxide support and sputtering target are involved in the deposition of gold thin films, which reduces the effect of additives and impurities on interface. Secondly, it allows the production of large-scale samples with a process that is simple and easy to control. Heating temperature was set in the range of 600-1000 ℃ (below the melting point of Au, 1064 ℃) to investigate the effect of heat treatment temperature on gold-rutile interface. Table 3.1 lists the variation of both temperature and time in heat treatment.

For sample preparation, single crystal, 10×10×1 mm, one side EPI polished TiO_2 (rutile, space group $P4_2/mnm$, a = 4.5936 Å, c = 2.9582 Å) substrates were purchased from MTI Corp with (110) termination and surface finish less than 5 Å. The crystal was then cut into 4 pieces (5×5×1 mm) with a diamond knife for further experiment. In detail, rutile substrate was fixed on a slide using hot glue with the unpolished side facing the slide. Next, place the wheel on one edge of the crystal and run the cutter along surface with pressure until a complete and smooth score appear. Finally hold the rutile substrate and break it into two halves along the score. Four pieces of smaller crystals could be obtained by repeating the above steps. It is worth noting that gloves should be worn when dealing with the crystals to avoid contamination especially on the polished side of rutile since gold-rutile interface is sensitive to surface conditions.

Table 3.1 Heat treatment conditions of samples

No.#	Temperature / ℃	Time / minutes
1	600	10
2	700	10
3	800	10
4	1000	10
5	1000	60

Figure 3.1 shows the major procedures of sample preparation. The rutile substrates after cutting were ultrasonically cleaned with acetone. Each crystal was placed in a 10 mL disposable test tube which was filled with 99.99% pure acetone purchased from Shanghai LingFeng Chemical Agent Ltd. After ultrasonication for 30 minutes, the acetone and tube was refreshed for a second run of cleaning. The cleaning step was finished after repeating for 6 times and the substrate was taken out for natural drying. Gold film with a thickness of 10 nm was then sputtered on rutile substrate (Hitachi E-1045 Ion Sputter Unit) and the sample was transferred to a furnace (GSL-1400X tube furnace from MTI Corp) for heat treatment at 600-1000 ℃ as listed in Table 3.1. In order to create an inert atmosphere and suppress the vaporization of gold at high temperatures, argon of 99.9% purity was flowing in the furnace throughout the heating process. For nanowire growth, the sample was sealed in a quartz tube (diameter of 1 cm, thickness of 1 mm, and length of 10 cm) that was filled with 100 mmHg argon (No.5 sample). The length of the vessel was chosen to fit the isothermal region of the furnace. The rate of temperature increase was 10 ℃/min and the rate of natural cooling in the furnace was 2 ℃/min. For more details of tube sealing and heat treatment, see Appendix A.

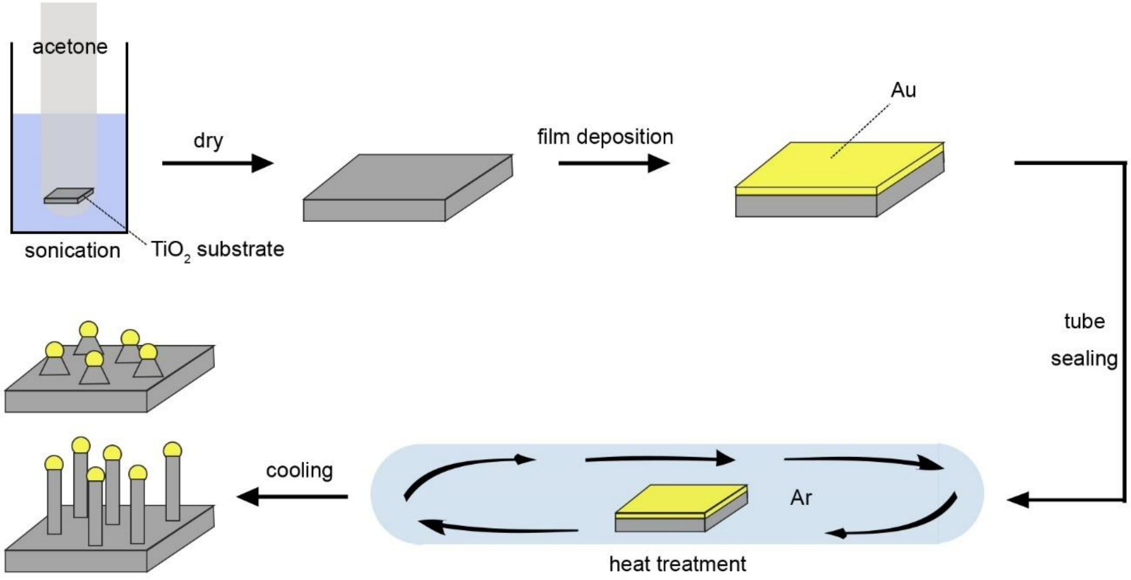

Figure 3.1 Scheme of sample preparation procedures.

3.1.2 Morphology of Prepared Samples

Using the methods introduced above, gold-rutile samples were produced with a visible darkened color in comparison to the transparent rutile crystal before experiment. The morphology of as-prepared samples was examined with SEM. Figure 3.2 shows the morphology of as-prepared samples after heat treatment at various conditions. After being heat treated at 600 °C for 10 minutes, gold films were dewetted to nanoparticles that were randomly distributed on the substrates. Besides, faceted and elongated shapes could be observed especially for large particles. When the temperature was increased to 700 °C, the average aspect ratio of the particles was close to unity. Further rise in temperature induced truncated quadrangular pyramids beneath the particles with elongation along $[001]_{TiO2}$ direction. This feature is similar to the oxide bases in other metal-oxide systems such as Au-$MgAl_2O_4$ [38] and Au-$SrTiO_3$ [43] in which the shape is dependent on the symmetry of substrate surface. At 1000 °C, ridges (see yellow arrow in Figure 3.2(d)) appeared under the particles with a contrast close to the rutile substrate. After heating time was extended, the grown nanostructures evolved in both size and morphology as presented in Figure 3.2(e). After heat treatment at 1000 °C for 60 minutes, vertical nanowires with lengths of 20-30 microns were observed on the substrate. At higher magnification as inserted, these wires were composed of three parts including (i) pyramid-like bases, (ii) bead-like nanowires with a uniform diameter, and (iii) a nanoparticle on the top, which is a common feature of nanowires obtained through VLS and VSS growth

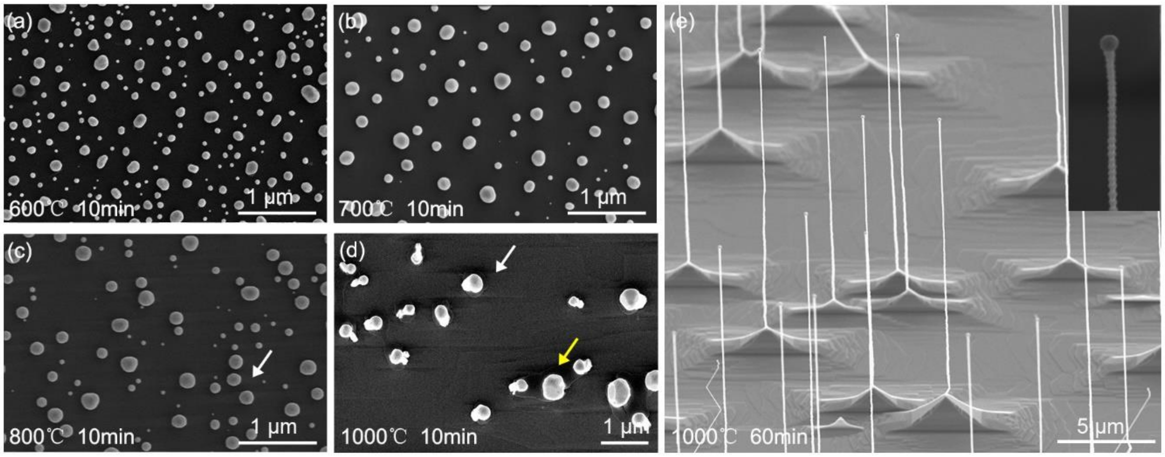

Figure 3.2 Morphology of sample surface after various heat treatment. (a)-(d) SEM images of sample surface after heat treatment at conditions of 600 ℃ and 10 minutes for (a), 700 ℃ and 10 minutes for (b), 800 ℃ and 10 minutes for (c), 1000 ℃ and 10 minutes for (d), 1000 ℃ and 60 minutes for (e), respectively. Insert in (e): enlarged image of a typical nanowire. The tilt angle of SEM sample stage in (e) is 30°.

There are three interfaces involved in the present systems: (i) the interface between dewetted gold particles and single-crystal rutile substrates, (ii) the interface between gold seeds and rutile nanowires; and (iii) the interface between TiO_x adsorbates and gold seeds (in this case, adsorbates appear as a few nm thick layer on gold seeds as discussed in Chapter 6 [13]). The first two interfaces have unique crystallographic features since gold lattice directly contacts rutile lattice, while the last interface has complex local environment of atoms because TiO_x adsorbates are randomly located on gold seeds.

For SEM imaging, the SEM models used in this work included Tescan Mira3, FEI Nova NanoSEM 450, and Zeiss Ultra Plus Field Emission SEM with a resolution limit of ~1 nm. All samples were readily mounted to stubs through conductive carbon adhesive tapes. Low accelerating voltage (5 keV) was chosen because: (i) rutile has poor conductivity, thus charging occurs leading to drift of image during beam scan. This effect can be mitigated by lowering the voltage which increases the emission coefficient of SE, and (ii) low-energy electrons have less damage on sample surface. In addition, a 20 nm layer of carbon was also deposited by sputtering prior to SEM observations to improve the conductivity of substrates except the nanowire sample. High resolution SE detectors including Everhart-Thornley detector (ETD) and through-lens detector (TLD) were used to collect electrons. ETD was used to review samples at lower magnifications in field-free mode, while TLD worked in immersion mode to acquire ultra-high resolution micrographs at higher magnification. It should be noted that for TLD to be available, working distance is required to be less than 7 mm. Therefore, attention should be paid to working distance and the type of detectors when tilt is applied to the stage.

3.2 Interface between Gold Nanoparticles and Rutile Substrates

3.2.1 Preparation of TEM Samples

For gold nanoparticles supported on rutile substrates, focused ion beam (FIB, FEI Versa 3D and GAIA3 GMU Model 2016) technique was used to prepare cross-section specimens for transmission electron microscopy (TEM) characterization of gold-rutile interface. When a focused ion beam impinges on the specimens, beam-induced damage is inevitable due to momentum transfer and ion implantation, resulting in a damaged surface layer with amorphization and defects. Therefore, protective Pt layer, which also served as a marker, was deposited on target region prior to cutting. In order to reduce damages on Au nanoparticles, a thin Pt layer with a thickness of tens of nanometers was first deposited by electron-beam induced deposition. Subsequently a Pt bar of ~1 μm in thickness was deposited with ion beam. Next, H-bar method was used to prepare TEM specimens in which a lamella can be acquired after cutting two trenches with Ga+ ion beam. The specimens were further thinned to ~100 nm and damage-removed with ion-milling (Gatan PIPS II).

Figure 3.3 shows one TEM lamella that is attached to a copper support. Au nanoparticles are well defined between Pt layer and rutile substrate as indicated by the black circles. Although the position of cutting was randomly determined on surface, the density of nanoparticles was sufficiently high to ensure the existence of Au nanoparticles in each specimen. To better investigate the epitaxial relationship between gold and rutile, specimens were cut along two directions including $[001]_{TiO2}$ and $[1\bar{1}0]_{TiO2}$.

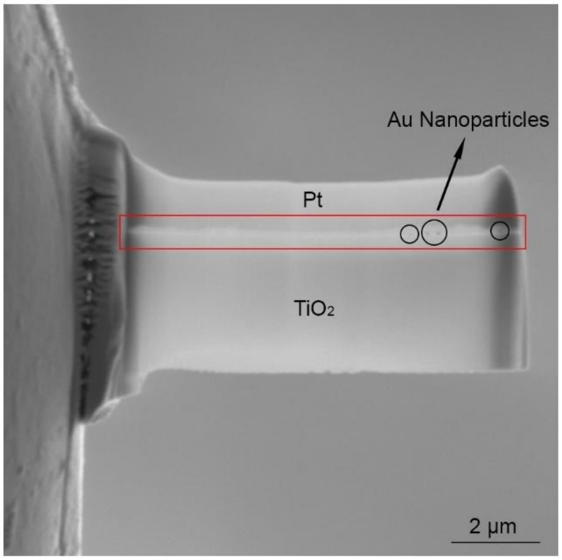

Figure 3.3 A typical TEM specimen prepared with FIB. The boundary between Pt and rutile is located within the red rectangle. Au nanoparticles are shown by the black circles.

For TEM characterization of the nanowires, nanowires on the substrates were transferred to a copper grid that was coated with carbon film. In detail, a grid was scratched across substrate surface at an angle of 30° to the horizontal. Scratch was repeated for 2-3 times along $[001]_{TiO2}$ and $[1\bar{1}0]_{TiO2}$ directions. Although the carbon film might be mechanically damaged at some grids, nanowires lying on good regions could be used for further observations.

3.2.2 Interface Structure Characterization

When high-energy electron beam is incident on specimens typically <100 nm thick, electrons will be elastically or inelastically scattered by atoms carrying the information of the materials. If transmitted electrons are collected by specialized detectors, the morphology, structure, and composition of the specimen can be obtained after appropriate interpretation. With the abundant information and a high resolution, TEM has become an important tool for studying micro- and nano- structures.

In this work, two types of gold-rutile samples were examined with TEM including the FIB specimens shown in Figure 3.3 and the nanowire specimens. To image gold-rutile interface in FIB specimens, the electron beam was converged to a probe and scanned across the specimen. By collecting electrons with large scattering angles, a Z-contrast image was formed reflecting the distribution of averaged atomic number. This high-angle angular dark-field imaging (HAADF) mode would produce a high-resolution image of the interface with well-resolved atom columns.

For the nanowire samples, transmitted electrons were detected to view the overall morphology. The composition of nanowires was analyzed with energy-dispersive X-ray spectroscopy (EDX). Select area electron diffraction (SAED) was used to identify the crystallographic structure of the particles and nanowires. In order to reach certain zone axes especially low-index ones, Kikuchi patterns were taken as the reference during sample tilt, thus a small camera length was used to include more zones and bands in the field of view. As for gold-rutile interface, HRTEM images were acquired at high magnification (×820k).

The instrument and experiment conditions involved in the TEM session are listed as follows: TEM models included JEOL-ARM200F, FEI-Titan 80-300 HB and FEI-Talos F200X operated at 200 kV. For STEM, the convergence angle of the scanning probe and the collection angle of the HAADF detector were 19 mrad and 65-200 mrad respectively in Titan, 30 mrad and 68-280 mrad in ARM. Super-X EDX system with 4 SDD detectors was utilized to perform elemental mapping on the nanowires. For SAED, camera length was 98 mm during holder tilt and 260 mm for imaging of diffraction patterns with a CCD camera. The smallest aperture size (10 µm) was inserted for diffraction due to the small size of gold nanoparticles.

3.2.3 Interface Crystallography

In order to have global information of interface crystallography, XRD was applied to resolve the preferential orientations of dewetted Au nanoparticle on single-crystal rutile substrates. The preferential interfaces were further predicted using geometrical models of gold-rutile interfaces.

3.2.3.1 Experiment

In practice, the orientation of crystal can be represented by stereographic projection. In detail, for a crystal located at the center of a sphere, the normal line of each lattice plane drawn from the center of the sphere intersects with the northern hemisphere at some point P. This point is defined as a pole. By connecting the point with the south pole of the sphere, a point P’ is generated at the intersection with the equatorial plane. This point is unique for each pole, thus it can be used to represent the orientation of corresponding crystal plane. With all the planes projected in this way, we can obtain a stereographic projection of the crystal which consists of all the intersections at equatorial plane. Figure 3.4 (a) presents the stereographic projection for a cubic crystal with a [001] as the normal, i.e., being the north pole of the sphere. When the crystal is rotated to a different orientation, the position of poles will vary accordingly. Therefore stereographic projections can be used to graphically describe the orientation of crystals.

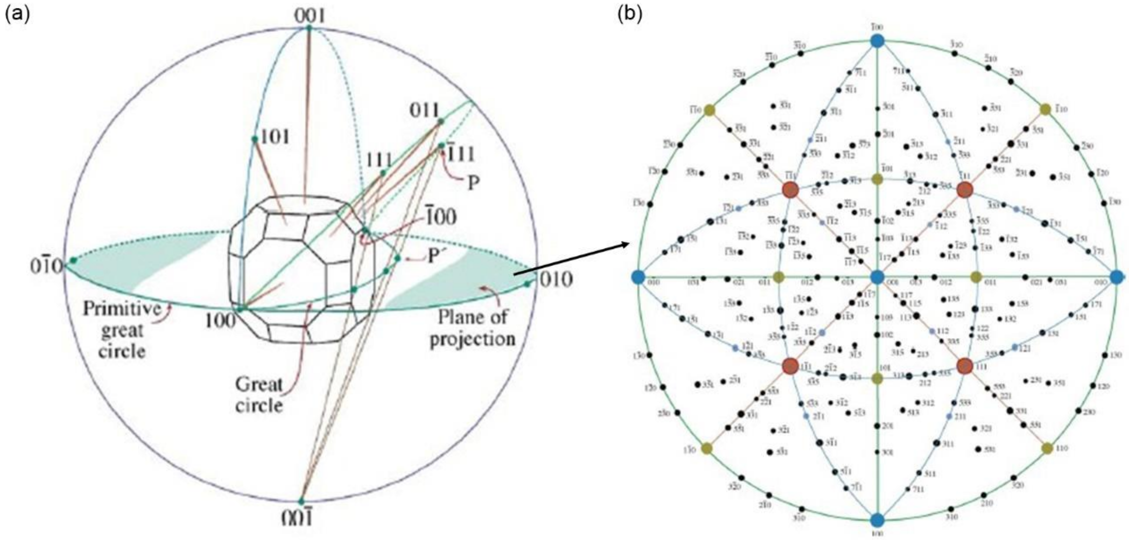

Figure 3.4 Stereographic projections of a cubic crystal. (a) Construction of a stereographic projection. (b) Standard stereographic projection of a cubic crystal [96]. Used with permission.

For a single crystal, the poles of a family of planes, e.g. {111} poles in Figure 3.4(b) denoted by the red points, will show as a set of spots. For polycrystalline samples, variation of orientations leads to a combination of poles from each crystal in the stereographic projection. Therefore, by producing pole figures in which the positions of specific poles such as {111} are recorded, information on crystal orientations can be extracted.

Experimentally, pole figures can be measured with XRD. XRD has broad applications in phase and structure identification particularly for crystals. When incoming X-ray beam interacts with the materials, constructive interference will occur at specific directions for waves elastically scattered by atoms in a set of lattice planes. The condition of this constructive interference, which is also known as X-ray diffraction, is given by Bragg's law:

$$2dsin(\theta) = n\lambda \tag{3.1}$$

where λ is the wavelength of the X-ray source, θ is the angle between incident beam and reflecting planes $(h\ k\ l)$, d is the interplanar distance of the planes, n is an integer number representing the order of reflection. By fixing the position of the X-ray source and rotating the sample in three-dimensional space with a goniometer, diffracted beam of specific lattice planes, e.g. $\{111\}$ can be collected when Bragg's law is satisfied. Integration over the diffraction angles of $\{111\}$ planes can produce a $\{111\}$ pole figure where the orientations of all $\{111\}$ planes in the sample and corresponding weight are represented by the distribution and intensity of $\{111\}$ poles in the figure. With pole figures of two non-parallel planes such as $\{111\}$ and $\{200\}$ pole figures, the orientation of crystals can be fully determined.

In this study, $\{111\}$ and $\{200\}$ pole figures of Au were obtained with Bruker Discover diffractometer to analyze the preferred orientations of dewetted gold nanoparticles on rutile support. Data collection procedures were described by standard Eulerian angles $(\omega, \chi_g, \phi, \psi)$ as shown in Figure 3.4. Two ϕ scans were designed for the same sample with 2θ set to 38° and ω set to 170°. In the first scan, ψ was fixed to 60° or equivalently χ_g was fixed to 30° (90°- ψ). ϕ was scanned from 0° to 360° with an interval of 1°. In the second scan, ψ was fixed at 30° or χ_g was fixed to 60°, and ϕ was scanned from 0° to 360° with an interval of 1°. The exposure time for each frame was set to 10 s.

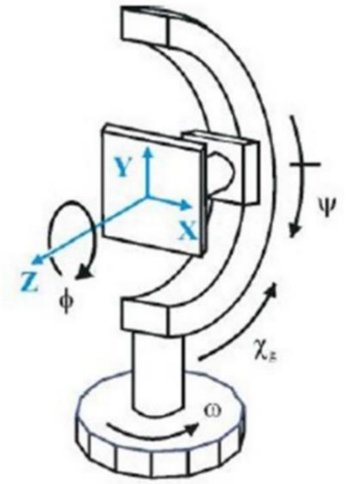

Figure 3.5 Schematic illustration of XRD goniometer showing the rotation axes $(\omega, \chi_g, \phi, \psi)$ and translation axes (X, Y, Z). Image modified from B. B. He [97]. Used with permission.

3.2.3.2 Simulation

Experiment XRD pole figures were interpreted with predicted ORs based on coincidence site lattice (CSL) theory. CSL theory was originally developed to describe grain boundaries by Grimmer et al [98]. For two interpenetrating lattices, if orientation relationship is given, some points from the two lattices may coincide after translation in the space. These coincidence lattice points form a sublattice known as CSL. In CSL theory, lattice strain in the formation of interface is not considered. Generally, for boundary plane that contains dense CSL points, a good fit can be obtained for atoms from the two lattices, thus interface energy is relatively low. In order to form more CSL sites, the two lattices should have special orientation relationships and specific relationship in in-plane lattice symmetry and lattice constants. Therefore, for dissimilar crystals it is hard to form perfect CSL. Instead, a constraint can be applied to either lattice to force the coincidence of points. Accordingly, a better matched sublattice is generated which is defined as constrained coincidence site lattice (CCSL). CSL and CCSL theories provide geometric models of interface that can be used to determine stable interface. Based on these theories, preferred ORs at gold-rutile interface, which should correspond to relatively low energy, can be predicted. Accordingly, interpretation of experiment pole figures can be performed involving following three steps:

(i) Step 1: use the geometric model of gold-rutile interface to predict possible preferential ORs with CSL theory.

(ii) Step 2: simulate pole figures based on predicted ORs and compare the simulations with measured pole figures.

(iii) Step 3: examine the degree of lattice match at gold-rutile interface for each OR in direct space to verify predicted ORs.

3.2.3.3 Estimation of Interface Energy

Experimentally, interfacial energy between a solid substrate and particle can be measured by Winterbottom analysis based on equilibrium shape of the particles [99]. In general, an isolated crystal in equilibrium state is believed to be surrounded by low energy close-packed facets such as (100) and (111) for FCC crystal as a consequence of energy minimization. This faceted morphology is known as Wulff shape. With the assumption of constant volume, the surface energy of each facet is proportional to the distance of the facet to crystal center (Figure 3.6(a)):

$$\frac{\gamma_i}{h_i} = \frac{\gamma_j}{h_j} = const \tag{3.2}$$

If the crystal is attached to a flat and rigid support (Figure 3.6(b)), Wulff construction can be modified to Winterbottom analysis [40,99]. The energy of one free surface is replaced with an effective energy $\gamma^* = \gamma_{interface} - \gamma_s$, where $\gamma_{interface}$ is the interfacial energy and γ_s is the surface energy of substrate in the vapor phase. Then equation (3.2) becomes:

$$\frac{\gamma_i}{h_i} = \frac{\gamma_j}{h_j} = \frac{\gamma^*}{h_i - \Delta h} = const \tag{3.3}$$

Therefore, $\gamma_{interface}$ can be estimated by measuring the ratio of $(h_i - \Delta h)/h_i$. The larger the ratio, the higher the interfacial energy. It is worth noting that Winterbottom analysis is only applicable to large particles (~10-1000 nm in size) so that edge and corner energies can be neglected [99].

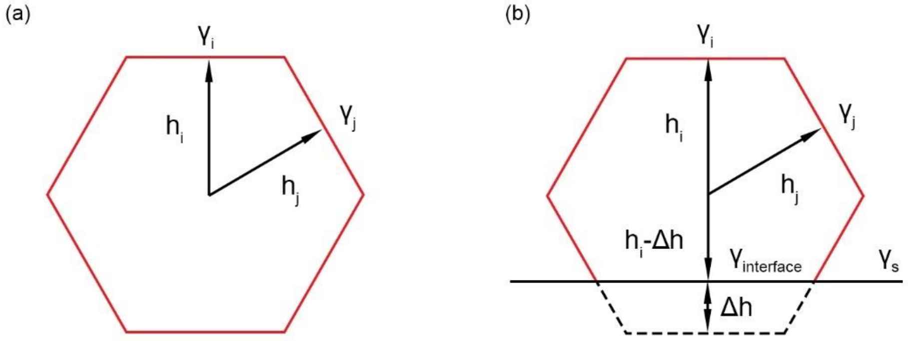

Figure 3.6 Estimation of interface energy. (a) Wulff construction of an isolated crystal in equilibrium. (b) Winterbottom analysis of interfacial energy for a particle on foreign substrate.

3.3 Interface between TiO_x Adsorbates and Gold

X-ray absorption spectroscopy (XAS) was applied to characterize local environment of atoms at TiO_x adsorbates-gold interfaces. In order to magnify weak interface signals, special experimental settings were employed by utilizing the geometry of samples to ensure the beam mainly collects signals from the interface region. Details of data interpretation are listed in the end of this section.

3.3.1 Principles of X-ray Absorption Spectroscopy

When high-energy X-rays are illuminated on materials, core-level electrons can absorb the incident photons and be promoted to unoccupied states. The intensity of absorption events can be described by absorption coefficient and plotted against the energy of X-rays, giving rise to an X-ray absorption spectrum containing the absorption properties of materials of interest. As photon energy increases, absorption coefficient decays steadily except at the binding energy of core orbital which generates a sharp peak termed absorption edge. X-ray absorption fine structures (XAFS) near and beyond the edge are sensitive to the atomic number and electronic states of absorbing sites. According to the energy range, XAS spectrum can be classified into three regions including the absorption edge, X-ray absorption near-edge structure (XANES) and extended x-ray absorption fine structure (EXAFS). XANES is usually defined within 50–100 eV above the edge which can be used as fingerprint to provide information on oxidation state and electronic structure. In contrast, EXAFS refers to the broad region over an energy range of 50-1000 eV above the edge or higher. When photoelectrons are backscattered by neighboring atoms, phase difference between scattering wave and electron wave will in turn modulate X-ray absorption and result in a sinusoidal oscillation in EXFAS region. Thus structural information relevant to neighboring atoms including coordination number, bond length, and disorder can be ascertained especially the first neighbors due to the mean free path of photoelectrons (approximately 5-10 Å) [100]. Combining XANES and EXAFS, XAS measurement would therefore provide us with insight into local structure at gold-rutile interface. To obtain high-quality XAS data with a high signal-to-noise ratio, X-ray beam with high brilliance and small energy bandwidth (<1 eV) over a wide energy is desirable. Therefore, synchrotron radiation source is generally employed to carry out XAS experiment.

3.3.2 Experiment Set-up

The sample to be investigated was rutile nanowires vertically grown on the substrates as shown in Figure 3.2(e). In order to detect the Au-L3 edge near gold-adsorbates interface, i.e. the tip of the nanowires, special configuration and strategy need to be considered for this inhomogeneous sample. The solution we figured out is illustrated in Figure 3.7. A metallic Au foil was set between I_1 and I_2 throughout the entire Au L3 XAFS experiment to provide a reference spectrum. The rutile substrate with grown nanowires was first fixed to the slot of a plastic sample cell with adhesive tape. Next, the cell was loaded to the sample holder with the position and height of the holder roughly adjusted to ensure the sample was on the travel path of incoming X-rays. Ideally, the surface of the sample should be parallel to the beam and only the top of the nanowires rather than the thick rutile substrate is struck by high-energy photons. However, such a perfect alignment of sample is difficult to achieve with naked eyes. Therefore, edges of the substrate were examined alternatively even if the sample may have certain angle with beam direction.

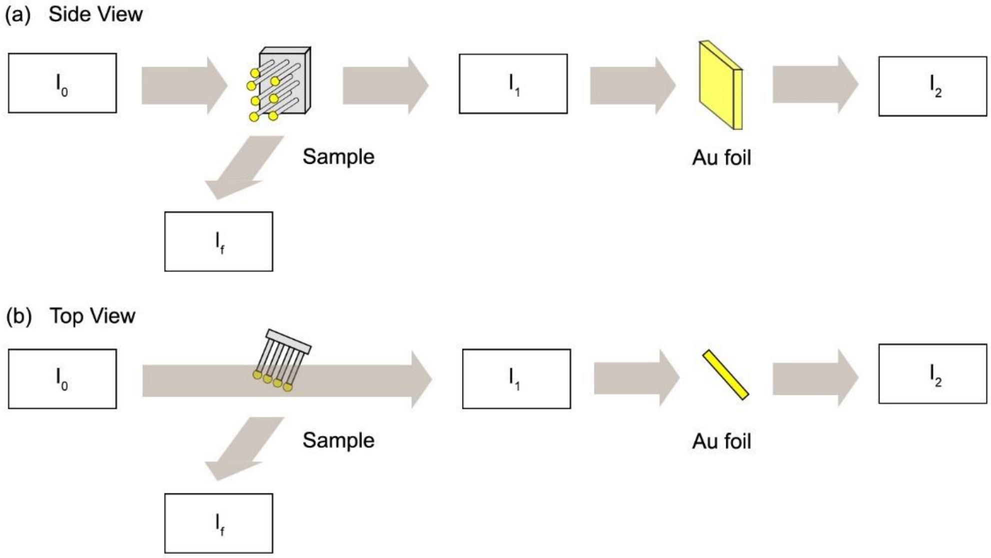

Figure 3.7 Experiment set-up for measurement of Au-L3 edge. (a) Side view. (b) Top view. The gray and yellow colors in the figure represent for rutile and gold, respectively. A standard gold foil is placed after the sample as a reference.

In order to locate the position of edges, following procedures were carried out: Firstly, a sum spectrum was collected covering the energy of Au-L3 edge. If few counts were recorded by the detector, the X-ray spot was likely near the center of the substrate. Then the sample was moved along one direction, either horizontally or vertically, with a large step such as 1 mm until Au peaks appeared in the spectrum, indicating that one edge of the sample was passed through. Next, a 2D map of Au-L3 edge was collected with current position as the map center. The scanning area was determined by setting desirable X-Y range and the number of scanning pixels in X and Y directions. One example is given in Figure 3.8 in which the intensity of Au-L3 edge was progressively measured over 9×13 pixels for an area of 0.3×1.2 mm. Each pixel was represented by a color that showed the number of detected counts. According to the distribution of intensity, it can be seen that the red and orange regions contain much more Au compared with the blue region. The boundary between the two parts indicates an edge or corner of the rutile substrate. By assigning the center of red pixels as the new map center, and the high-intensity area as the new scanning range, a second 2D map was obtained in which the position of desired region was refined. This step was repeated for several times until an area with sufficient Au signals was determined for further data collection.

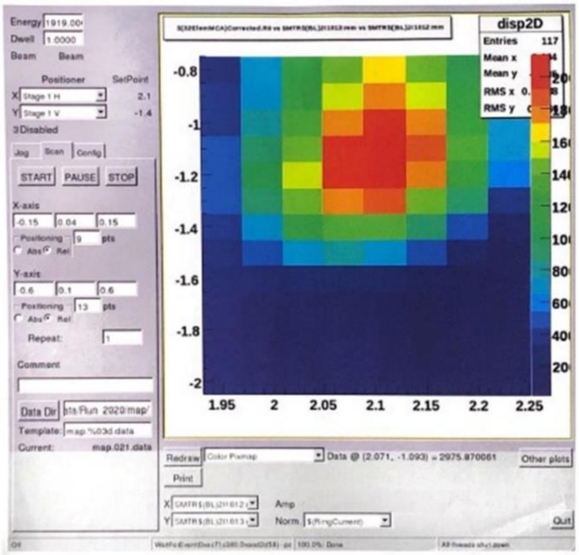
Energy 1919.00
Dwell 1.0000
Positioner SetPoint
X Stage 1 H 2.1
Y Stage 1 V -1.4
X-axis -0.15 0.04 0.15
Positioning 9 pts
Y-axis -0.6 0.1 0.6
Positioning 13 pts
Repeat: 1
Data Dir ts/Run 2020/map/
Template: map %03d.data
Current: map.021.data
Entries 117
Color Pixmap
Data @ (2.071, -1.093) = 2975.870061
X SMTR$(BL)211012
Y SMTR$(BL)211013
Norm $(RingCurrent)

Figure 3.8 An example of 2D map of Au-L3 edge over defined area. The transition of color from blue to red stands for increased counts of signals.

3.3.3 Data Acquisition

In this study, XAS experiment on Au-L3 edge was performed at the HXMA beamline in Canadian Light Source (CLS). For our gold-rutile system consisting of Au, Ti, and O, Au-L3 edge was preferred over Ti-K or Au-L2 edge for following reasons: (i) The energy of Au-L3 edge, 11919 eV, falls in the energy range of the beamline (5-40 keV) compared to the 4966 eV of Ti-K edge [101]. (ii) It is more intense than Au-L2 edge at 13734 eV. The L2 and L3 edge of Au correspond to transitions of electrons from 2p1/2 and 2p3/2 to 5d states, respectively. Given that 2p3/2 has a degeneracy of 4, while 2p1/2 has a degeneracy of 2, L3 edge will have a higher intensity. This is particularly valuable for our samples due to the small amount of Au at the interface. (iii) The influence of TiO_2 nanowires on the resolution of interface species is much greater than Au particles due to the large mass.

In practice, there are two methods available to obtain X-ray absorption spectrum including transmission mode and fluorescence mode which are shown in Figure 3.9. In transmission mode, the flux of beam before and after passing a uniform sample is measured and can be related with:

$$\frac{I}{I_0} = e^{-\mu(E)x} \tag{3.4}$$

$$\mu(E)x = -ln\,(\frac{I}{I_0}) \tag{3.5}$$

where I_0 and I are ionization chamber signals, respectively, $\mu(E)$ is absorption coefficient, x is the thickness of sample. In fluorescence mode, fluorescent X-rays emitted in core hole refilling are detected (I_f) and:

$$\mu(E) \propto \frac{I_f}{I_0} \tag{3.6}$$

Aside from fluorescence photons, it is possible that Auger electrons may also be generated during the decay of excited states. But in hard X-ray regime, X-ray fluorescence dominates over Auger emissions.

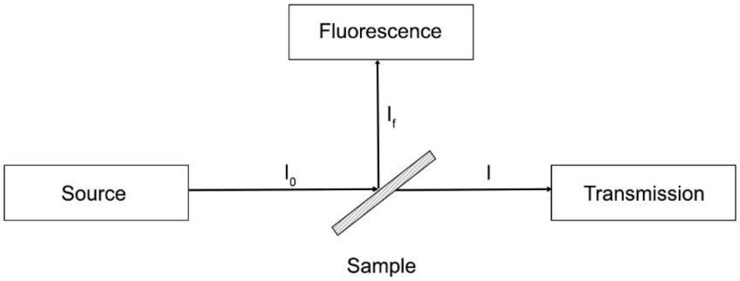

Figure 3.9 Configuration of XAFS measurement with transmission and fluorescence mode.

In this work, fluorescence mode was selected to record the L3 edge of Au, determined by the rutile substrates which have a thickness of 1 mm and low concentrations of interfacial species. CLS storage ring was operated with a current of 220 mA. The primary optics of the HXMA beamline included water-cooled Rh mirror to collimate the beam in focused mode, and a liquid nitrogen cooled double crystal Si(111) monochromator (Kohzu CMJ-1) to provide a monochromatic X-ray beam. Energy resolutions ($\Delta E/E$) was 10^{-4}. For X-ray detection, the chambers were Oxford straight ion chamber filled with 100% He gas. 32 element Ge detector in fluorescence mode was applied to collect signals. The size of beam spot was 0.8 mm×1.5 mm (H×V).

In terms of data collection, a few components of beamline should be adjusted to optimize the XAS spectrum. The monochromatic crystal was detuned to 50% to reduce high harmonic X-ray components in the incident X-ray beam, which may otherwise result in distortions in XAFS spectrum and misleading interpretation [102]. Appropriate gain of I_0, I and I_2 was selected within 2. To improve the signal-to-noise ratio of spectra, multiple scans were performed on the same point and the averaged data was acquired for further analysis. Statistically, the signal-to-noise ratio can be improved by the square root of the number of scans. Herein, 10-15 scans were chosen when collecting data.

3.3.4 Data Analysis of XANES

The XAS data recorded at HXMA was analyzed following the standard procedures of *Athena*. Sample spectrum was generated with the ratio of I_f/I_0. The spectrum measured from standard gold foil, i.e. I_2/I, was used as the reference to calibrate the edge energy of sample spectrum. To directly compare the spectrum with theoretical calculations and other experiment spectra regardless detailed acquiring conditions, the spectrum was normalized by performing low-order polynomial fits to pre-edge and post-edge regions. The pre-edge and normalization ranges should be carefully chosen to avoid interference to the structure information of interest.

Theoretical simulations of Au L3 XANES were performed for a few Au-Ti alloys with *FDMNES* to clarify the features in the spectrum [103]. *FDMNES* calculates the electronic structure of absorbing atoms with DFT. With the crystallographic information of the material, the electronic structure and XANES spectrum could be obtained for a cluster that was constructed with Au as the center. In reality, experiment XAS spectrum generally experiences edge broadening due to instrumental effects such as monochromator, and intrinsic effects of core-hole lifetime width [104]. Therefore, in order to match the degraded resolution, energy resolution of calculated results was reduced by convolving the spectrum with a Lorentzian function. Standard spectrum from the literature was used to optimize the parameters of convolution.

3.3.5 Data Analysis of EXAFS

Data reduction of EXAFS involves dealing with the oscillations of absorption coefficient well above the edge and relating them with the chemistry surrounding central absorber. In detail, absorption coefficient is transformed to a function χ that is defined as:

$$\chi(E) = \frac{\mu(E)_{exp} - \mu(E)_{bkg}}{\Delta\mu(E)_{exp}} \tag{3.7}$$

where $\mu(E)_{exp}$ is experimentally measured absorption coefficient, $\mu(E)_{bkg}$ is the value on the background curve, $\Delta\mu(E)_{exp}$ is the edge step, i.e. the difference between pre-edge and post-edge background. Photon energy is converted to wave number k with:

$$k = \sqrt{\frac{2m(E-E_0)}{h^2}} \tag{3.8}$$

where E is energy of X-ray photons, E_0 is the edge energy, E_0 is the Planck distance. Therefore, the initial $\mu(E)_{exp}{\sim}E$ curve is converted to $\chi(k){\sim}k$. Finally, by applying Fourier transform (FT), $\chi(E){\sim}k$ can be transformed to R space that consists of multiple shells contributed by different scattering paths.

From physical considerations, $\chi(k)$ is related with the interference of backscattering waves and outgoing waves as:

$$\chi(k) = \sum_j S_0^2 N_j \frac{|f_j(k)|}{kR_j^2} \sin\left(2kR_j + 2\delta_c + \phi\right) e^{-2R_j/\lambda(k)} e^{-2\sigma_j^2 k^2} \tag{3.9}$$

In this equation, R_j is interatomic distance, N_j is coordination number, $f_j(k)$ and δ_c are backscattering amplitude and phase shift that reflect the characteristics of scattering atoms. Other terms are used to restrict $\chi(k)$ for precision. $\lambda(k)$ is the mean free path of photoelectrons that limits EXAFS to a local region. σ_j is the Debye-Waller factor for thermal vibrations. S_0^2 is amplitude reduction factor. and σ_j^2 represents mean square relative displacement.

In order to extract R_j, N_j and σ_j^2 from $\chi(k)$, a common strategy is to model each shell of experiment $\chi(k)$ with possible combinations of scattering paths in the sample and to find the best match. The desired values of these variables for each path are then derived from fitting parameters. In this work, EXAFS analysis was performed with *WinXAS* and *Artemis*. After loading the atomic structure of proposed models in *Artemis*, *Feff6* was used to calculate the scattering paths with Au as the absorber. The *Feff* path file was input to *WinXAS* for further refinement of experiment EXAFS. Each shell was defined by a k border and fitted with selected paths. For each path, a few parameters can be adjusted including S_0, R_j, N_j, σ_j^2, and E_0 shift. Thus there will be a number of variables to be determined if all of them are free. However, the number of parameters that we can obtain from data is limited by:

$$N \approx \frac{2\Delta k \Delta R}{\pi} \tag{3.10}$$

here Δk and ΔR are the range of k and R of the data. Thus we need to limit the number of total independent variables from all the paths. In *WinXAS* this could be realized by either fixing the value or correlating the values of different paths. For each variable, a constraint could be additionally applied to confine its value in certain range to avoid irrational results. For example, when first shell of EXAFS was fitted with three paths, S_0^2 was fixed to 0.9. E_0 shift was correlated so that the three paths have identical values and constrained to -6~6 eV. The coordination number was varied from 11.8 to 12.2 for Au-Au and 6-12 for Au-Ti referring to the original values in each scattering path. σ^2 was constrained to 0.005-0.01 for Au-Au and 0.008-0.01 for Au-Ti. Based on all the paths and constraints, *WinXAS* would run the simulation and give the results that are best matched with experiment data. The number of shells considered was increased step by step until all major peaks are fitted with a good quality.

3.4 Summary

Targeting at the gold-rutile interfaces involved in current system, a few techniques were chosen to extract detailed information for different interfaces. For nanoparticles supported on rutile substrates, FIB was used to prepare cross-section specimens for TEM characterization of interface atomistics. The orientation distribution of gold particles was examined with XRD. For rutile nanowires, gold-adsorbates and gold-nanowire interfaces were investigated with XAS and TEM respectively.

Chapter 4 Gold-Rutile Interface in Rutile Supported Gold Nanoparticles

For gold particles supported on rutile substrates, the crystallography and structure of gold-rutile interface were investigated and presented in this chapter. Section 4.1 focuses on the measurement and interpretation of orientation relationship distributions between gold and rutile for a large number of gold nanoparticles. The atomistics of several types of gold-rutile interfaces is demonstrated in Section 4.2. An overall discussion on the evolution of orientation relationships with heat treatment and interface atomistics are included in Section 4.3, and key results are summarized in Section 4.4.

4.1 Interface Orientation Relationships

4.1.1 Measurement of XRD Pole Figures

Figure 4.1 illustrates the pole figures of dewetted gold nanoparticles following heat treatment at 600~1000 ℃. The $\{111\}$ and $\{200\}$ pole figures of Au were obtained by integrating over a 2θ range from 38° to 38.5° and 44.2° to 44.7° respectively. It should be noted that there is overlap of reflections between gold particles and rutile substrates. For instance, the diffraction angles of $(200)_{TiO2}$ (2θ = 38.9°) is close to the measured range of $\{111\}_{Au}$, while $(120)_{TiO2}$ (2θ = 43.7°) is close to $\{200\}_{Au}$. Therefore signals from the rutile substrate may be found in the pole figures. After dewetting at 600 ℃, a bright spot appears in the center of $\{111\}$ pole figure. This indicates that the normal of $\{111\}$ planes in gold particles is parallel to sample normal, i.e. $\{111\}_{Au}$ lattice planes are aligned with sample surface, $(110)_{TiO2}$. However, a diffuse ring is observed for other $\{111\}_{Au}$ planes of the family instead of spots. Thus the in-plane orientation of gold particles is random. This distribution of orientations is referred to as $\{111\}$ out-of-plane texture here. $\{200\}$ pole figure shown in Figure 4.1(b) also confirms this texture. The extra two reflections in $\{111\}$ pole figure and four reflections in $\{200\}$ pole figure labeled by the squares belong to $(100)_{TiO2}$ and $(120)_{TiO2}$ respectively. For the temperature of 800 ℃, preferred in-plane orientation appears as suggested by the transition from ring patterns to strong spots. Combined with the positions of $(100)_{TiO2}$ and $(120)_{TiO2}$ poles which are identical with those in Figure 4.1(a), the in-plane alignment between gold and rutile can be indexed as $\langle 1\bar{1}0\rangle_{Au}//[001]_{TiO2}$. This texture corresponds to the most common orientation relationship in gold-rutile system, ORa, and its 180° rotation variant arising from the two-fold in-plane symmetry of $\{110\}_{TiO_2}$. The star and arc shapes of the poles suggest slight deviation from ideal ORa in some gold particles. In addition to the primary poles of ORa, some weak spots also emerge in the pole figures as shown by the circles in Figure 4.1(c). Although twinning is one of the possible origins, these weak spots cannot be indexed to the $\{111\}$ twins observed in gold particles (twinning is shown later in Section 4.2). In addition, as gold and rutile are non-reactive, the possibility of new interfacial phases could also be ruled out. Therefore, it is likely that other ORs exist in the specimen with a small proportion. As the temperature is raised to 1000 ℃, the intensity of ORa poles is greatly reduced while the number of other ORs is increased, indicating that other ORs can be promoted at high temperature.

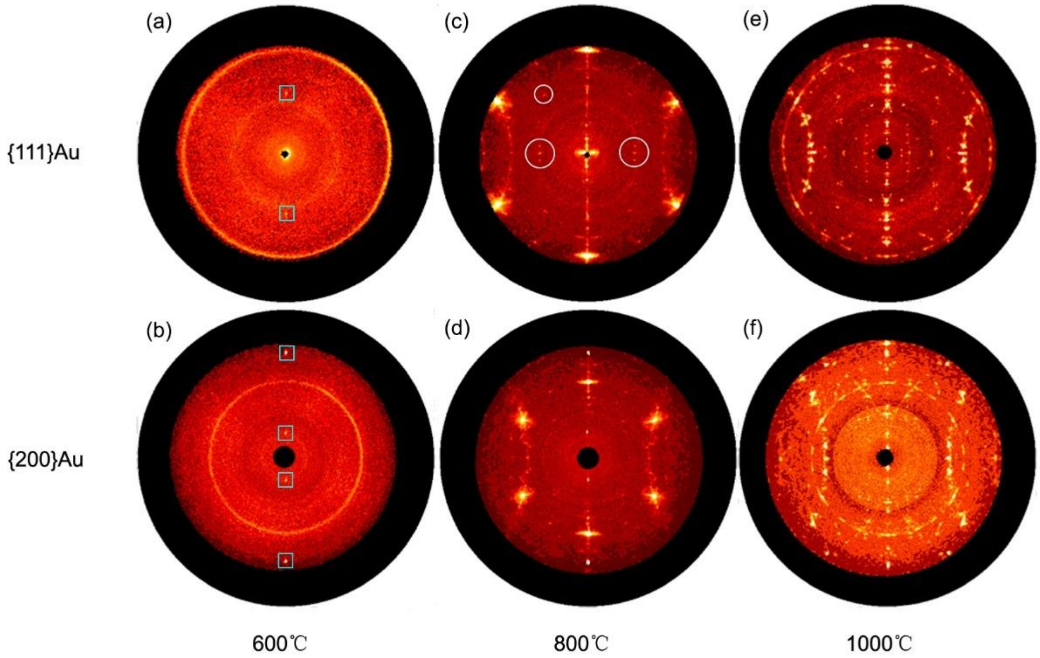

Figure 4.1 Pole figures of rutile supported gold nanoparticles after heat treatment. Heating time for all samples are 10 minutes. (a) and (b) are at 600 ℃, (c) and (d) are at 800 ℃, (e) and (f) are at 1000 ℃. The top row corresponds to Au$\{111\}$ pole figures and the bottom corresponds to $\{200\}$Au pole figures.

4.1.2 Interpretation of Pole Figures

Following the strategy described in Section 3.2, possible ORs in Figure 4.1(e) and (f) were extracted as much as possible. In geometric model, it is assumed that interface with good atomic match is relatively stable. Thus preferential ORs at gold-rutile interface should correspond to a high density of matched atoms. As gold and rutile are incommensurate, two-dimensional atomic match at the interface is complex. Therefore, the problem was simplified to two steps. First, the good-matched direction pair between gold and rutile were determined by calculating lattice misfits of various pairs. The misfit δ between two directions is defined as:

$$\delta = \frac{|d_{TiO2} - d_{Au}|}{1/2(d_{Au} + d_{TiO2})} \tag{4.1}$$

in which d_{TiO2} and d_{Au} are atomic distances along corresponding directions in gold and rutile, respectively. Accordingly, misfits of a few direction pairs were calculated for direction pairs that meet following conditions: (i) have low index (index < 3), (ii) have distance less than 0.7 nm; and (iii) the direction of rutile in the pair lies in $(110)_{TiO2}$ plane. The distance between neighboring atoms in both directions and corresponding misfit for each pair is presented in Figure 4.2. Although the lattice misfit of $[111]_{Au}//[1\bar{1}1]_{TiO2}$ is slightly smaller than $[110]_{Au}//[002]_{TiO2}$, the density of atoms is higher in the latter pair. Considering that $\langle 1\bar{1}0\rangle_{Au}//[002]_{TiO2}$ is contained in all previously reported ORa-ORd, we choose this pair as the best-matched directions.

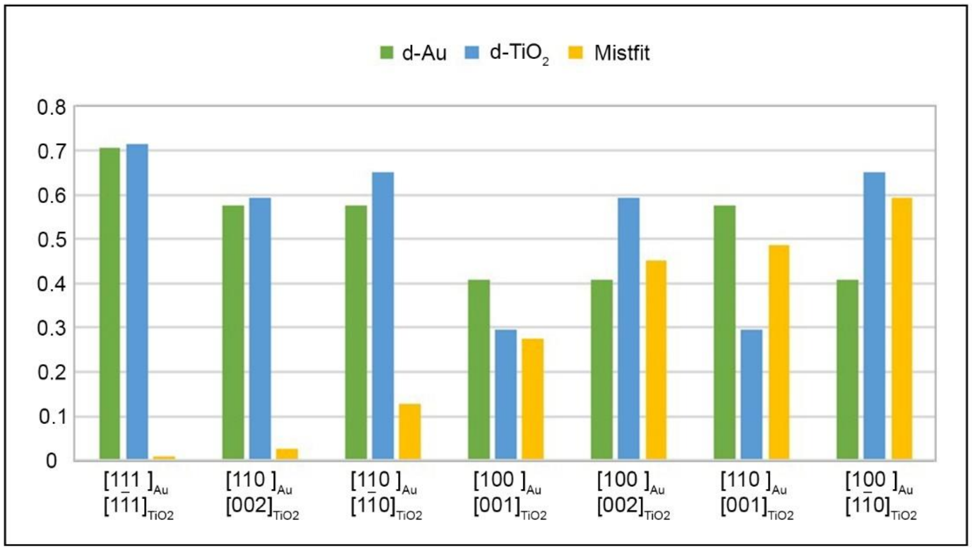

Figure 4.2 Atomic match of gold and rutile lattice in specific low-index direction pairs. The neighboring distance of atoms along each direction in gold, rutile, and corresponding lattice mismatch are shown with green, blue, and orange bars respectively.

Next, assuming all preferential ORs at gold-rutile interface contains this best-matched direction pair, then preferential ORs can be predicted by finding lattice plane pairs at the interface that have approximate interplanar spacing. This procedure can be facilitated by analyzing in reciprocal space as illustrated in Figure 4.3. At $\langle 1\bar{1}0\rangle_{Au}//[002]_{TiO2}$ zone axis, the diffraction patterns of gold and rutile were overlapped with $(002)_{Au}//(1\bar{1}0)_{TiO2}$, i.e. ORc. By rotating the pattern of gold with respect to rutile, some reflections of gold got close to those of rutile. Then the closest pair from gold and rutile would correspond to lattice planes with most similar interplanar spacing. In this way, a few ORs were determined corresponding to various rotation angles of gold pattern. In addition to the previously observed ORa, ORb, ORc, ORd, following irrational ORs could also be obtained and named as ORe, ORf, and ORg, respectively. 1 and 2 represent identical plane matching pair between gold and rutile. For example, $(220)_{Au}$ was matched with $(\bar{1}30)_{TiO2}$ for ORf1 and $(310)_{TiO2}$ for ORf2. Thus we classified them as similar type of OR here. A rotation of 90° exists between ORf1 and ORf2 as shown by the blue arcs in Figure 4.3. This similar plane match pair does not mean the two ORs have identical interface because $\langle 1\bar{1}0\rangle$ is not four-fold axis in gold. The indices of ORe-ORf are described as follows which can be directly compared with ORa-ORd:

ORe1: $\left\{1\ 1\ \ 4-3\sqrt{2}\right\}_{Au}//\{110\}_{TiO_2}, \langle 1\bar{1}0\rangle_{Au}//[001]_{TiO_2}$

ORe2: $\left\{1\ 1\ \ 4+3\sqrt{2}\right\}_{Au}//\{110\}_{TiO_2}, \langle 1\bar{1}0\rangle_{Au}//[001]_{TiO_2}$

ORf1: $\left\{1\ 1\ \ \sqrt{2}/2\right\}_{Au}//\{110\}_{TiO_2}, \langle 1\ \bar{1}\ 0\rangle_{Au}//[001]_{TiO_2}$

ORf2: $\left\{1\ 1\ \ 2\sqrt{2}\right\}_{Au}//\{110\}_{TiO_2}, \langle 1\bar{1}0\rangle_{Au}//[001]_{TiO_2}$

ORg1: $\left\{1\ 1\ \ \sqrt{2}/3\right\}_{Au}//\{110\}_{TiO_2}, \langle 1\bar{1}0\rangle_{Au}//[001]_{TiO_2}$

ORg2: $\left\{1\ 1\ \ 3\sqrt{2}\right\}_{Au}//\{110\}_{TiO_2}, \langle 1\bar{1}0\rangle_{Au}//[001]_{TiO_2}$

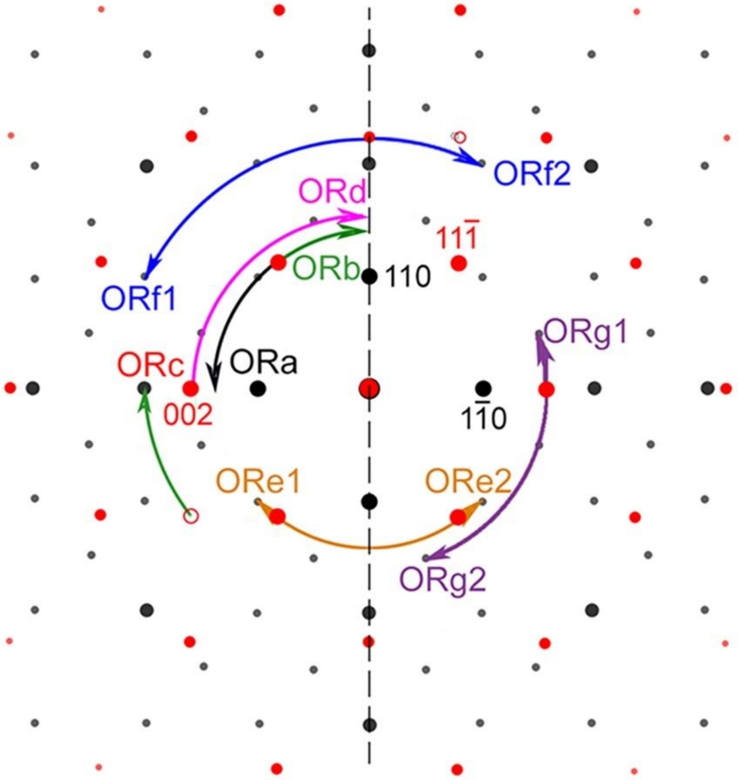

Figure 4.3 Superimposed diffraction patterns of gold (red spots) and rutile (black spots) along $\langle 1\bar{1}0\rangle_{Au}//[002]_{TiO2}$ zone axis showing the operation to predict preferential ORs. The forbidden reflections of gold are represented by the hollow circles. The rotation operation for each OR is denoted by arcs.

According to the ORa-ORg predicted above, pole figures were simulated without taking into account the weight of each OR. As presented in Figure 4.4, the experiment pole figures of gold particles dewetted at 1000 ℃ agree well with the simulation results at most of the poles. Higher order of twinning was not included in the calculation because its intensity is much lower than the first order twins. While it is hard to carry out quantitative analysis on the weight of ORs due to severe overlap of spots and difficulty to distinguish low intensity signals, the uniform intensity distribution indicates a roughly equal probability of all ORs. Besides, the newly discovered irrational ORs can also explain some weak spots appearing at 800 ℃ as labeled in Figure 4.1. Therefore, this interpretation of pole figures should be reasonable considering the consistency between experiment and calculation results.

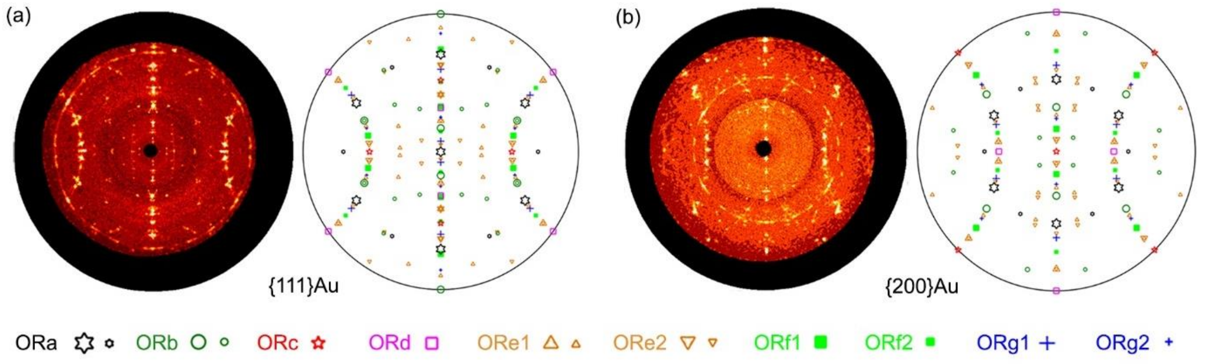

Figure 4.4 Comparison between experiment and calculated pole figures with predicted ORa-ORg. (a) {111}Au pole figures. (b) {200}Au pole figures. The smaller symbols of ORa denote its variations with 30° rotation. The smaller symbols of ORb and ORe1-2 are for their first-order twinned orientations.

4.2 Atomistics of Gold-Rutile Interface

To reveal the arrangement of atoms at gold-rutile interface, thin lamellas prepared using FIB were examined in TEM. Following observations were performed in samples that were heated at 800 °C because: (i) the growth of oxide bases is not evident when heating temperature is below 800 °C as shown in Figure 3.2; (ii) samples of 800 °C contain other irrational ORs in addition to ORa as indicated by weak poles in the pole figures; (iii) the shape of particles is not regular for samples being heated at 1000 °C possibly due to the temperature near melting point of gold (1064 °C). This is not advantageous to the estimation of interface energy based on Winterbottom analysis.

Figure 4.5 presents the morphology of dewetted nanoparticles in a representative TEM specimen. The contrast of the four layers in Figure 4.5(a) can be identified to be single-crystal TiO_2 substrate, carbon coating for SEM characterization, Pt layer deposited by electron beam and ion beam respectively from bottom to top. Bases of 10-20 nm in height are detected under the particles with the same contrast as the substrate, suggesting a composition close to TiO_2. Similar bases have been reported in other gold-oxide systems [105,106]. It is of great interest that holes can be observed at the interface in some particles as shown by the red circles. This will be discussed later in this chapter.

All nanoparticles were further examined with STEM-HAADF imaging. As a result, five types of gold-rutile interfaces were recorded with their orientation relationships indexed as ORa, ORb, ORc, ORe1, and ORf1. The structure of each interface is described in this section.

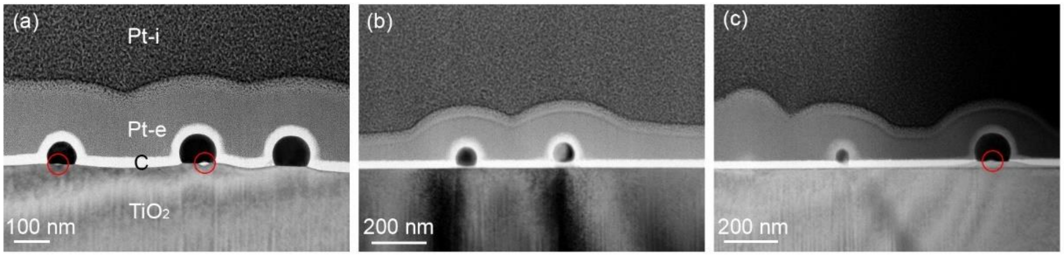

Figure 4.5 TEM micrographs of nanoparticles in a typical FIB specimen.

4.2.1 ORa interface

Figure 4.6 shows the interfaces of two gold nanoparticles projected along two perpendicular directions, both of which have an orientation relationship of ORa as confirmed by the good agreement between STEM-HAADF images and inserted atomic models, as well as the fast Fourier transform (FFT) images. This $(111)_{Au}//(110)_{TiO2}$ OR is the most commonly observed one in gold-rutile system. Although the mismatch between FCC Au and tetragonal TiO_2 is generally large, there are certain directions in which good alignment of atoms can be achieved.

Viewed along $[11\bar{2}]_{Au}//[1\bar{1}0]_{TiO2}$ direction (Figure 4.6(a)), $[1\bar{1}0]_{Au}$ is epitaxial with $[001]_{TiO2}$. This is consistent with the small lattice misfit along $[1\bar{1}0]_{Au}//[001]_{TiO2}$ (2.57%) in Figure 4.2. To accommodate this small mismatch misfit dislocations are formed to partially release strain at the interface. The positions of these dislocations are recorded and labeled in the inverse FFT image where extra half-plane of atoms is present in gold lattice. The average spacing of these mismatch dislocations is roughly 4-6 nm, agreeing with the predicted value of 3.9 nm.

Viewed along $[1\bar{1}0]_{Au}$ $//[001]_{TiO2}$ direction, individual atoms can be better distinguished from the HAADF image, especially the gold atoms located in topmost Ti-O layer. The interplanar spacing between interfacial Au and Ti-O planes can be measured as 0.24-0.26 nm. This value was previously reported in relaxed $(111)_{Au}//TiO$ reconstructed TiO_2 (110) interface (0.245 nm) calculated by DFT in which Au atoms were mixing with the topmost Ti-O layer (see Figure 2.7(d)) [76]. Besides, twining is regularly observed in these ORa gold nanoparticles with $(111)_{Au}$ being the twin boundary. One example is given in Figure 4.6(c).

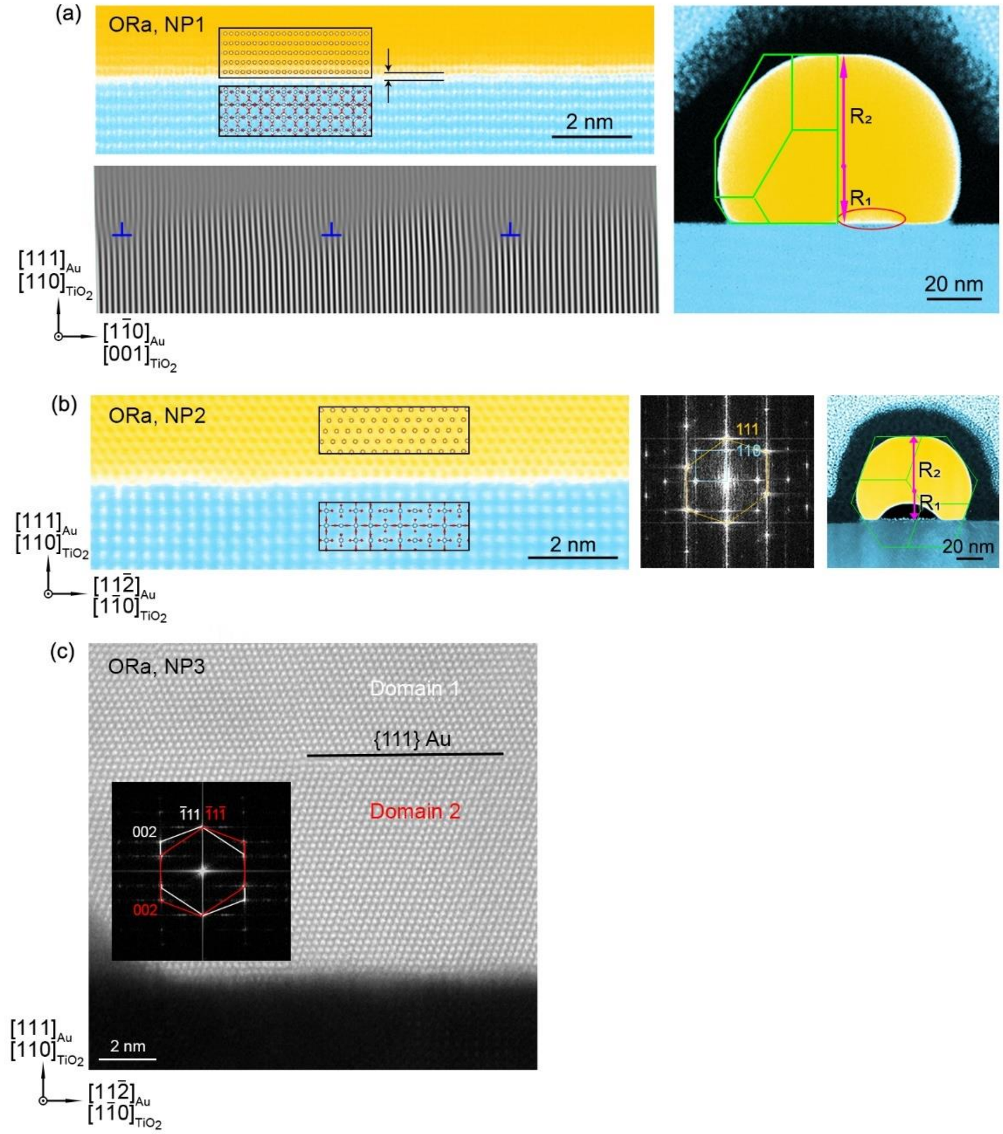

Figure 4.6 Gold-rutile interface of two ORa nanoparticles. (a) Nanoparticle 1 (NP1) viewed along $[11\bar{2}]_{Au}$ // $[1\bar{1}0]_{TiO2}$ direction. (b) Nanoparticle 2 (NP2) viewed along $[1\bar{1}0]_{Au}$ // $[001]_{TiO2}$ direction. The STEM-HAADF images are color-coded to enhance the contrast with the atomic models of gold and rutile inserted (generated with Vesta [107]). The intensity of blue, white and golden are in ascending order. The inverse FFT image in (a) shows the locations of misfit dislocations at the interface. The FFT image of NP1 is given in (b) to confirm interface OR in which blue and golden colors stand for rutile and gold respectively. Modified Wulff constructions of both nanoparticles are demonstrated on the right for the measurement of interfacial energy. (c)

Nanoparticle 3 (NP3) which contains $\{111\}$ twinning in Au. The inserted FFT image shows two sets of reflections corresponding to the two twinned domains.

In terms of interfacial energy, estimations were made by Winterbottom analysis based on the shape of gold nanoparticles as stated in Section 3.2. Facet that does not intersect with the substrate can be used to measure R_2. As a result, the ratio of R_1/R_2 is approximately 0.5 for ORa from Figure 4.6. Although gold particles may not have perfect Wulff shape with roughness at the top or edge surfaces due to surface fluctuations at finite temperatures, this R_1/R_2 value may provide a reference for comparison of interfacial energy between various ORs. More interestingly, interface voids are found in the ORa particles examined as shown by the weak contrast and red ellipse in Figure 4.6(a). It is not likely that damage from sample preparation should be responsible for these voids, since they can be observed within ~50% particles of the FIB specimens. Hence the formation of interface voids may be governed by other factors such as the nature of gold-rutile interface.

4.2.2 ORb Interface

Compared with the regular interface of ORa, the ORb interface in our system is much rougher as shown in Figure 4.7. The Au atoms adjacent to the interface form alternating steps of $\{111\}_{Au}$ and $\{100\}_{Au}$which are low energy planes of gold, but no periodicity is observed in these steps. More importantly, a transition layer appears between gold and rutile lattices with a thickness less than 2 nm. The arrangement of atoms within this region does not match the lattice of either Au or TiO_2 including rutile, anatase, and brookite viewed from any directions. Instead, a new pattern is observed which is close to the superimposition of the two lattices with relaxation possibly to release misfit strain. Since TEM images are 2D projections of specimen, there remains uncertainty on whether the pattern results from penetrating gold and rutile lattices or the roughness of the interface. Although the ratio of R_1/R_2 is ~0.84 from Figure 4.7(c), this ORb particle deviates from perfect Wulff shape, thus the estimation of R_1/R_2 may not be accurate. Nevertheless, ORb interface has a higher energy than ORa. It should be noted that only one ORb particle was detected in our experiment. Therefore, it is rash to conclude that the appearance of such rough interface is determined by interface OR.

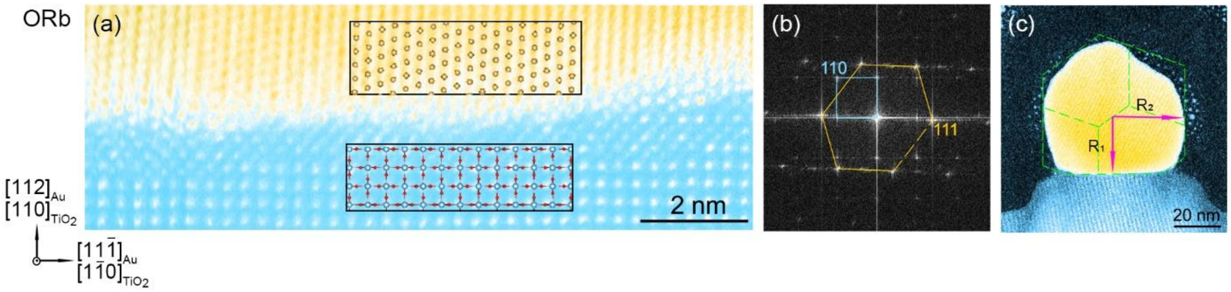

Figure 4.7 ORb interface viewed along $[1\bar{1}0]_{Au}//[001]_{TiO2}$ direction. (a) STEM-HAADF image of gold-rutile interface with the atomic models of gold and rutile inserted. (b) The FFT image of (a). (c) The morphology of the ORb particle and its modified Wulff construction. The images are color-coded to enhance the contrast. Blue, white, and golden colors represent the intensity of HAADF signal in an increasing order.

4.2.3 ORc Interface

Figure 4.8 presents one ORc nanoparticle and corresponding gold-rutile interface. Likewise, the gold particle also contains {111} twinning as ORa particles, thus the construction of Wulff shape was modified with respect to the twinning plane. The influence of twin energy was not considered because of the low energy of coherent twin boundaries in gold [108]. As the twinning plane does not intersect with the interface, R_1 and R_2 measured from the bottom domain can still be used to estimate interface energy. The high contrast of golden cluster in this particle is likely to result from ion beam in FIB sample preparation, but it should have negligible influence on most area of the interface. Consequently, the ratio of R_1/R_2 for this ORc particle is approximately 0.65, which is slightly higher than that of ORa, indicating a less stable interface. The spacing between interfacial Ti-O and Au layers at the interface is ~0.3 nm according to the STEM-HAADF micrograph. Although edge dislocations are also recorded in the inverse FFT image, no specific spacing between neighboring dislocations is observed which is different from that of ORa. For example, in Figure 4.8(b), the two dislocations have a spacing of ~3 nm with most regions free of dislocations. This variation of dislocation distribution between ORa and ORc along identical direction, i.e. $[1\bar{1}0]_{Au}$ // $[001]_{TiO2}$, may originate from different lattice mismatch in the perpendicular direction, since the relaxation of misfit strain at gold-rutile interface involves two dimensions in the plane.

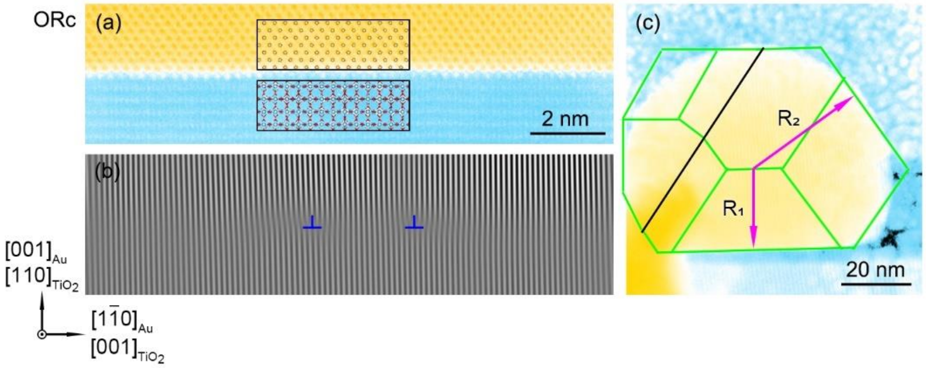

Figure 4.8 ORc interface viewed along $[110]_{Au}//[1\bar{1}0]_{TiO2}$ direction. (a) STEM-HAADF image of gold-rutile interface with the atomic models of gold and rutile inserted. (b) The inverse FFT image of (a) showing the locations of misfit dislocations at the interface. (c) The overall morphology of the particle and its modified Wulff construction. The black line indicates the position of $\{111\}$ twinning plane. The images are color-coded to enhance the contrast. Blue, white, and golden colors represent the intensity of HAADF signal in an increasing order.

4.2.4 ORe1 Interface

Apart from the reported ORa and ORc, a few new orientation relationships were also discovered in TEM observations. One of them was named as ORe1 and shown in Figure 4.9. As shown in the atom-resolved micrograph in Figure 4.9(a), the gold layers at the interface have a zig-zag shape, showing an alternation of low index atomic planes, $(001)_{Au}$ and $(110)_{Au}$. According to the FFT image in Figure 4.9(b), $\{11\bar{1}\}_{Au}$ reflection is overlapped with $\{200\}_{TiO_2}$, thus the OR can be determined as:

$$\{1\ 1\ \ 0.242\}_{Au}//\{110\}_{TiO_2}, \langle 1\bar{1}0\rangle_{Au}//[001]_{TiO_2}$$

This corresponds to the ORe1 predicted in Section 4.1.2:

ORe1: $\left\{1\ 1\ \ 4-3\sqrt{2}\right\}_{Au}//\{1\ 1\ 0\}_{TiO_2}, \langle 1\ \bar{1}\ 0\rangle_{Au}//[0\ 0\ 1]_{TiO_2}$

Since the twin plane in the gold particle does not intersect with the interface, it is reasonable to evaluate interfacial energy via Winterbottom analysis. The ratio of R_1/R_2 is measured with a value of ~0.8. Moreover, strong intensity is detected at the interface as shown by the white contrast in Figure 4.9(c), similar to the interfacial voids observed in previous ORa particles.

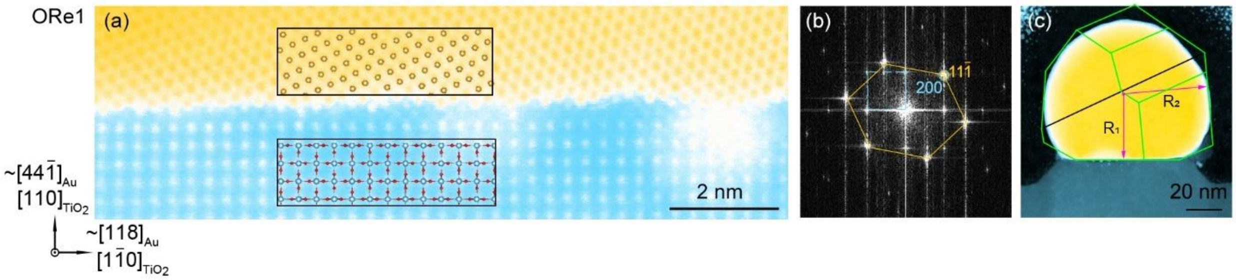

Figure 4.9 ORe1 interface viewed along $[1\bar{1}0]_{Au}$//$[001]_{TiO2}$ direction. (a) STEM-HAADF image of gold-rutile interface with the atomic models of gold and rutile inserted. (b) The FFT image of (a). (c) The morphology of the ORe1 particle and its modified Wulff construction. The black line indicates the position of $\{111\}$ twinning plane. The images are color-coded to enhance the contrast. Blue, white, and golden colors represent the intensity of HAADF signal in an increasing order.

4.2.5 ORf1 Interface

Figure 4.10 presents another new irrational OR observed in gold nanoparticles. This interface shares similar features with ORe1 regarding the zig-zag shape of gold rows. The major difference lies in the smaller tilt angle of $\{111\}_{Au}$ depending on the orientation relationship at the interface. For this interface, $\{111\}_{Au}$ planes are 12 degrees with $\{110\}_{TiO_2}$. A similar angle was reported in Akita's work where $\{111\}_{Au}$ of ~3 nm gold particles was tilted 15 degrees off $\{110\}_{TiO_2}$ viewed along $\langle 1\ \bar{1}\ 0\rangle_{Au}//[0\ 0\ 1]_{TiO_2}$ [79]. Although the exact OR was not given in his case, our interface might be the same type. In the FFT image, the spot of $(130)_{Au}$ coincides with $(220)_{TiO2}$. Both the matching pair of reflections and the atomic models in Figure 4.10(a) confirm the index as:

$\{1\ 1\ 0.706\}_{Au}//\{110\}_{TiO_2}, \langle 1\bar{1}0\rangle_{Au}//[001]_{TiO_2}$

This can be classified to ORf1:

ORf1: $\left\{1\ 1\ \ \sqrt{2}/2\right\}_{Au}//\{110\}_{TiO_2}, \langle 1\bar{1}0\rangle_{Au}//[001]_{TiO_2}$

Correspondingly, the R_1/R_2 ratio of ORf1 is 0.7 from Figure 4.10(c), lower than that of ORe1.

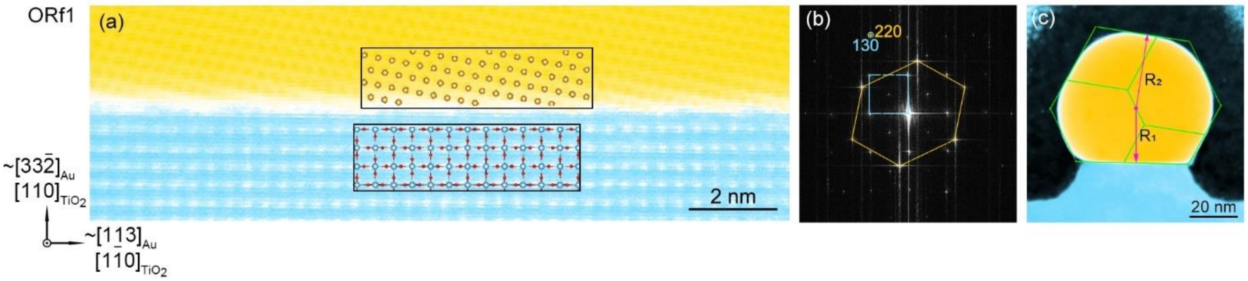

Figure 4.10 ORf1 interface viewed along $[1\bar{1}0]_{Au}//[001]_{TiO2}$ direction. (a) STEM-HAADF image of gold-rutile interface with the atomic models of gold and rutile inserted. (b) The FFT image of (a). (c) The morphology of the ORe1 particle and its modified Wulff construction. The images are color-coded to enhance the contrast. Blue, white, and golden colors represent the intensity of HAADF signal in an increasing order.

4.3 Discussion

4.3.1 Interface Orientation Relationship

Combining TEM and XRD measurement of ORs and theoretical calculations based on CSL theory, it is practical to presume that ORa-ORg are principal ORs at gold-rutile interface in this work despite lack of direct observations of ORd and ORg from TEM. The distribution of these ORs evolves intensely as dewetting temperature is increased. At 600 °C, $\{111\}_{Au}$ tends to be parallel with $\{110\}_{TiO_2}$, but in-plane directions are random. This texture is referred to as {111} out-of-plane texture here. At 800 °C, in-plane orientations are re-aligned and form a strong ORa texture with a minority of other irrational ORs such as ORe. As the temperature is increased to 1000 °C, the ORs could be indexed as ORa-ORg with comparable weight for each OR. Since all samples are slowly cooled down with identical procedures, this evolution of ORs is likely to be related with heating temperature.

Near-coincidence sites (NCS) theory can be used to calculate the distribution of good matched atoms at gold-rutile interface and confirm the validity of predicted ORa-ORg. When the two lattices at heterophase interface are incommensurate, it is difficult to form exact coincidence sites due to different lattice structure and mismatched lattice constant. Therefore, the concept of near coincidence sites was proposed to describe good matched atoms that have a distance less than a critical value. This is known as NCS lattice theory [109], a special case of CSL theory. Likewise, the density of NCSs which is defined by:

$$Density\ of\ NCSs = \frac{Number\ of\ NCSs}{Number\ of\ Ti\ atoms} \tag{4.2}$$

is related with the stability of the interface. Therefore, with NCS theory, the degree of atomic match at Au-TiO_2 interface was evaluated with *MATLAB* for various ORs by calculating the density of NCSs at interface. Following NCS theory, firstly, crystal lattices of Au and TiO_2 were constructed in three-dimensional space with a size of 120×120×50 Å. The origin was shared by Au and Ti. The initial OR was set to be ORc. Next, for each Ti in rutile lattice, the distance between Ti and all Au atoms in the space was calculated. If the distance was less than 15%|**b**|, where **b** = $\langle 110\rangle/2$**a** is the Burgers vector of Au, this Au-Ti pair was defined as a good matching pair with the midpoint of the two atoms being one NCS. The density of NCSs for ORc interface was then calculated within the boundary layer of 50×120×1 Å. Finally, with TiO_2 fixed, Au lattice was rotated about plane normal ($\langle 111\rangle_{Au}//[110]_{TiO_2}$) from 0° to 90° with an increment of 1° (including ORa-ORg) and the density of NCSs was calculated for each increment. Accordingly, the variation of NCSs density with rotation angle, i.e. OR, was obtained as shown by the black curve lines in Figure 4.11.

Since gold and rutile have unmatched symmetry and lattice constants, lattice misfit at the interface could be accommodated by applying a small constraint to either lattice to form exact lattice coincidence sites. This is known as CCSL theory. A high temperature provides a high mobility of Au atoms, leading to the constrained lattice favorable for selected ORs, which may be reserved during the cooling process. Herein, we manually applied constraints in order to achieve better lattice match. Constraints were applied to gold because rutile is much stiffer. The values of constraint on gold lattice were determined by perfectly matching the closest plane pairs derived from Figure 4.2. As listed in Table 4.1, a compression of 2.44% in gold was used as the constraint for ORa, ORb, ORe1, and ORe2, and an expansion of 0.76% was used for ORc, ORd, ORf1, ORf2, ORg1, ORg2 in CCSL theory.

Table 4.1 The closest reflections of gold and rutile in each pair with corresponding interplanar spacing and accordingly the constraints needed to be applied.

ORs	Au reflections	d-spacing /Å	TiO_2 reflections	d-spacing /Å	constraint
ORa	$(11\bar{2})$	1.6648	(220)	1.6243	-2.44%
ORb	$(\bar{2}\bar{2}4)$	0.8324	$(\bar{4}\bar{4}0)$	0.8121	-2.44%
ORc	$(\bar{4}\bar{4}2)$	0.6797	$(\bar{6}\bar{3}0)$	0.8121	0.76%
ORd	$(\bar{4}\bar{4}2)$	0.6797	$(\bar{3}60)$	0.6848	0.76%
ORe1	$(\bar{1}\bar{1}1)$	2.3544	$(\bar{2}00)$	2.2971	-2.44%
ORe2	$(\bar{1}\bar{1}\bar{1})$	1.4418	$(0\bar{2}0)$	1.4528	-2.44%
ORf1	(220)	2.0390	$(\bar{1}30)$	2.0545	0.76%
ORf2	(220)	1.6648	(310)	1.6243	0.76%
ORg1	$(00\bar{2})$	0.8324	$(2\bar{1}0)$	0.8121	0.76%
ORg2	$(00\bar{2})$	0.8156	$(\bar{1}\bar{2}0)$	0.8121	0.76%

Note: The lattice parameters for calculations are: a_{Au} = 4.078 Å, a_{TiO2} = 4.594 Å, c_{TiO2} = 2.959 Å.

Accordingly, the density of NCS, i.e. the degree of atomic match in the interface layer, was estimated for all ORs with variation in lattice constraints. Figure 4.11 presents the calculation results corresponding to CSL and CCSL theories. The distributions of NCSs from CSL and CCSL theories for each OR are illustrated in Appendix B. Based on CSL theory, ORa has the highest density of NCSs while ORc and ORd are local maxima. When a compression of 2.44% is applied to gold lattice, the densities of NCSs for ORa and ORe1-2 are greatly increased. In contrast, an expansion of 0.76% promotes the number of NCSs in ORf1-2 and ORg1 interfaces. These peaks show that with constraints applied, the density of NCSs can be significantly increased for the ORs reported here. These calculations confirm the validity of most preferential ORs predicted in reciprocal space in addition to the low occurrence of NCSs at ORb and ORg2 interface. Thus the appearance of these irrational ORs is likely to be associated with the accommodation of lattice misfit with interface strain. The exception of ORb and ORg2 indicates the limitation of this simple geometric model.

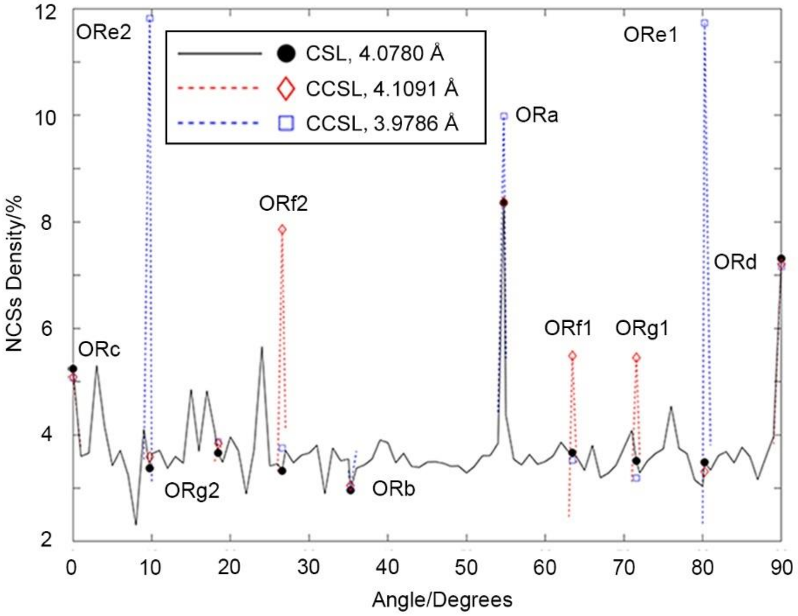

Figure 4.11 The density of NCSs for all gold-rutile interfaces that contain $\langle 1\ \bar{1}\ 0\rangle_{Au}//[0\ 0\ 1]_{TiO_2}$. Each OR corresponds to a rotation angle with respect to this axis. The black solid lines are calculated based on CSL theory with a lattice constant of 4.0780 Å. The red and blue dashed lines are from CCSL theory with lattice constant of 4.1091 Å (0.76% expansion) and 3.9786 Å (2.44% compression) respectively.

In terms of the temperature effect on OR evolution, it has been previously reported in a variety of systems. The {111} out-of-plane texture observed after heating at 600 ℃ has been reported for on many other substrates such as Si [110], glass [111], sapphire [112], and spinel [42]. For as-deposited polycrystalline metal films, texture of grains is related with many factors including the type of substrate, film thickness, deposition conditions, etc. When condensed at relatively low temperature such as room temperature, this texture is often encountered for FCC metal films such as gold with < 4° deviation from plane normal [113,114], while preferred in-plane orientation may not be expected. At higher temperature, gold films start to dewet including four stages: nucleation of holes, hole growth, hole coalescence and particle formation [115]. During this process, {111} out-of-plane texture can be further enhanced [116]. Niekiel et al. used in situ TEM to monitor the evolution of dewetting texture and morphology for 16 nm gold films on amorphous silicon nitride membranes [117]. In situ SAED experiments were performed during isothermal heating at 400 ℃, in which apparent intensity shift of diffraction rings were recorded within the first 10 minutes of heat treatment, indicating that grains with $\{111\}$ plane parallel to the substrate became predominant when dewetted at 400 °C.

The preference for this $\{111\}$ out-of-plane texture can be partially understood from aspects of energy. Interfacial energy (per unit interface area) is given by:

$$\gamma_{interface} = \gamma_{metal} + \gamma_{oxide} - W_{ad} \tag{4.3}$$

where γ_{metal} and γ_{oxide} are surface energies of metal and oxide, respectively, W_{ad} is the work of adhesion (energy cost to separate the two crystals). Accordingly, the value of interfacial energy is determined by the nature of both lattice planes. Although there is no accurate value of adhesion energy for various planes, both Au$\{111\}$ and $TiO_2\{110\}$ have low surface energy. Thus the contact of the two close-paced planes could be energy favorable.

As temperature increases to 800 °C, preferential in-plane orientation appears between gold and rutile. Such evolution of azimuthal orientations was previously reported for Au crystallites deposited on (1 1 1) MgO substrates [118], Ni clusters on mica after annealing of 15 nm nickel films at 410 °C [119], and Au particles obtained by annealing of Au films on SiO_2/Si(111) [110]. For 12 nm Au films deposited on rutile substrates, annealing at 775 K for 1 hour also produced this ORa texture [71], while in contrast for this work heat treatment at 600 °C (873 K) generates $\{111\}$ out-of-plane texture, and 800 °C (1073 K) gives rise to ORa. This difference in in-plane orientation may result from the shorter heating time (10 minutes) used in our experiments. Nonetheless, these results show that appropriate heat treatment can lead to pronounced ORa texture.

4.3.2 Interface Structure

To calculate the interface energy from Winterbottom analysis, $\{111\}_{Au}$ was chosen as the reference facet for all particles in this work, thus we have:

$$\gamma_{interface} = \gamma_{(110)TiO2} + \gamma_{(111)Au}\,\frac{R_1}{R_2} \tag{4.4}$$

from equation (3.3). The values of $\gamma_{(110)TiO2}$ and $\gamma_{(111)Au}$ adapted in this work were 0.33 J/m^2 and 1.283 J/m^2, respectively [64]. With R_1/R_2 ratios measured from TEM images, interface energies were estimated for all ORs and summarized in Table 4.2. Most of the interface energy reported in the literature is for ORa within a range of 0.9-1.2 J/m^2 [65]. Although reported values were measured corresponding to different approaches and surface conditions, our estimations from Winterbottom analysis fall within this range, indicating a relatively reliable measurement. Although the accuracy of measurement cannot be fully evaluated for other ORs due to lack of reference data, the values of R_1/R_2 could be compared with ORa to show the relative stability of each OR. Despite higher energy than ORa interface, ORb-ORg appear at temperature >800 ℃. This thermally activated OR transition is possibly associated with higher mobility of atoms and increased probability to overcome energy barriers from ORa to other ORs at high temperature.

Regarding the atomic structure of gold-rutile interface, three features are observed for these ORs including lock-in configurations, rearrangement of interfacial atoms, and interface voids. Viewed along close packed directions $[1\bar{1}0]_{Au}//[001]_{TiO2}$, rows of Au atoms tend to sit corresponding to rows of TiO_2 with certain periodicity. For ORa, Au atoms in closed packed $[1\bar{1}1]$ rows lock into every first row of $[001]_{TiO2}$ on $TiO_2(110)$ surface. In ORe1 and ORf1 the smallest width between Au rows is two and four spacings of TiO_2 $[001]_{TiO2}$, respectively. This structure is analogous to the lock-in model proposed by Fecht and Gleiter [120] which states that observed low-energy interphase boundaries between noble metals and ionic crystals correspond to an interface where close packed rows of atoms in the metal fit into the valleys between close packed rows in the ionic crystal. In some systems such as Au/Al_2O_3, low-energy boundaries of preferred ORs could be correlated with a high density of lock-in configurations. For Au/TiO_2 interfaces reported in this work, ORa has the highest density of lock-in structures, in accordance with its lowest interface energy. However, for ORe1 and ORf1 interfaces, ORe1 has a larger number of lock-in rows but larger R_1/R_2 and higher interface energy. This divergence suggests that other effects should be taken into account to understand the interfaces observed in experiment. From HAADF images, some Au atoms in the interfacial layer are missing in ORe1, while in ORb a transition layer between Au and TiO_2 is formed with atomic arrangement different from both lattices. In addition, mixing of Au and TiO_2 layers at the interface also indicates the reconstruction at Au-TiO_2 interface. Although it is difficult to construct accurate structure of interfaces especially interface reconstruction due to limitations of samples and instrument, interactions between the two lattices should not be neglected.

Finally, interface voids are observed in some ORa and ORe1 particles which have not been reported for gold films to the best of our knowledge. The appearance of interface voids during annealing was previously reported in dewetting of bilayer films. For instance, for porous Au particles produced from dewetting and dealloying of Au/Ag films, a second heat treatment led to closed holes in the particles through pore coalesce [121]. However, these pores could be trapped either in the particles or at the interface, the former of which was not observed in this experiment. Another example is the voids occurring during outerdiffusion and oxidation of Al in Au@Al core-shell particles supported on sapphire [122]. A reactive component and oxidation conditions were required to produce the irregular pores at the interface. In these cases, the formation of interface voids involves hole generation and aggregation. It is rude to conclude that voids in as-deposited Au films would have similar coarsening behavior and result in the voids at gold-rutile interface likewise because this feature is only observed in a few ORa and ORe1 particles. On the other hand, the number of gold particles examined in TEM is also limited so far especially those with irrational ORs. Thus the verification of correlation between interface voids, epitaxy relationship and heat treatment requires more work in the future.

4.4 Summary

In summary, we performed a systematic study on the interface between dewetted gold nanoparticles and rutile support. A few preferential orientation relationships were discovered and indexed to ORa-ORg through interpretation of XRD pole figures based on CSL predictions. Among them, the atomic structure of ORa, ORb, ORc, ORe1, and ORf1 were obtained from TEM observations, showing a lock-in feature of Au rows and atom rearrangement at the interface. The interface energy of these ORs was reflected by the R_1/R_2 ratio in Winterbottom analysis, from which ORa interface had the lowest energy. The distribution of ORs was greatly influenced by dewetting temperature from (111) out-of-plane texture at 600 ℃, to ORa-dominating texture at 800 ℃, to a considerable number of ORb-ORg at 1000 ℃. The appearance of these uncommon ORs could be partially explained by examining the degree of atomic match at interface based on CSL, CCSL and NCS theories. According to *MATLAB* calculations, NCSs densities of some ORs were promoted when constraints were applied to Au lattice. These results indicate that interface strain together with interface reconstruction are likely to play an important role in the ORs and atomic structure of gold-rutile interface.

Chapter 5 Gold-Rutile Interfaces at the Growth Front of Nanowires

In this chapter, we study the orientation relationships and structures at gold-rutile interface in the nanowires. Firstly, the structure and composition of nanowires are investigated with TEM in Section 5.1. Section 5.2 covers the orientation relationships between gold and rutile determined from electron diffraction. Section 5.3 shows typical atomic structure of the interface. A discussion on the growth mechanism of nanowires is included in Section 5.4, followed by a summary in Section 5.5.

5.1 Structure Identification of Nanowires

TEM and EDX analysis were exploited to characterize the structure and composition of as-grown nanowires in samples heat treated at 1000 °C for 60 minutes. Figure 5.1(a) shows the morphology of a typical nanowire which exhibits a bead-like shape. It consists of tens of beads stacking in the growth direction and a particle could be found at one end. With a fine spot scanning across another representative nanowire and a HAADF detector to collect large-angle scattered electrons, STEM-HAADF images can be obtained as presented in Figure 5.1(b) in which the particle shows a much brighter contrast than the body of the nanowire, implying heavier atoms within the particle. This contrast difference is consistent with the distribution of elements illustrated by the EDX mappings in Figure 5.1(c)-(d). Qualitative and quantitative analysis of the mapping data shows that the body of the nanowire is composed of Ti and O with an atomic ratio of 1 : 2, while the particle is mainly Au with a small but detectable fraction of Ti and O atoms. It is worth noting that a well-defined thin layer can be observed surrounding the gold particle, especially a small cluster at the surface as indicated by the red arrows in Figure 5.1(b). Relating the contrast of this layer, which is similar to the TiO_2 nanowire, and the minor Ti and O detected in the mappings of the particle, this layer is likely to be composed of Ti and O. Further quantification of composition for this layer is not applicable due to the low concentrations of Ti and O.

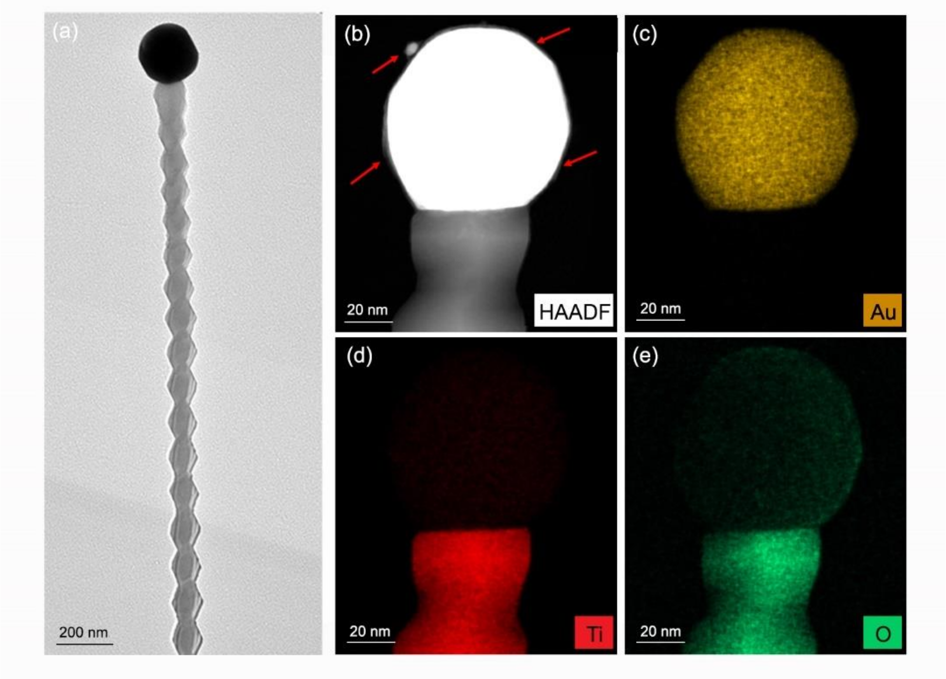

Figure 5.1 Morphology and composition mappings of nanowires. (a) The morphology of a typical nanowire. (b)-(d) STEM-HAADF images and corresponding elemental maps of Au, Ti, O of another nanowire to reveal the distribution of composition. The red arrows in HAADF images denote the layer at particle surface.

To identify the phases of these TiO_2 nanowires, electron diffraction experiments were carried out. The four diffraction patterns demonstrated in Figure 5.2(a)-(d) can be indexed to [001], [111], [112], and [113] zone axes of rutile respectively with a growth direction of [110]. Thus the structure of the nanowires is also rutile. An epitaxial relationship exists between rutile(110) substrates and vertical rutile nanowires growing in [110] direction. Taken together other nanowires observed at [100], [110], [101] zone axes, it can be found that there is a correlation between nanowire morphology and corresponding zone axis. Accordingly, a geometric model of the bead was constructed as shown in Figure 5.2(e)-(h). In this model, the bead is enveloped by eight {101} and four small {110} facets, all of which are low-energy surfaces in rutile [123]. No variation of diffraction patterns was detected when electron beam was positioned at different regions along the nanowires, indicating single-crystal rutile nanowires.

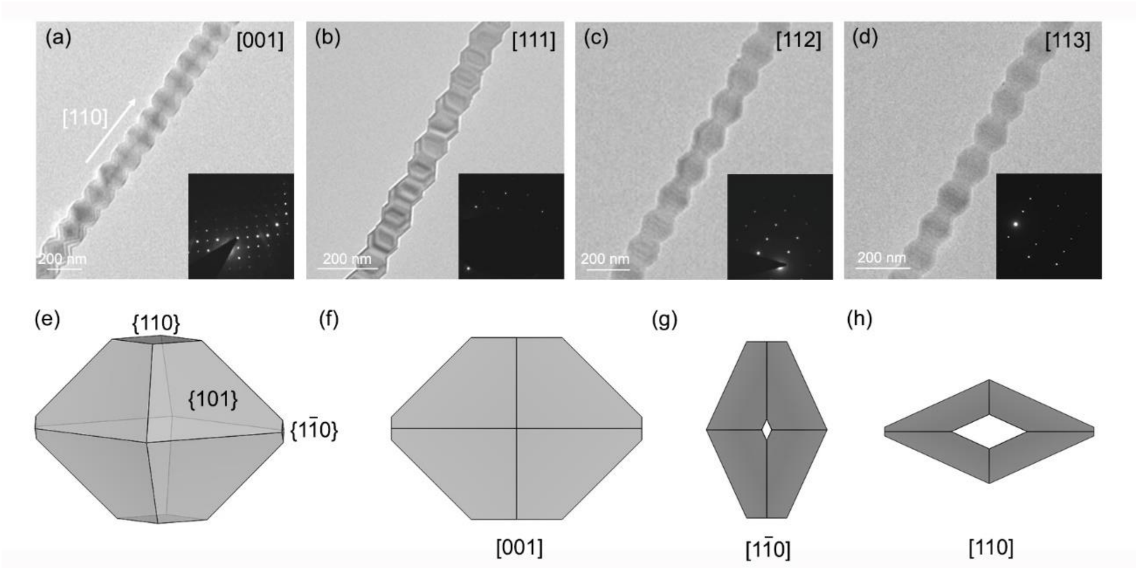

Figure 5.2 Morphology of nanowires at various zone axes and geometric model. (a)-(d) Morphology of nanowires at different zone axes. The electron diffraction patterns of corresponding nanowires are inserted corresponding to$[001]$, $[111]$, $[112]$, and $[113]$, respectively. (e) A three-dimensional model of individual bead in nanowires. (f)-(h) Projections of the model along $[001]$, $[1\bar{1}0]$, and $[110]$ directions, respectively.

5.2 Orientation Relationships at Gold-Rutile Interface

The structure and orientation relationships of gold-rutile interface in the nanowires could be obtained by HRTEM and SAED if: (i) the nanowires are appropriately orientated so that the electron beam is incident at specific zone axis, particularly those with low index; (ii) the thickness of the nanowires is thin enough to get HRTEM images of high quality. However, nanowires generally lie in random orientations on the copper grid, thus it is possible that low-index zone axes may not be tilted to for some of the nanowires due to the angle limit of double tilt holder. Therefore, it will be more efficient if certain criteria are used to select nanowires before further observations. Considering the structure of gold-rutile interface from Chapter 4 and the growth direction of rutile nanowires, the interface between gold particle and rutile nanowires should exhibit sharp features in TEM if it is edge-on at particular orientations, e.g. $[001]_{TiO2}$. In addition, as shown in Section 5.1, the projection of nanowires varies significantly when viewed along different zone axes. Thus the morphology of nanowires in the field of view can be used to indicate which zone axis they may be close to. Taking into account the diameter and shape of nanowires and the sharpness of gold-rutile interface, >15 nanowires were examined from which ORs between gold and rutile were determined.

In order to identify the OR between gold and rutile, first rutile nanowires were tilted to certain zone axis according to Kikuchi map in reciprocal space with corresponding diffraction patterns recorded with CCD camera. Next, the specimen was moved in x-y plane so that the Kikuchi pattern and diffraction pattern of gold particles could be obtained at the same tilt angles with rutile. Accordingly, the ORs were roughly interpreted. Nevertheless, depending on the OR and zone axis of rutile, different cases need to be considered for OR interpretation. The OR types discovered in the nanowires are listed below with the procedures of OR determination briefly introduced.

5.2.1 ORa

In 10 nanowires, when the nanowires were tilted to $[001]_{TiO2}$ zone axis, the diffraction patterns of gold particles could be indexed as $\langle 110\rangle_{Au}$ as shown in Figure 5.3(b)-(c). This $[001]_{TiO2}$ // $\langle 110\rangle_{Au}$ relationship follows the best-matched directions of gold and rutile as the ORa-ORg in Chapter 4. After indexing the hkl of each spot in the two diffraction patterns, the diffraction vector, **g**, in gold that was parallel to $\mathbf{g}_{110}$ in rutile was determined, which corresponded to the lattice plane parallel to growth front, $(001)_{TiO2}$. Consequently, $(111)_{Au}$ // $(110)_{TiO2}$was derived and this OR was interpreted as ORa. If rutile was also selected by the aperture, there would be contributions from rutile in the diffraction pattern of gold as presented in Figure 5.3(d), resulting in a superimposed pattern that contained two sets of reflections. But the identification of OR was the same as the first nanowire. Although nanowires may slightly deviate from accurate zone axis when acquiring diffraction patterns, this will not have great influence on the identification of ORs.

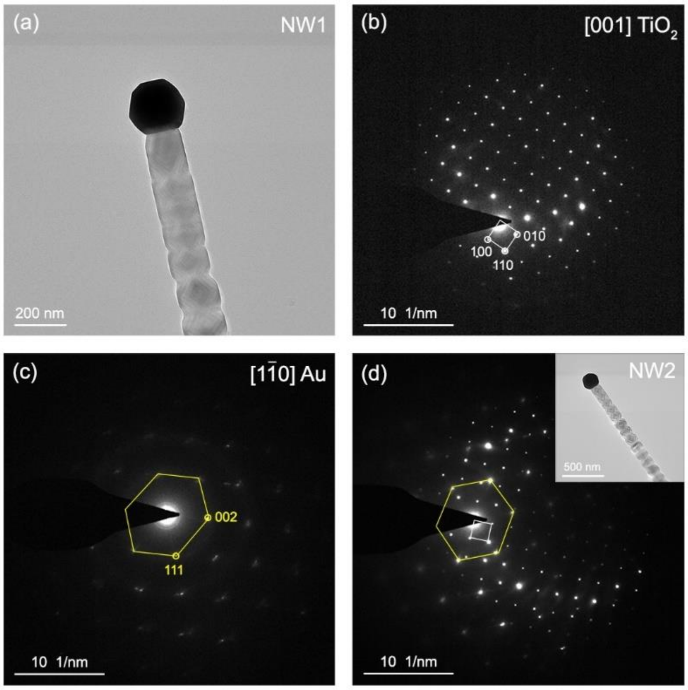

Figure 5.3 A typical ORa nanowire. (a) Morphology of nanowire 1, NW1. (b)-(c) Electron diffraction patterns from NW1. (d) Diffraction patterns of nanowire 2, NW2. The patterns were taken with the beam parallel to $\langle 1\bar{1}0\rangle_{Au}$ // $[001]_{TiO_2}$. The white square and yellow hexagon in (b)-(d) show the sets of rutile and gold, respectively.

5.2.2 ORe2

If rutile and gold were at low index zone axis besides $[001]_{TiO_2}$ and $\langle 1\bar{1}0\rangle_{Au}$, the OR derived from diffraction patterns might be different from ORa-ORg at first sight. However, in crystallography each OR can be expressed with a unique lattice transformation matrix so that different pairs of parallel planes and directions can be transformed between each other. As shown in Figure 5.4, the diffraction spots of gold and rutile give a relationship of

$(1\bar{1}\bar{1})_{Au}$ // $(010)_{TiO2}$, $[110]_{Au}$ //$[101]_{TiO2}$

if $\boldsymbol{g}_{1\,\bar{1}\,\bar{1}}$ of gold is rotated clockwise for ~2° with respect to $[110]_{Au}$. With TiO_2 as the reference, the direction parallel to $[001]_{TiO_2}$ and the plane parallel to $(110)_{TiO2}$ in gold lattice could be solved through lattice transformation with a OR matrix.

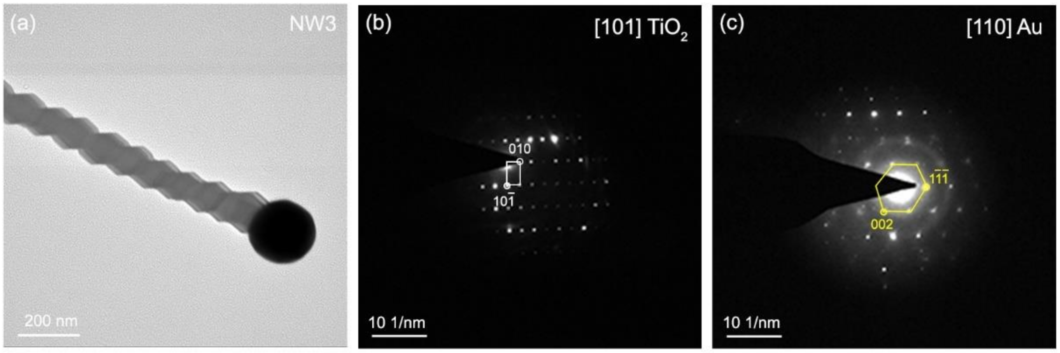

Figure 5.4 A typical ORe2 nanowire. (b)-(c) Electron diffraction patterns of nanowire 3 (NW3). The patterns were taken with the beam parallel to $[110]_{Au}$ $//[101]_{TiO2}$. The white rectangle and yellow hexagon in (d) show the reflection sets of rutile and gold, respectively.

The procedures to determine OR transformation matrices have been discussed by Fortes [124], and McHenry and Graef [125]. A detailed description is given in Appendix C. For the specific case of $(1\bar{1}\bar{1})_{Au}$ // $(010)_{TiO2}, [110]_{Au}$ $//[101]_{TiO2}$ here, transformation matrix $\boldsymbol{X}$ is:

$$\boldsymbol{X} = \begin{bmatrix} 0.7242 & 0.3316 & 0.3926 \\ 0.5127 & -0.5127 & -0.5127 \\ 0.0547 & 1.0011 & -0.9464 \end{bmatrix}$$

Thus this OR can be transformed to the equivalent one:

$(1.2369\ \overline{0.1811}\ \overline{0.1201})_{Au}$ // $(110)_{TiO2}$, $[0.0288\ 0.5266\ \overline{0.4979}\ ]_{Au}$ // $[001]_{TiO2}$

Although this index is not exactly identical with any of ORa-ORg obtained in last chapter, we can assign it to the closest OR. In this work, if the deviation of experiment OR from a perfect OR is within 4°, we assume that the two ORs are identical. For the OR here, it is closest to ORe2 with an angle of 2.78° between $[01\bar{1}\ ]_{Au}$ and $[0.0288\ 0.5266\ \overline{0.4979}\ ]_{Au}$ and 1.97° between $\left(4 + 3 \times \sqrt{2}\ \ \bar{1}\ \ \bar{1}\right)_{Au}$ and $(1.2369\ \overline{0.1811}\ \overline{0.1201})_{Au}$. Taking into account the ~2.3° rotation of gold reflections when determining the OR and measurement error from experiment patterns, it is reasonable to speculate that this OR is approximately ORe2.

5.2.3 ORf1

Figure 5.5 presents a nanowire that has two sets of reflections in the diffraction pattern of gold as shown by the yellow and white hexagons in Figure 5.5(c). This indicates the presence of

$\{111\}$ twins in the particle which agrees with the observations in rutile supported gold particles. The consistence between experimental and simulated patterns in Figure 5.5(d) further confirms that two domains with twinned relationship coexist in gold. If we define the yellow set as the matrix (represented by subscript ‘M’) and the white set as the twin (represented by subscript ‘T’), then the patterns in Figure 5.5(c) are indexed as $[1\bar{1}0]_M$ for the matrix and $[\bar{1}10]_T$ for the twin with a twinning plane of $(11\bar{1})_{M/T}$. Besides, the reciprocal vector corresponding to $(110)_{TiO2}$, i.e. $\boldsymbol{g}_1$ in Figure 5.5(b), is parallel to the $\boldsymbol{g}_2$ in Figure 5.5(c), from which the OR can be determined if $\boldsymbol{g}_2$ is figured out. Therefore an essential step is to rewrite $\boldsymbol{g}_2$ in the vector basis of both matrix and twin lattice.

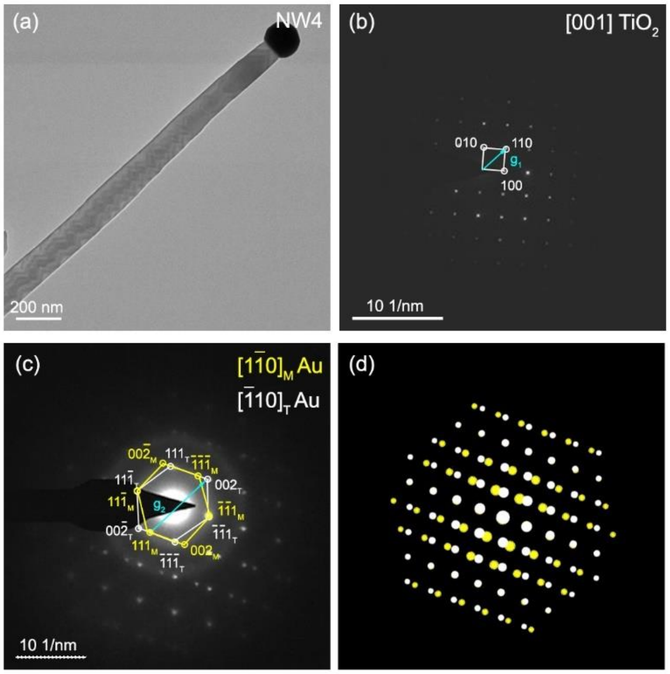

Figure 5.5 A typical ORf1 nanowire. (b)-(c) Electron diffraction patterns of nanowire 4 (NW4) which contains $\{111\}$ twin. The patterns were taken with the beam parallel to $\{1\bar{1}0\}_{Au}//[001]_{TiO_2}$. The white and yellow hexagons in (c) show the set of twin and matrix, respectively. (d) Superimposed pattern of simulated diffraction patterns of gold and rutile along zone axes of $[1\bar{1}0]_{Au}$ and $[\bar{1}10]_{Au}$, which is identical to the experiment pattern in (c). Subscripts ‘T’ and ‘M’ are used to label different domains with ‘T’ for the twin, and ‘M’ for the matrix.

Similar to the transformation matrix in last section, the OR between matrix and twin can also be described by a twinning matrix T which can be used to transform equivalent directions and planes in the two domains as:

$$[u_T;\ v_T;\ w_T] = T[u_M;\ v_M;\ w_M] \tag{5.1}$$

$$[h_T;\ k_T;\ l_T] = T[h_M;\ k_M;\ l_M] \tag{5.2}$$

where $[u;\ v;\ w]$ is the index for direction and $[h; k;\ l]$ is for lattice plane. Matrix for twinning on $(11\bar{1})$ in FCC system is given by Mahajan [126] as:

$$T = \frac{1}{3}\begin{bmatrix} -1 & 2 & -2 \\ 2 & -1 & -2 \\ -2 & -2 & -1 \end{bmatrix}$$

Thus the reflection of $(002)_T$ in the twin is transformed to $[h_M;\ k_M;\ l_M]$ in the matrix with:

$$[h_M;\ k_M;\ l_M] = T^{-1}[0; 0; 2] = [-\frac{4}{3};\ -\frac{4}{3};\ -\frac{2}{3}]$$

and vector $\boldsymbol{g}_2$ in the matrix ($\boldsymbol{g}_{2M}$) and the twin ($\boldsymbol{g}_{2T}$) are:

$$\boldsymbol{g}_{2M} == \left[-\frac{4}{3};\ -\frac{4}{3};\ -\frac{2}{3}\right] - [1;\ 1;\ 1] = [-\frac{7}{3};\ -\frac{7}{3};\ -\frac{5}{3}]$$

$$\boldsymbol{g}_{2T} = T\boldsymbol{g}_{2M} = [\frac{1}{3};\frac{1}{3};\frac{11}{3}]$$

As the twinning plane cannot be resolved from the TEM image due to the thick particle, it is difficult to identify which domain is adjacent to rutile nanowire. Thus there are two possibilities for OR at gold-rutile interface. The OR between rutile and the matrix domain of gold is defined as OR_M, and the OR between rutile and the twin domain is denoted by OR_T. OR_M and OR_T can be written as:

OR_M: $(\bar{1}\ \bar{1}\ \ \overline{0.7143})_{Au}//(110)_{TiO_2}, [1\bar{1}0]_{Au}//[001]_{TiO_2}$

OR_T: $(1\ \ 1\ \ 11)_{Au}//(1\ 1\ 0)_{TiO_2}, [\bar{1}10]_{Au}//[001]_{TiO_2}$

It is noteworthy that $(\bar{1}\ \bar{1}\ \ \overline{0.7143})_{Au}$ approaches $\left\{1\ 1\ \sqrt{2}/2\right\}_{Au}$ with a small angle of 0.23°. Thus we concluded that OR_M is indeed ORf1.

5.2.4 ORg2

For irrational ORs, it is usual that gold and rutile may be not at low-index zone axes at the same time. In this situation, Kikuchi maps can provide additional information on OR interpretation. One example is given in Figure 5.6. When rutile is at exact $[1\bar{1}0]_{TiO2}$ zone axis as indicated by the sharp diffraction spots and four-fold pattern of the zone, gold is not on zone axis as shown in Figure 5.6(d). But it can be seen that there is a low-index zone at bottom right which is beyond the screen even though a low camera length was used. Therefore the specimen was tilted in two directions, α and β, to reorient gold to this zone. From Figure 5.6(b)-(d) to Figure 5.6(e)-(g), 0.5° α tilt and 15° β tilt were applied to trace along band 2. During this tilt operation, it can be presumed that the nanowire is rotated around $[00\bar{1}]_{TiO_2}$ for about 15° to reach $[1\bar{1}0]_{Au}$ zone axis.

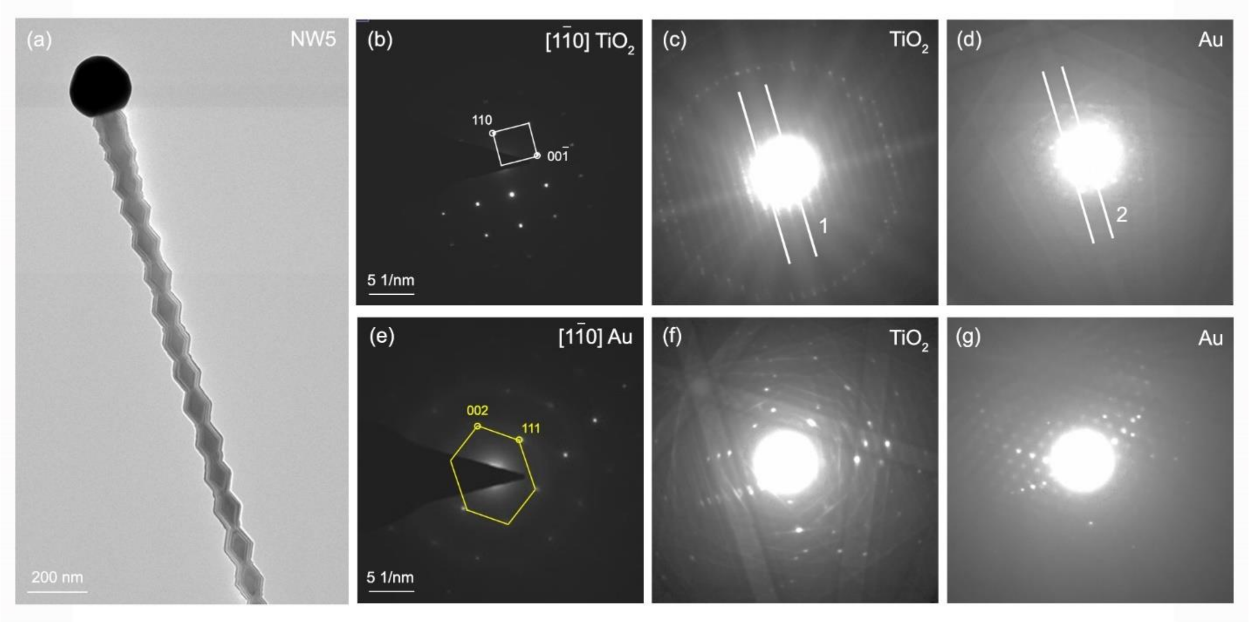

Figure 5.6 A typical ORg2 nanowire. (b)-(d) and (e)-(g) are recorded electron diffraction patterns and Kikuchi patterns of gold and rutile in nanowire 5 (NW5) at two different orientations.

Since it is not sure which direction the nanowire is rotated to, there are two possibilities as illustrated in Figure 5.7 in which the rotation direction is opposite for (a)-(b) and (c)-(d). For Figure 5.7(a)-(b), the vector in rutile that is parallel to $[1\bar{1}0]_{Au}$ after the rotation (labeled by $\boldsymbol{r}$) can be obtained by:

$$\boldsymbol{r} = [110]_{TiO2} + \tan(75°) \times [1\bar{1}0]_{TiO2} = [4.7321\ \ \overline{2.7321}\ \ 0]_{TiO2}$$

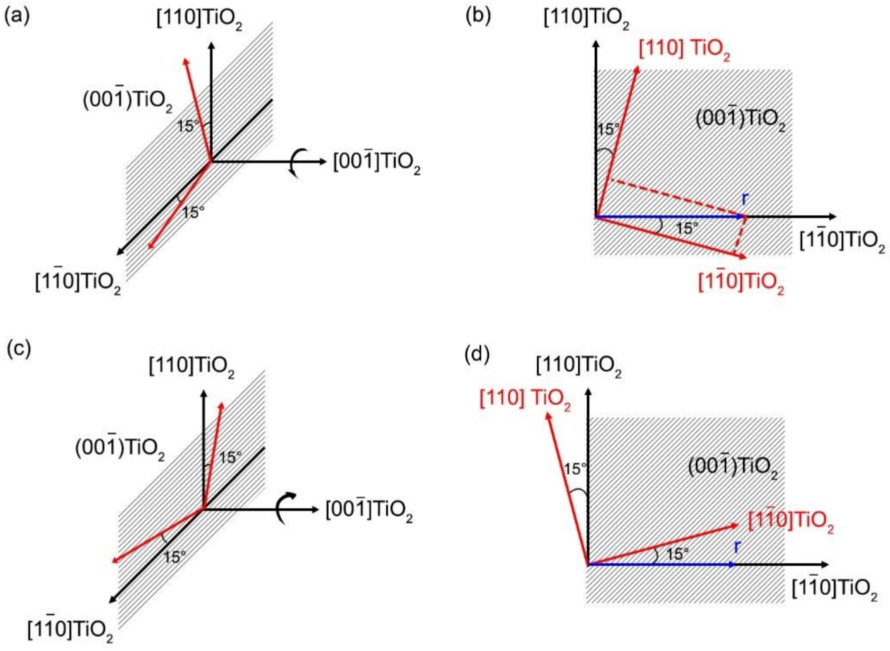

Figure 5.7 Scheme of the rotation of rutile around two opposite directions. Rutile can be rotated around two opposite directions (denoted by the arrows on $[00\bar{1}]_{TiO_2}$ axis) when gold is tilted to $[1\bar{1}0]_{Au}$ zone axis. (b) and (d) are projections of (a) and (c) when viewed along $[00\bar{1}]_{TiO_2}$ direction.

Then the OR between gold and rutile should be:

OR1: $(110)_{Au}\ //(00\bar{1})_{TiO_2}, [1\bar{1}0]_{Au}\ //\ [4.7321\ \ \overline{2.7321}\ \ 0]_{TiO2}$

Following Appendix C, corresponding transformation matrix is:

$$\boldsymbol{X_1} = \begin{bmatrix} 0.5438 & -0.5438 & 0.4440 \\ -0.3140 & 0.3140 & 0.7690 \\ -0.9749 & -0.9749 & 0 \end{bmatrix}$$

And accordingly OR1 can be converted to:

OR1: $(1\ \ \bar{1}\ \ 5.2785)_{Au}//(110)_{TiO_2}, [\bar{1}\bar{1}0]_{Au}//[001]_{TiO_2}$

Similarly, from Figure 5.7(c)-(d), OR2 is given by:

OR2: $(110)_{Au}\ //(00\bar{1})_{TiO_2}, [1\bar{1}0]_{Au}\ //\ [2.7321\ \ \overline{4.7321}\ \ 0]_{TiO2}$

$$\boldsymbol{X_2} = \begin{bmatrix} 0.3140 & -0.3140 & 0.7690 \\ -0.5438 & 0.5438 & 0.4440 \\ -0.9749 & -0.9749 & 0 \end{bmatrix}$$

And finally we can have:

OR2: $(\bar{1}\ 1\ \ 5.2785)_{Au}//(110)_{TiO_2}, [\bar{1}\bar{1}0]_{Au}//[001]_{TiO_2}$

By comparing with ORa-ORg, OR1 and OR2 are closest to ORg2. The angle between $(\bar{1}\ 1\ \ 5.2785)_{Au}$ and $\left(\bar{1}\ 1\ 3\sqrt{2}\right)_{Au}$ is 3.44°.

5.3 Structure of Gold-Rutile Interface

The structure of gold-rutile interface was further investigated with HRTEM. The rutile nanowire in Figure 5.8 was tilted to $[001]_{TiO2}$ and the OR between gold particle and the nanowire could be indexed to ORa from diffraction patterns. In HRTEM, image contrast, also known as phase contrast, originates from the interference between direct and scattered electron waves. This contrast is related with defocus conditions, thus the 'atoms' appearing in the image are not necessarily realistic atom columns. But lattice fringes in HRTEM images can still provide information on crystals. Figure 5.8(a)-(c) are arranged to show the overall morphology of the interface. Consistent with the observations in Figure 5.1, an adsorbates layer, which has been identified with a composition of TiO_x, is present on the surface of gold particle and near-interface region of rutile as indicated by the yellow arrows. The distance between adjacent lattice planes in the nanowire is 0.308 nm, close to the interplanar spacing of $(1\bar{1}0)_{TiO2}$ (0.325 nm). Region A and region B are enlarged in panel (d) and (e) to show the structure of the interface. Most of the Au atoms cannot be clearly resolved near the interface, probably due to the large thickness of the particle. Although the edge-on interface seems to be flat, it is not atomically sharp. In Region A, a transition can be observed from sharp area to diffused front with a height of several atomic layers. In region B, there is an enrichment near three phase boundary. The arrangement of 'atoms' in this enrichment is not perfect periodic with misorientation and local disorder at some sites. However, the interatomic distance measured for some atoms (0.316 nm) in this region is close to that of $(1\bar{1}0)_{TiO2}$. Such interface enrichment is likely to be associated with the growth of nanowires as will be discussed later.

The interface of other ORs is not presented here due to the thickness of gold and rutile which is not favorable for high-quality HRTEM imaging. The diameter of most nanowires investigated in TEM is 150-200 nm viewed along $[001]_{TiO_2}$. Although the thickness in beam direction is less according to the model of beads, it could still influence imaging quality. Therefore, only ORa interface has been carefully characterized at this stage.

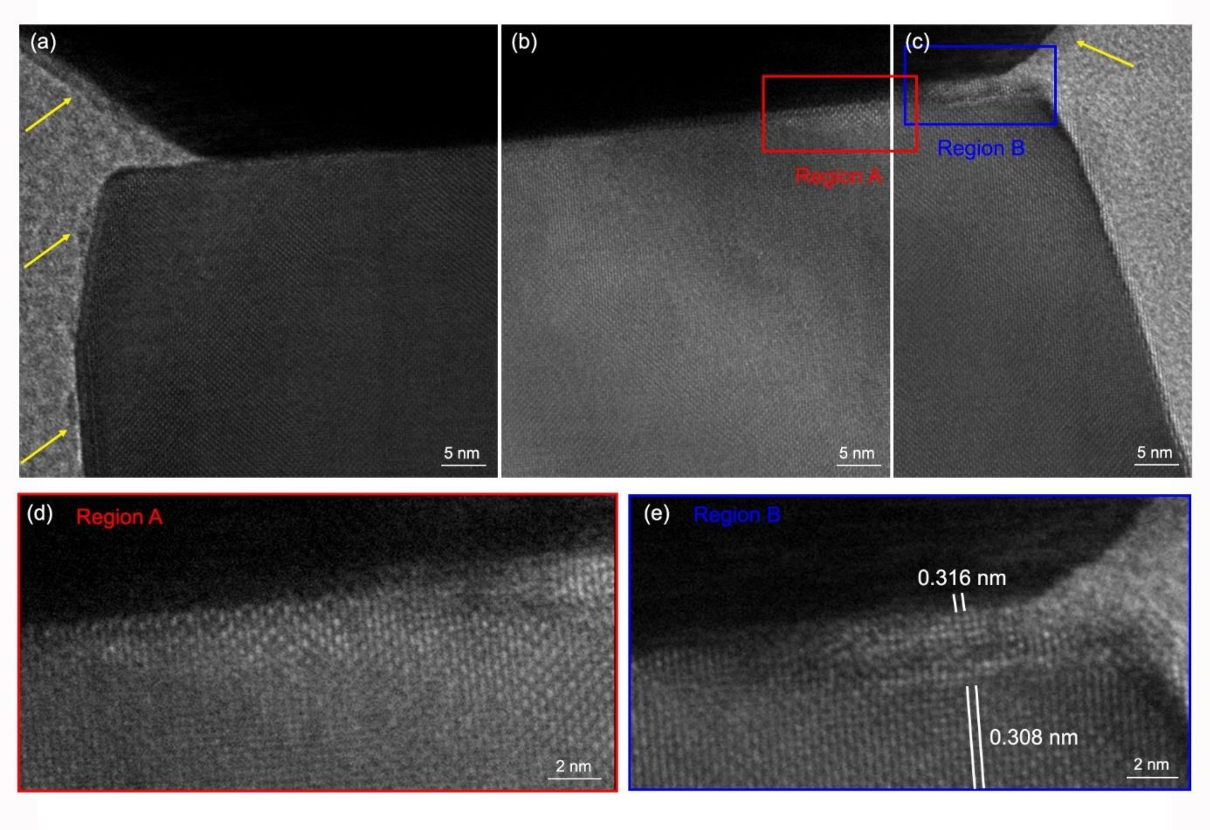

Figure 5.8 Structure of growth front in a typical nanowire. (a)-(c) HRTEM images of gold-rutile interface of an ORa nanowire viewed along $[001]_{TiO_2}$ direction. (d)-(e) correspond to Region A and Region B in panel (b) and (c). The yellow arrows show the TiO_x layer at the surface

5.4 Discussion

According to TEM investigations, the OR between gold and rutile in a majority of nanowires examined is ORa. Other irrational ORs including ORe2, ORf1, and ORg2 were also indexed within acceptable experiment errors. These ORs are consistent with the ORa-ORg found in rutile supported gold particles discussed in Chapter 4. It should also be noted that current interpretation of ORs only includes the nanowires examined in TEM. It is likely that other ORs in addition to

ORa, ORe2, ORf1, and ORg2 may also exist in the sample. Similar observations were found for gold particles dewetted at 1000 ℃ where there remained some weak spots in the pole figures that have not been identified so far. However, the number of these unknown ORs is significantly less than identified ORs in experiment observations, thus they are not focused on here. As for the fraction of ORa, for particles produced at 1000 ℃ the homogeneous distribution of pole intensity indicates a weak ORa texture, while for nanowires ORa is dominant with a ratio of ~60%. This implies less geometric confinement at gold-rutile interface in the nanowires compared to dewetted particles. The two types of gold/rutile samples were both prepared at 1000 ℃, but gas atmosphere and heating time were different: the particles were obtained in flowing Ar for 10 minutes, and the nanowires were heated for 60 minutes within an Ar-filled closed tube. Thus the difference in OR distribution may be associated with gas atmosphere and heat treatment. Nonetheless, the ORs observed in both samples belong to the predicted ORa-ORg, suggesting that gold-rutile interfaces in the two types of samples should be similar despite deficiency of direct evidence for interfaces in nanowires.

In terms of atomic structure, although Au atoms are not noticeable, the $(001)_{TiO_2}$ plane at the interface is generally sharp except regions near the triple line. Triple line is widely believed to be preferential nucleation sites in VLS-like growth of nanowires with a low Gibbs free energy in the formation of nucleus [31]. The enrichment observed in the interface supports that nucleation and growth of rutile nanowires are likely to be initiated at this boundary as well. Another important feature at the triple phase boundary is the TiO_x layer which extends from the surface of gold particle without crystalline structure. Similar coating layers have been reported in vapor growth of ZnO and TiO_2 nanowires which are believed to be associated with mass transfer of growth species on seed surface [48,57]. Within the closed quartz tube in our work, this TiO_x coating is likely to originate from thermal vaporization of TiO_2. At temperature >1800 ℃, Ti-O species including O, Ti, TiO, and TiO_2 have been reported in the decomposition products of TiO_2 [127,128]. Although growth temperature, i.e. 1000 ℃, is well below the melting point of TiO_2 (1843 ℃), the vapor products from thermal vaporization could also be produced consisting of Ti- and O-containing species, which are referred to as TiO_x here. These TiO_x vapors are likely to adsorb on the surface of gold as indicated by the presence of the Ti-O layer surrounding the particle. On the other hand, at 1000 ℃, which is close to the melting point of Au (1064 ℃), surface melting may occur at the surface of gold particles driven by minimization of surface energy [129]:

$$\gamma_{vs} > \gamma_{vl} + \gamma_{ls} \tag{5.3}$$

Where γ is interface energy, v, l, s represent for vapor, liquid, and solid phase, respectively. As a result, a quasi-liquid layer would appear on the surface of solid phase with higher disorder. The onset temperature of surface melting of gold nanoparticles is influenced by particle size. For example, for a gold particle with a size of 20 nm, surface melting was initiated at 827 K [130]. Therefore, for the >100 nm particles involved in this work, heat treatment at 1000 °C (close to the melting point of Au, 1064 °C) may also result in surface melting at gold surface. In conventional VSL-like growth, increased surface roughness is beneficial to the adsorption and accommodation of gaseous growth species on seed surface [31]. This further endorses the assumption that TiO_x is adsorbed and transported on gold surface. Consequently, we proposed a growth mechanism for rutile nanowires in this system: at high temperature, the vaporization products of TiO_2 adsorb on gold particles and transport along the surface to triple phase boundary where rutile nuclei will form and incorporate into pre-existing rutile lattice, leading to the growth of rutile nanowires at gold-rutile interface.

5.5 Summary

In this chapter, the interface between gold particles and rutile nanowires were investigated. Orientation relationships of ORa, ORe2, ORf1, and ORg2 were discovered at gold-rutile interface, agreeing with the ORs in rutile supported gold particles. HRTEM characterizations showed that gold particles were covered by TiO_x adsorbate layers. In addition, enrichment was observed at triple phase boundary. Accordingly, a mechanism based on surface adsorption and mass transfer was proposed to explain the growth of rutile nanowires under gold seeds.

Chapter 6 Interfaces between TiO_x Adsorbates and Gold Seeds

In order to further investigate the thin TiO_x overlayer on gold seeds, XAS was applied to examine the local environment of Au atoms in nanowire samples. The feasibility of differentiating interface gold from bulk gold within the seeds is assessed in Section 6.1. Data analysis of X-ray fine structure (XANE and EXAFS) data is included in Section 6.2 and Section 6.3, respectively. In Section 6.4, the characteristics of interfacial gold species is discussed based on XANES and EXAFS results. Section 6.5 summarizes major results of this chapter.

6.1 Feasibility Evaluation

Prior to XAFS experiment, the feasibility of XAFS measurement on nanowire samples was evaluated to theoretically estimate the possibility of resolving surface Au from bulk Au with XAFS spectrum. With the assumption that local environment of Au may show similarity to known stable Au- and Ti-containing phases such as Au-Ti alloys, preliminary simulations of XANES were carried out with a few known models of Au-Ti alloys. The models we considered are listed in Table 6.1. Spherical clusters with a radius of 6.0-6.6Å were created for each model with Au as the absorbing center, based on which theoretical XANES spectra of Au L3-edge were calculated using *FDMNES* code [103]. As shown in Figure 6.1(a), intense absorption appears near edge energy, giving rise to a strong peak known as whiteline. The range indicated by the dashed rectangle is enlarged in Figure 6.1(b), in which features of the whiteline change progressively from alloying Au to metallic Au, referred to as trend A here. As Au L3-edge corresponds to a $p \rightarrow d$ transition, XANES spectrum of Au L3-edge can probe unoccupied density of d states. The integration of absorption coefficient under the whiteline curve is related with the population of d holes [131]. Therefore, it can be seen that Au is losing d charges upon forming alloys with Ti, consistent with other Au-metal systems [132]. In contrast, this whiteline feature is suppressed in bulk Au due to the nominally full occupancy of the d states [133]. On the other hand, another trend, trend B, can be additionally observed in the first derivative of XANES. Both trends show the dependence of XANES on the structure of the models, likely the characteristics of Au-Ti bonding and the atomic ratio of Au and Ti in the alloys. Thus they can be used as indications to discern different types of Au-Ti interaction from XANES spectra.

Table 6.1 Summary of Au and Au-Ti alloy models for XANES simulations.

model	Formula	Space group	Au/Ti mole ratio	Reference
M1	Au	Fm-3m	-	Au foil
M2	AuTi	Pm-3m	1:1	Data-1510312
M3	AuTi	P63/mmc	1:1	Data-1510313
M4	AuTi$_3$	Pm-3n	1:3	Data-1510314
M5	AuTi$_3$	Pm-3m	1:3	Data-2310078

Note: All models come from Crystallography Open Database (COD) [134].

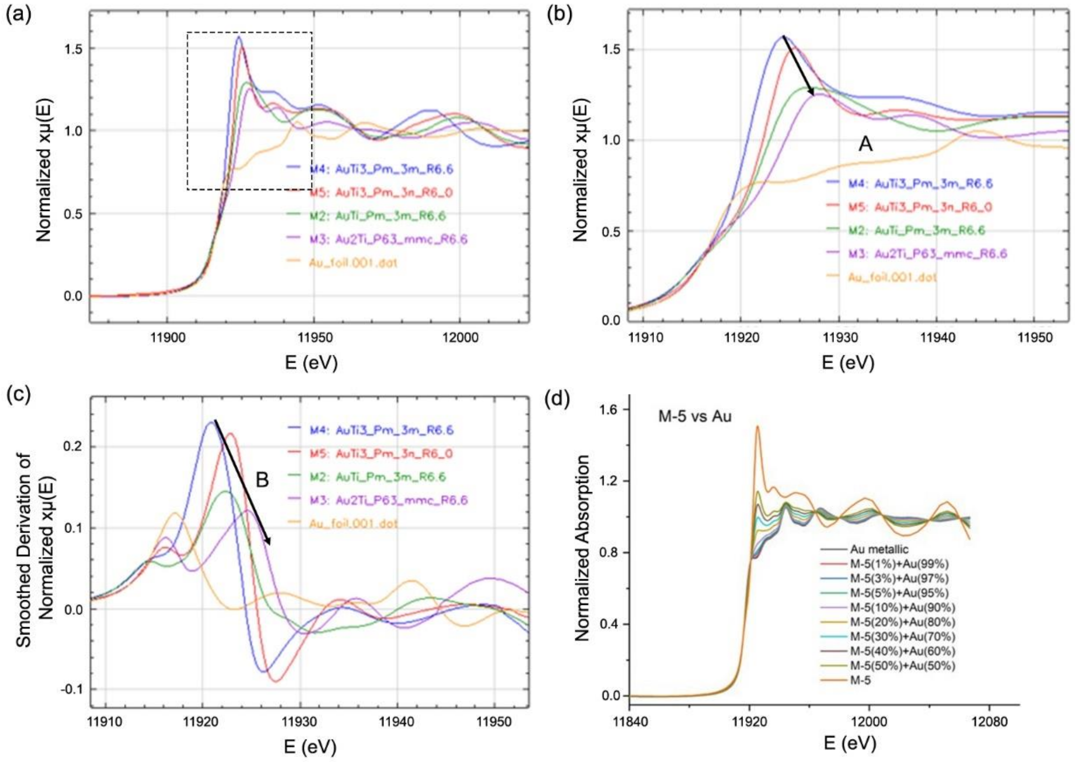

Figure 6.1 Simulated XANES spectra of various Au-Ti models. (a) Calculated XANES spectra of models M1 to M5. (b) Enlarged spectrum of (a). (c) The first derivative of XANES. (d) XANES spectra of Au and model M5 with various ratio. The simulations were performed with the help of Dr. Ning Chen from CLS.

Moreover, there are two contributions of Au L3-edge signals in this sample comprising surface Au near the interface and Au atoms inside the particle. Therefore a key problem is whether surface Au with a small weight can be clearly resolved. For this purpose, different ratios between Au-Ti alloy and metallic Au (M1) were tested for M2-M5 with the weight of Au-Ti alloy being 1%, 3%, 5%, 10%, 20%, 30%, 40%, and 50%, respectively. Figure 6.1(d) gives the calculation results based on metallic Au and M5. As the proportion of Au-Ti species increases in the mixture, the difference between simulated spectrum and that of Au or M5 becomes more significant, indicating that it is possible to identify the existence of a second phase in addition to Au, especially when the weight is >10%. These results show that it is feasible to identify a second type of Au from XANES spectrum even if it has a low weight.

6.2 XANES Data Analysis

The experimental Au L3-edge XANES spectra of reference Au foil (red) and Au/TiO_2 nanowire sample (blue) are presented in Figure 6.2. The reference spectrum of Au is consistent with those measured by Matsuo [135] and Benfield [133]. There are generally four distinct near-edge features in Au L3 XANES of Au-containing species, labeled by A, B, C, and D, respectively. Feature A corresponds to the whiteline, thus it is generally associated with the electronic structure and oxidation state of Au. In contrast, feature B-D reveals the extended local structure around the absorbing Au atoms. Comparing the experiment spectra of Au/TiO_2 sample and reference Au shown in Figure 6.2(a), evident difference is observed for the four features, suggesting that surface Au species can be well resolved from the bulk Au inside the particles. Based on the characteristics of features A-D, further information may be extracted from XANES. On the one hand, shift towards higher energy can be contributed by increased oxidation state or a smaller interatomic distance especially for 3d transition metals. On the other hand, the intensity and width of these peaks are influenced by the number of neighboring atoms around Au [133]. By plotting the first derivative of $x\mu(E)$ versus photon energy as shown in Figure 6.2(b), the two spectra have the same edge energy, which is defined as the position of the first maximum of the first derivative of XANES spectrum. Thus it is likely that changes in local environment of Au [136] play a more important role for the observed features.

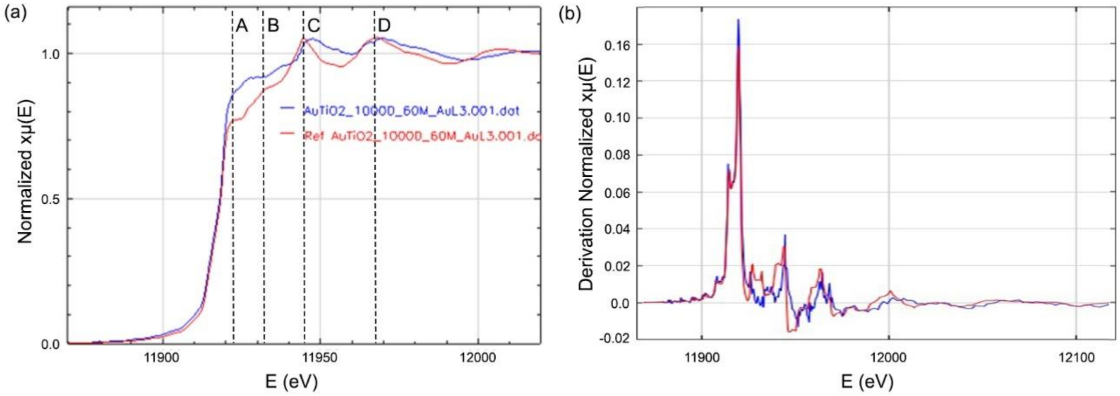

Figure 6.2 Experiment and reference XANES spectra. (a) Experiment XANES spectra of Au/TiO$_2$ specimen (blue) and reference Au foil (red). (b) First derivative of XANES spectra in (a).

In order to estimate possible Au species that contribute to the experiment XANES spectrum, linear combination fitting (LCF) was applied in *Athena* based on the simulated spectra of M1-M5 in Figure 6.1(a). The Energy range analyzed was 11890-11990 eV. LCF uses the linear combination of standard spectra, for example M1-M5 here, to reconstruct sample spectrum. For each possible combination, a sum spectrum is calculated and compared with sample spectrum. The statistical goodness of this fitting is described by a few parameters such as R-factor and reduced χ^2. The smaller the values, the better the fitting. Consequently, a combination that gives the best fit could be used to represent the components in the sample [137]. With this method, combinations satisfying following constrains were taken into account: (i) 5 variables were input including XANES spectra of model M1-M5 from experiment and simulations. (ii) Metallic Au must be contained due to its dominant weight over surface Au in the particle. (iii) The number of maximum components was limited to 4 to ensure a good fitting but with less calculations. Based on these constraints, all possible binary, ternary, and quaternary combinations were considered. The one with the smallest R-factor and reduced χ^2 was selected as the most likely interpretation of measured XANES spectrum.

After calculating all combinations, the best fit is given by M1, M4, and M5 as summarized in Table 6.2 based on 171 data points. As a result, metallic Au is dominating with a weight of 81%, consistent with the high fraction of core Au within the particle. The remaining 20% is composed of Au-Ti species of AuTi$_3$ with approximately 10% for each type. In practice, R factor values <

0.05 are considered to be a convincing fit. Therefore current fit should be reasonable considering the small values of fitting parameters.

Table 6.2 Fitting parameters of best fit combination in LCF.

Model	Crystallography					LCF		
	Formula	Space Group	Nearest Neighbor	CN	R	Weight	Error	E_0
M1	Au	Fm-3m	Au-Au	12	2.88	0.81	0.01	0.5
M4	$AuTi_3$	Pm-3m	Au-Ti	12	2.93	0.11	0.01	3.8
M5	$AuTi_3$	Pm-3n	Au-Ti	12	2.85	0.08	0.02	0.0

Note: For the fit, R-factor is 0.00029, χ^2 is 0.031, reduced χ^2 is 0.00019.

The spectra of experiment data, fitting results, and corresponding three models involved in the combination are further shown in Figure 6.3(a). Comparing the experiment spectrum (blue) and LCF fit (red) in Figure 6.3(a) and the difference spectrum (red) in Figure 6.3(b). Major difference between the two spectra lies in the region of feature C that is mostly contributed by Au-Au species. A peak shift to higher energy can be observed for feature C, which corresponds to a shorter averaged Au-Au distance compared to bulk Au. This indicates a compression of bond length between Au atoms, likely originating from Au near the surface. Despite the errors from peak C, the two spectra are well overlapped at low-energy range (< 11930 eV) where the major features of M4 and M5 are located. Thus the LCF results regarding Au-Ti species should be relatively reliable.

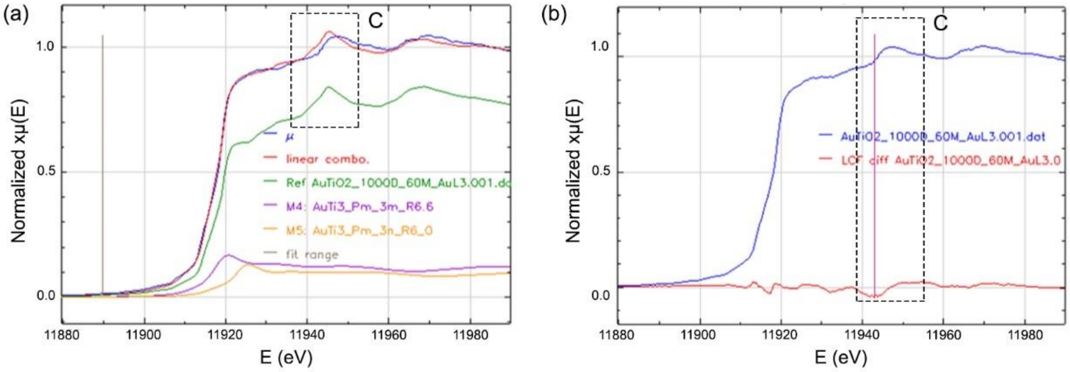

Figure 6.3 LCF fitting of experiment XANSE spectrum. (a) XANES spectra of Au/TiO_2 sample (blue), best fit given by LCF (red), and M1 (green), M4 (purple), and M5 (orange) in the linear

combination plotted with corresponding weight in the fit, namely 81% for M1, 11% for M4, and 8% for M5. (b) Measured XANES (blue) and difference spectrum (red) derived from sample and fitting spectrum.

The possibility of Au-O species was further examined by including Au_2O_3 in LCF. Among oxides of gold, Au_2O_3 was selected for following considerations [138,139]: (i) Au_2O_3 is the only stoichiometric binary compound of Au and O with known structure and sufficient stability. (ii) The XANES and EXAFS spectra of Au_2O_3 have been reported in the literature with good reproducibility. When Au_2O_3 is added to LCF calculations, the best fit from LCF analysis is shown in Figure 6.4 and Table 6.3. No significant change occurs for the best fit with a zero weight of Au_2O_3 in the fitting. These results reject the possibility of considerable Au-O species in Au/TiO_2 nanowire samples.

It should be noted that the accuracy of LCF in XANES analysis mainly depends on how well the standard spectra in the combination can represent the samples. Therefore, there may be other possibilities to interpret the XANES in addition to models M4 and M5. However, the semiquantitative analysis above provides a reasonable fitting concerning the existence of Au-Ti bonding at the interface.

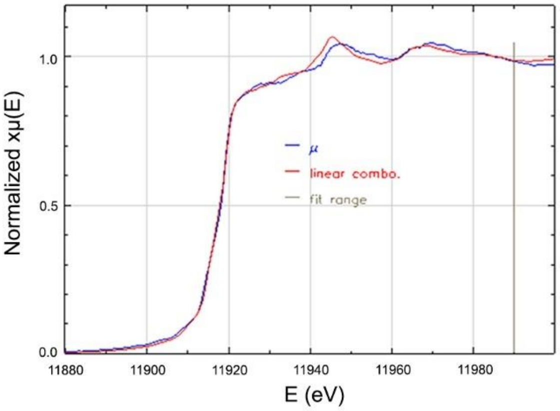

Figure 6.4 LCF fitting of experiment XANES spectrum with Au_2O_3 included. Blue curve is for Au/TiO_2 sample and red curve is for LCF calculations with Au_2O_3 considered.

Table 6.3 Fitting parameters of best fit combination in LCF with Au2O3 added.

Model	Crystallography					LCF		
	Formula	Space Group	Nearest Neighbor	CN	R(Å)	Weight	Error	E_0
M1	Au	Fm-3m	Au-Au	12	2.88	0.82	0.01	0.5
M4	$AuTi_3$	Pm-3m	Au-Ti	12	2.93	0.10	0.01	-3.8
M5	$AuTi_3$	Pm-3n	Au-Ti	12	2.85	0.08	0.02	0.0
M6	Au_2O_3	Fdd2	Au-O	6	1.93-2.90	0.00	N/A	N/A

Note: For the fit, 195 data points were included. R-factor is 0.00030, χ^2 is 0.033, reduced χ^2 is 0.00017.

6.3 EXAFS Data Analysis

Compared to XANES, quantitative analysis of EXAFS is more robust and gives detailed information on the local environment of Au atoms. The EXAFS of Au L3-edge in nanowire samples was analyzed in *WinXAS* after transforming $\chi(k)$ to R space. The k range of Fourier transform was 2.92-12.33 Å^{-1}. The Fourier filtering window was Gaussian function with a window parameter of 30%. From Figure 6.5(a), $\chi(k)$ decays quickly with increasing k, which makes it difficult to capture features in high-k range. Therefore, a k weight of 3 was applied to $\chi(k)$ and fitting analysis was performed on the k^3-weighted FT data in R space (Figure 6.5(b)). As shown in Figure 6.5(b), Fourier transform of $\chi(k)k^3$ consists of three shells, labeled by A, B, C respectively, within a radius of 6 Å. At larger distance, EXAFS generally contains less useful information due to featureless shells, thus they are not taken into consideration in spectrum fitting. For each shell in EXAFS, it is possibly contributed by multiple scattering paths around the absorber. For example, Table 6.4 gives 10 strong single scattering paths in model M1, M4, M5 (determined by XANES analysis above) calculated by *Feff* modelling of a 5 Å cluster. Multiple shell scattering is not taken into account here. The travel path, coordination number (CN), and distance (R) are listed in detail. One can see that path #1, #4, #7 contribute to shell A at approximately 2.5 Å, path #2, #5, #8 with a R close to 4 Å contribute to shell B, and the remaining path #3, #6, #9, #10 are related with shell C.

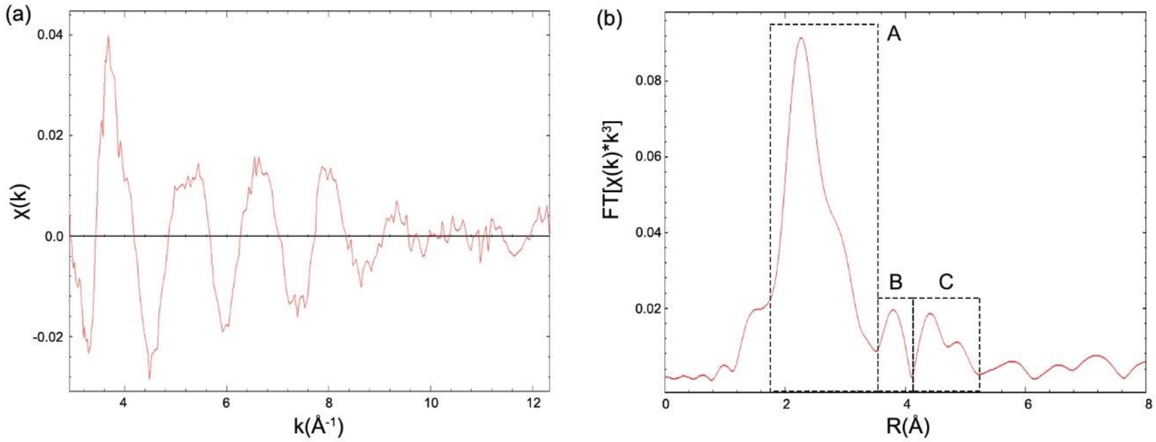

Figure 6.5 EXAFS $\chi(k)$ of sample spectrum in k space (a) and Fourier transform of k^3-weighted EXAFS (b). A, B, C shells are defined by the dashed rectangles.

Table 6.4 Scattering paths used in EXAFS fitting with Au as the absorber in models M1, M4, and M5.

Model	Formula/Space group	Scattering paths			
		Path #	Path ID	CN	R (Å)
M1	Au Fm-3m	1	Au-Au	12	2.88
		2	Au-Au	6	4.08
		3	Au-Au	24	4.99
M4	AuTi$_3$ Pm-3m	4	Au-Ti	12	2.93
		5	Au-Au	6	4.15
		6	Au-Ti	24	5.08
M5	AuT$_3$ Pm-3n	7	Au-Ti	12	2.85
		8	Au-Au	8	4.41
		9	Au-Ti	12	4.59
		10	Au-Au	6	5.10

On the basis of these paths, EXAFS data was refined and the fitting results were shown in Figure 6.6. The number of shells included in the fit was progressively increased from one shell (peak A, 3 paths used) to two shells (peaks A and B, 6 paths used), to three shells (peaks A, B, and C, 10 paths used). The final fit in R space and k space are shown in Figure 6.6(c)-(d). The good agreement between experiment and calculated spectra indicates a reasonable EXAFS fit. Comparing Table 6.4 and Table 6.5, the largest difference is observed for path #3 and path #4. The coordination number and length of path #3 are significantly reduced, suggesting a change in Au-Au bond likely from Au atoms at particle surface. In addition, the Au-Ti path (path #4) also experiences a shortening from 2.93 Å to 2.64 Å. This indicates a local distortion at the interface or a third Au-Ti phase may exist in the sample.

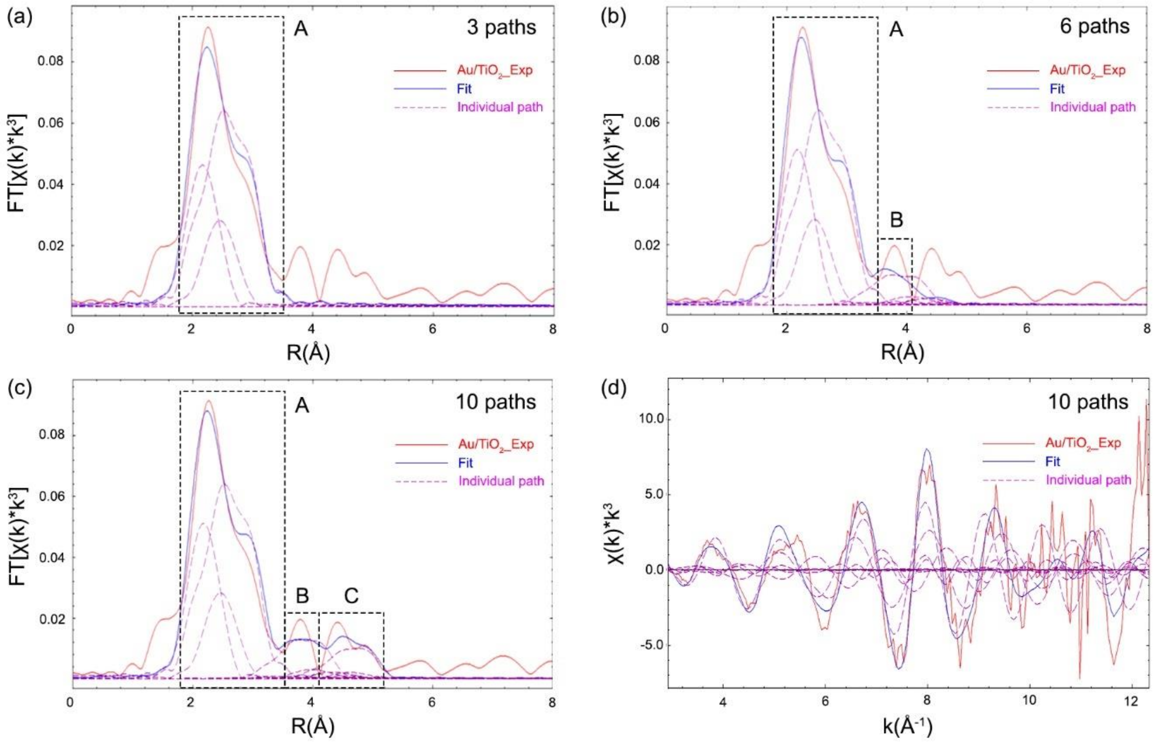

Figure 6.6 Fitting of experiment EXAFS spectrum with various paths. (a) Fitting of shell A with 3 paths (path #1, #4, #7). (b) Fitting of shells A and B with 6 paths (path #1, #2, #4, #5, #7, #8). (c)-(d) Fitting of shells A, B, and C with all 10 paths. (d) EXAFS fitting of all three shells in k space. The red curve and blue curve are for sample spectrum and fitting spectrum, respectively. The magenta dashed lines represent each component of the combination.

Table 6.5 Results of of k^3-weighted fitting of EXAFS in R space with all the 10 paths from M1, M4, and M5

Path #	Shell	CN	R(Å)	DW	E_0 shift (eV)	Area under paths
1	Au-Au	11.8	2.82	0.0100*	4.92377	100 %
2	Au-Au	5.8	4.03	0.0100*	4.92377	52.35 %
3	Au-Au	6.0	4.81	0.0089	4.92377	29.00 %
4	Au-Ti	11.6	2.64	0.0070	4.92377	20.52 %
5	Au-Au	6.0	4.14	0.0050	4.92377	4.696 %
6	Au-Ti	12.0	5.06	0.0060	4.92377	3.299 %
7	Au-Ti	12.0	2.93	0.0080	4.92377	15.21 %
8	Au-Au	8.2	4.49	0.0060	4.92377	2.538 %
9	Au-Ti	3.0	4.61	0.0100*	4.92377	0.533 %
10	Au-Au	2.0	5.07	0.0100*	4.92377	0.1879 %

Note: For this fitting, data point is 321. R range of fit is 1.17- 5.21Å. The initial set of E_0 shift is 4.9 eV. χ^2 is 44711.9, residual is 19.7, reduced χ^2 is 143.3.

6.4 Discussion

For gold particles at the top of nanowires, there are primarily three types of Au environment including: (i) the metallic Au inside the particle (dominated species); (ii) Au atoms at the growth front, i.e. Au-TiO_2 nanowire interface; (iii) Au atoms at Au-TiO_x adsorbates interface. Although the latter two types cannot be differentiated from XAFS data at present, they are both surface Au involving the interaction between Au and Ti, O. Thus we put them together and refer to as surface Au here. For surface Au, the contributions of type (ii) and type (iii) interfaces could be estimated from interface area. For simplicity the shape of Au particles is regarded as spherical cap, and growth front is treated as circular. Thus the surface area of type (iii) interface is approximately:

$$S_{iii} = 2\pi r^2(1 - cos\alpha) \tag{6.1}$$

where r is the radius of the sphere, α is the contact angle at triple phase boundary. The area of interface (ii) is given by:

$$S_{ii} = \pi r^2 (sin\alpha)^2 \tag{6.2}$$

According to TEM images of nanowires in Chapter 5, the contact angle is assumed to be 135°. With this contact angle, the contribution of interface (iii) is expected to be ~6 times higher than growth front.

From both XANES and EXAFS analysis, satisfactory spectrum fitting indicates that the sample may contain a majority of metallic Au (>80%) and two Au-Ti species (~10% for each) from $AuTi_3$. Only single-scattering paths with large probability were calculated in this study. The exclusion of Au_2O_3 suggests that surface Au tend to bond with Ti rather than O at the interface. This agrees with the Au-Ti-O stacking sequence for TiO_x film on Au(111) as reported by Wu et al [140]. Slight lattice contraction of Au is revealed by shift of feature C to higher energy in XANES, which is contributed by metallic Au, and shortening of Au-Au path in EXAFS fitting particularly the third shell, the distance reduction of which is 0.18 Å. Contraction of lattice is commonly observed for the shortest distance in small particles such as Au_{55} clusters compared to bulk values [141,142]. Shift of edge energy compared to Au foil is not found in XANES, indicating that the average valence of Au is close to zero. Similar feature was reported in Au/TiO_2 catalyst prepared by deposition-precipitation of Au on TiO_2 support with an Au content of 4.41 wt% and $Au/MgAl_2O_4$ and Au/Al_2O_3 catalyst prepared with the same method [84,143]. The chemical information of surface Au may provide insights on the interaction between Au and TiO_x adsorbates and further enhance the understanding of nanowire growth in this system.

6.5 Summary

In summary, the local environment of gold atoms at the seeds-adsorbates interface was investigated by measurement and analysis of Au L3-edge. XANES showed that Au atoms at the interface could be resolved from metallic Au in the seeds. With linear combination fitting on experiment spectrum, surface Au may consist of metallic Au and two $AuTi_3$ species without Au_2O_3. From EXAFS analysis the types of bond and corresponding parameters of each single-scattering path were determined. Comparing calculated paths with theoretical paths in adopted models, bond distance of Au-Au was contracted by 0.05-0.18 Å, and bond distance of Au-Ti was reduced by as much as 0.3 Å.

Chapter 7 Conclusions and Future Work

7.1 Conclusions

In this work, interfaces involved in the growth of rutile nanostructures mediated with gold seeds were investigated. Three interfaces in gold-rutile system were systematically studied including the orientation relationships, atomic structures and local bonding environment of gold atoms at the interface. Primary conclusions are drawn as follows.

For gold particles on rutile support, a few new and irrational orientation relationships were discovered in this work. The distribution of orientation relationships between gold and rutile showed strong dependence on heating temperatures. As heat treatment temperature increased from 600-1000 ℃ with a period of 10 minutes, orientation relationships evolved from {111} out-of-plane texture at 600 ℃, to dominating ORa at 800 ℃ and uniform distribution of ORa-ORg at 1000 ℃. By applying CSL and CCSL predictions and NCSs calculations on preferential ORs at gold-rutile interface, interpreted ORs corresponded to local maxima in the function of NCSs in terms of orientation of gold, thus the rationality of these appreciable uncommon ORs was justified.

The atomistics of a few ORs as obtained using STEM-HAADF imaging including ORa, ORb, ORc, ORe1, and ORf1, which provided detailed information on preferred ORs in gold-rutile system. Among these detected ORs, ORa interface had the lowest interface energy with a separation between interfacial Au and Ti-O layers. For other ORs lock-in configurations of gold rows on rutile surface could be observed at the interface. In addition, evident interface rearrangement of atoms occurred at ORb interface within a transition layer.

For rutile nanowires examined, the orientation relationships at gold-rutile interface were dominated by ORa with a minority of ORe2, ORf1, and ORg2. These nanowires were featured with TiO_x adsorbates layers on seeds surface and TiO_x enrichment at triple phase boundary, based on which a vapor-adsorbate-solid mechanism was proposed to explain the growth of nanowires. The role of gold surface in adsorption and transfer of TiO_x vapors to gold-rutile interface for nucleation and growth of rutile was highlighted.

The interface between TiO_x adsorbates and gold seeds was studied with XAS. LCF analysis of XANES spectrum revealed that surface gold atoms tend to form metallic bond with Ti instead of

O in the adsorbates. From the fitting results of EXAFS, the bond lengths of Au-Au and Au-Ti were slightly contracted compared to theoretical values in Au and $AuTi_3$ models. These results provided experiment evidence on the structure of gold-adsorbates interface which might be used as reference for the understanding of adsorption behavior.

7.2 Future Work

Although gold-rutile interface involved in this thermal growth system has been systematically studied, additional work needs to be performed to further clarify the growth behavior. Some experiments that can be extended in the future include:

(i) Interfacial voids at gold-rutile interface. Although interfacial voids have been found in some systems, the reported cases mainly involve complex fabrication process and a second element. However, for this gold-rutile system, the dewetting of gold is finished in a simple and common way. Considering our experiment conditions, the influence of temperature and interface epitaxy on the formation of interfacial voids should be further examined.

(ii) Atomistics of growth front in the nanowires. Due to the thickness of seeds and nanowires, it is difficult to obtain detailed atomic structure of growth front with current imaging resolution. Therefore, alternative methods should be developed to overcome this problem such as reducing the size of gold seeds to achieve thinner nanowires, or prepare thin specimens directly from current thick nanowires.

(iii) Interface structure at high temperature. Although preliminary results have been obtained for the structure of grow front, the observations were performed at room temperature for post-growth samples. Thus, they cannot fully represent the interface structure during nanowire growth. Therefore, in situ experiment of nanowire growth may need to be set up for direct observations of interfaces and growth at high temperature.

(iv) The structure of these interfaces needs to be further linked to the growth of rutile nanowires. For example, how interfacial ORs will influence the growth characteristics such as growth directions can be explored.

References

[1] M.A. Carpenter, S. Mathur, A. Kolmakov, Metal oxide nanomaterials for chemical sensors, Springer Science & Business Media, 2012.

[2] J. Mei, T. Liao, L. Kou, Z. Sun, Two-dimensional metal oxide nanomaterials for next-generation rechargeable batteries, Adv. Mater. 29 (2017) 1700176.

[3] K.-S. Lin, S. Chowdhury, Synthesis, characterization, and application of 1-D cerium oxide nanomaterials: a review, Int. J. Mol. Sci. 11 (2010) 3226–3251.

[4] Y. Yang, S. Niu, D. Han, T. Liu, G. Wang, Y. Li, Progress in developing metal oxide nanomaterials for photoelectrochemical water splitting, Adv. Energy Mater. 7 (2017) 1700555.

[5] J.A. Rodríguez, M. Fernández-García, Synthesis, properties, and applications of oxide nanomaterials, John Wiley & Sons, 2007.

[6] R.S. Wagner, W.C. Ellis, Vapor-liquid-solid mechanism of single crystal growth, Appl. Phys. Lett. 4 (1964) 89–90.

[7] Y. Ding, P.X. Gao, Z.L. Wang, Catalyst− nanostructure interfacial lattice mismatch in determining the shape of VLS grown nanowires and nanobelts: a case of Sn/ZnO, J. Am. Chem. Soc. 126 (2004) 2066–2072.

[8] S.Y. Li, C.Y. Lee, T.Y. Tseng, Copper-catalyzed ZnO nanowires on silicon (100) grown by vapor–liquid–solid process, J. Cryst. Growth. 247 (2003) 357–362.

[9] Y.H. Yang, Y. Feng, G.W. Yang, Experimental evidence and physical understanding of ZnO vapor-liquid-solid nanowire growth, Appl. Phys. A. 102 (2011) 319–323.

[10] S. Mathur, S. Barth, H. Shen, J. Pyun, U. Werner, Size-dependent photoconductance in SnO_2 nanowires, Small. 1 (2005) 713–717.

[11] S. Budak, G.X. Miao, M. Ozdemir, K.B. Chetry, A. Gupta, Growth and characterization of single crystalline tin oxide (SnO_2) nanowires, J. Cryst. Growth. 291 (2006) 405–411.

[12] X. Feng, K. Shankar, O.K. Varghese, M. Paulose, T.J. Latempa, C.A. Grimes, T. Pennsyl,

V. State, V. Uni, U. V Park, V. Pennsyl, Vertically aligned single crystal TiO_2 nanowire arrays grown directly on transparent conducting oxide coated glass : synthesis details and applications, Nano Lett. 8 (2008) 3781–3786.

[13] D.Y. Xie, M. Lin, W. Zhou, J. Wang, G. Zhu, Kinetically favorable vapor–adsorbate–solid growth of rutile nanowires, Small Methods. 3 (2019) 1900111.

[14] T.J. Trentler, K.M. Hickman, S.C. Goel, A.M. Viano, P.C. Gibbons, W.E. Buhro, Solution-liquid-solid growth of crystalline III-V semiconductors: an analogy to vapor-liquid-solid growth, Science. 270 (1995) 1791–1794.

[15] R.G. Hobbs, N. Petkov, J.D. Holmes, Semiconductor nanowire fabrication by bottom-up and top-down paradigms, Chem. Mater. 24 (2012) 1975–1991.

[16] K.A. Dick, A review of nanowire growth promoted by alloys and non-alloying elements with emphasis on Au-assisted III–V nanowires, Prog. Cryst. Growth Charact. Mater. 54 (2008) 138–173.

[17] N. Üzar, S. Okur, M.Ç. Arıkan, Investigation of humidity sensing properties of ZnS nanowires synthesized by vapor liquid solid (VLS) technique, Sensors Actuators A Phys. 167 (2011) 188–193.

[18] J.B. Park, N.-J. Kim, Y.-J. Kim, S.-H. Lee, G.-C. Yi, Metal catalyst-assisted growth of GaN nanowires on graphene films for flexible photocatalyst applications, Curr. Appl. Phys. 14 (2014) 1437–1442.

[19] S. Misra, L. Yu, M. Foldyna, P.R. i Cabarrocas, High efficiency and stable hydrogenated amorphous silicon radial junction solar cells built on VLS-grown silicon nanowires, Sol. Energy Mater. Sol. Cells. 118 (2013) 90–95.

[20] E.I. Givargizov, Fundamental aspects of VLS growth, in: Vap. Growth Ep., Elsevier, 1975: pp. 20–30.

[21] V. Schmidt, J. V Wittemann, S. Senz, U. Gösele, Silicon nanowires: a review on aspects of their growth and their electrical properties, Adv. Mater. 21 (2009) 2681–2702.

[22] V.A. Nebol’Sin, A.A. Shchetinin, Role of surface energy in the vapor–liquid–solid growth

of silicon, Inorg. Mater. 39 (2003) 899–903.

[23] T.I. Kamins, R. Stanley Williams, D.P. Basile, T. Hesjedal, J.S. Harris, Ti-catalyzed Si nanowires by chemical vapor deposition: Microscopy and growth mechanisms, J. Appl. Phys. 89 (2001) 1008–1016.

[24] S. Hofmann, R. Sharma, C.T. Wirth, F. Cervantes-Sodi, C. Ducati, T. Kasama, R.E. Dunin-Borkowski, J. Drucker, P. Bennett, J. Robertson, Ledge-flow-controlled catalyst interface dynamics during Si nanowire growth, Nat. Mater. 7 (2008) 372–375.

[25] C.-Y. Wen, M.C. Reuter, J. Tersoff, E.A. Stach, F.M. Ross, Structure, growth kinetics, and ledge flow during vapor− solid− solid growth of copper-catalyzed silicon nanowires, Nano Lett. 10 (2010) 514–519.

[26] Y.-C. Chou, W.-W. Wu, S.-L. Cheng, B.-Y. Yoo, N. Myung, L.J. Chen, K.N. Tu, In-situ TEM observation of repeating events of nucleation in epitaxial growth of nano $CoSi_2$ in nanowires of Si, Nano Lett. 8 (2008) 2194–2199.

[27] C.-Y. Wen, M.C. Reuter, J. Bruley, J. Tersoff, S. Kodambaka, E.A. Stach, F.M. Ross, Formation of compositionally abrupt axial heterojunctions in silicon-germanium nanowires, Science. 326 (2009) 1247–1250.

[28] S. Kodambaka, J. Tersoff, M.C. Reuter, F.M. Ross, Germanium nanowire growth below the eutectic temperature, Science. 316 (2007) 729–732.

[29] C.B. Maliakkal, D. Jacobsson, M. Tornberg, A.R. Persson, J. Johansson, R. Wallenberg, K.A. Dick, In situ analysis of catalyst composition during gold catalyzed GaAs nanowire growth, Nat. Commun. 10 (2019) 1–9.

[30] T. Akiyama, Y. Haneda, K. Nakamura, T. Ito, Role of the Au/GaAs (111) interface on the wurtzite-structure formation during GaAs nanowire growth by a vapor-liquid-solid mechanism, Phys. Rev. B. 79 (2009) 153406.

[31] B.A. Wacaser, K.A. Dick, J. Johansson, M.T. Borgström, K. Deppert, L. Samuelson, Preferential interface nucleation: an expansion of the VLS growth mechanism for nanowires, Adv. Mater. 21 (2009) 153–165.

[32] R.P. Sear, Nucleation at contact lines where fluid–fluid interfaces meet solid surfaces, J. Phys. Condens. Matter. 19 (2007) 466106.

[33] F. Glas, J.-C. Harmand, G. Patriarche, Why does wurtzite form in nanowires of III-V zinc blende semiconductors?, Phys. Rev. Lett. 99 (2007) 146101.

[34] C.-Y. Wen, J. Tersoff, K. Hillerich, M.C. Reuter, J.H. Park, S. Kodambaka, E.A. Stach, F.M. Ross, Periodically changing morphology of the growth interface in Si, Ge, and GaP nanowires, Phys. Rev. Lett. 107 (2011) 25503.

[35] V.G. Dubrovskii, Development of growth theory for vapor–liquid–solid nanowires: contact angle, truncated facets, and crystal phase, Cryst. Growth Des. 17 (2017) 2544–2548.

[36] S.N. Filimonov, Y.Y. Hervieu, Kinetic Model of the Initial Stage of the Nanowire Growth, Russ. Phys. J. 60 (2018) 2040–2043.

[37] P. Rueda-Fonseca, E. Bellet-Amalric, R. Vigliaturo, M. Den Hertog, Y. Genuist, R. André, E. Robin, A. Artioli, P. Stepanov, D. Ferrand, K. Kheng, S. Tatarenko, J. Cibert, Structure and morphology in diffusion-driven growth of nanowires: The case of ZnTe, Nano Lett. 14 (2014) 1877–1883.

[38] T. Majdi, G. Zhu, J. Carvalho, V. Jarvis, K. Meinander, J.F. Britten, G. Botton, J.S. Preston, Evidence for an equilibrium epitaxial complexion at the Au-$MgAl_2O_4$ interface, Appl. Phys. Lett. 107 (2015) 241601.

[39] V. Ghetta, D. Chatain, Morphologies Adopted by Al_2O_3 Single-Crystal Surfaces in Contact with Cu Droplets, J. Am. Ceram. Soc. 85 (2002) 961–964.

[40] W.D. Kaplan, D. Chatain, P. Wynblatt, W.C. Carter, A review of wetting versus adsorption, complexions, and related phenomena: the rosetta stone of wetting, J. Mater. Sci. 48 (2013) 5681–5717.

[41] D. Chatain, W.C. Carter, Spreading of metallic drops, Nat. Mater. 3 (2004) 843–845.

[42] F. Liu, D.Y. Xie, T. Majdi, G. Zhu, Twin-assisted growth of nominally stable substrates underneath dewetted Au nanoparticles, Mater. Charact. 113 (2016) 67–70.

[43] A. Yi, F. Liu, D.Y. Xie, M. Wen, G. Zhu, Gold-assisted growth of oxide bases underneath

dewetted gold nanoparticles, Mater. Charact. 151 (2019) 237–241.

[44] X. Duan, C.M. Lieber, General synthesis of compound semiconductor nanowires, Adv. Mater. 12 (2000) 298–302.

[45] Z.-Y. Zhou, Y. Ma, Q.-F. Han, Y.-L. Liu, Solubility, permeation, and capturing of impurity oxygen in Au/Ag: A comparative investigation from first-principles, Comput. Mater. Sci. 114 (2016) 79–85.

[46] S.H. Oh, M.F. Chisholm, Y. Kauffmann, W.D. Kaplan, W. Luo, M. Rühle, C. Scheu, Oscillatory mass transport in vapor-liquid-solid growth of sapphire nanowires, Science. 330 (2010) 489–493.

[47] S.R. Hejazi, H.R.M. Hosseini, M.S. Ghamsari, The role of reactants and droplet interfaces on nucleation and growth of ZnO nanorods synthesized by vapor–liquid–solid (VLS) mechanism, J. Alloys Compd. 455 (2008) 353–357.

[48] H. Simon, T. Krekeler, G. Schaan, W. Mader, Metal-seeded growth mechanism of ZnO nanowires, Cryst. Growth Des. 13 (2013) 572–580.

[49] F. Zhuge, T. Yanagida, K. Nagashima, H. Yoshida, M. Kanai, B. Xu, A. Klamchuen, G. Meng, Y. He, S. Rahong, Fundamental strategy for creating VLS grown TiO_2 single crystalline nanowires, J. Phys. Chem. C. 116 (2012) 24367–24372.

[50] G. Meng, T. Yanagida, K. Nagashima, H. Yoshida, M. Kanai, A. Klamchuen, F. Zhuge, Y. He, S. Rahong, X. Fang, Impact of preferential indium nucleation on electrical conductivity of vapor–liquid–solid grown indium–tin oxide nanowires, J. Am. Chem. Soc. 135 (2013) 7033–7038.

[51] H.M.M. Munasinghe Arachchige, D. Zappa, N. Poli, N. Gunawardhana, N.H. Attanayake, E. Comini, Seed-Assisted Growth of TiO_2 Nanowires by Thermal Oxidation for Chemical Gas Sensing, Nanomaterials. 10 (2020) 935.

[52] Y.-S. Park, J.-S. Lee, Morphology control of single crystalline rutile TiO_2 nanowires, Bull Korean Chem Soc. 32 (2011) 3571–3574.

[53] J.-Y. Ha, B.D. Sosnowchik, L. Lin, D.H. Kang, A. V Davydov, Patterned growth of TiO_2

nanowires on titanium substrates, Appl. Phys. Express. 4 (2011) 65002.

[54] J.-C. Lee, K.-S. Park, T.-G. Kim, H.-J. Choi, Y.-M. Sung, Controlled growth of high-quality TiO_2 nanowires on sapphire and silica, Nanotechnology, 17 (2006) 4317.

[55] J.-M. Wu, W.-T. Wu, H.C. Shih, Characterization of single-crystalline TiO_2 nanowires grown by thermal evaporation, J. Electrochem. Soc. 152 (2005) G613.

[56] R.S. Dariani, Z.N. Qaleh, Microstructure characterization of TiO2 $_{nano}$wires fabricated by thermal evaporation process, Thin Solid Films. 542 (2013) 192–198.

[57] M.H. Kim, J.M. Baik, J. Zhang, C. Larson, Y. Li, G.D. Stucky, M. Moskovits, A.M. Wodtke, TiO_2 nanowire growth driven by phosphorus-doped nanocatalysis, J. Phys. Chem. C. 114 (2010) 10697–10702.

[58] L. Vitos, A. V Ruban, H.L. Skriver, J. Kollar, The surface energy of metals, Surf. Sci. 411 (1998) 186–202.

[59] Y.-N. Wen, J.-M. Zhang, Surface energy calculation of the fcc metals by using the MAEAM, Solid State Commun. 144 (2007) 163–167.

[60] W.H. Baur, A.A. Khan, Rutile-type compounds. IV. SiO2, GeO2 and a comparison with other rutile-type structures, Acta Crystallogr. Sect. B Struct. Crystallogr. Cryst. Chem. 27 (1971) 2133–2139.

[61] H. Perron, C. Domain, J. Roques, R. Drot, E. Simoni, H. Catalette, Optimisation of accurate rutile TiO_2 (110),(100),(101) and (001) surface models from periodic DFT calculations, Theor. Chem. Acc. 117 (2007) 565–574.

[62] A. Kiejna, T. Pabisiak, S.W. Gao, The energetics and structure of rutile TiO_2 (110), J. Phys. Condens. Matter. 18 (2006) 4207.

[63] S.H. Overbury, P.A. Bertrand, G.A. Somorjai, Surface composition of binary systems. Prediction of surface phase diagrams of solid solutions, Chem. Rev. 75 (1975) 547–560.

[64] S. Sivaramakrishnan, J. Wen, M.E. Scarpelli, B.J. Pierce, J.-M. Zuo, Equilibrium shapes and triple line energy of epitaxial gold nanocrystals supported on TiO_2 (110), Phys. Rev. B. 82 (2010) 195421.

[65] F. Cosandey, Epitaxy, interfacial energy and atomic structure of Au/TiO_2 interfaces, Philos. Mag. 93 (2013) 1197–1218.

[66] W. Gao, A.S. Choi, J.-M. Zuo, Interaction of nanometer-sized gold nanocrystals with rutile (110) surface steps revealed at atomic resolution, Surf. Sci. 625 (2014) 16–22.

[67] N. Shibata, A. Goto, K. Matsunaga, T. Mizoguchi, S.D. Findlay, T. Yamamoto, Y. Ikuhara, Interface structures of gold nanoparticles on TiO_2 (110), Phys. Rev. Lett. 102 (2009) 136105.

[68] S. Ichikawa, T. Akita, M. Okumura, M. Haruta, K. Tanaka, M. Kohyama, Electron holographic 3-D nano-analysis of Au/TiO2 catalyst at interface, J. Electron Microsc. (Tokyo). 52 (2003) 21–26.

[69] C.M. Wang, Y. Zhang, V. Shutthanandan, S. Thevuthasan, G. Duscher, Microstructure of precipitated au nanoclusters in TiO_2, J. Appl. Phys. 95 (2004) 8185–8193.

[70] T. Ishida, T. Murayama, A. Taketoshi, M. Haruta, Importance of size and contact structure of gold nanoparticles for the genesis of unique catalytic processes, Chem. Rev. 120 (2019) 464–525.

[71] F. Cosandey, L. Zhang, T.E. Madey, Effect of substrate temperature on the epitaxial growth of Au on TiO_2 (110), Surf. Sci. 474 (2001) 1–13.

[72] X. Chen, W.P. Gao, S. Sivaramakrishnan, H.F. Hu, J.M. Zuo, In situ RHEED study of epitaxial gold nanocrystals on TiO_2 (110) surfaces, Appl. Surf. Sci. 270 (2013) 661–666.

[73] R. Lazzari, G. Renaud, J. Jupille, F. Leroy, Self-similarity during growth of the Au⁄ TiO_2 (110) model catalyst as seen by the scattering of x-rays at grazing-angle incidence, Phys. Rev. B. 76 (2007) 125412.

[74] T. Akita, K. Tanaka, S. Tsubota, M. Haruta, Analytical high–resolution TEM study of supported gold catalysts: orientation relationship between Au particles and TiO_2 supports, Microscopy. 49 (2000) 657–662.

[75] U. Diebold, The surface science of titanium dioxide, Surf. Sci. Rep. 48 (2003) 53–229.

[76] M. Yu, D.R. Trinkle, Au/TiO_2 (110) interfacial reconstruction stability from ab initio, J. Phys. Chem. C. 115 (2011) 17799–17805.

[77] Q. Wang, A.R. Oganov, Q. Zhu, X.-F. Zhou, New reconstructions of the (110) surface of rutile TiO_2 predicted by an evolutionary method, Phys. Rev. Lett. 113 (2014) 266101.

[78] P.G. Moses, A. Janotti, C. Franchini, G. Kresse, C.G. Van de Walle, Donor defects and small polarons on the TiO_2 (110) surface, J. Appl. Phys. 119 (2016) 181503.

[79] T. Akita, K. Tanaka, M. Kohyama, M. Haruta, HAADF-STEM observation of Au nanoparticles on TiO_2, Surf. Interface Anal. An Int. J. Devoted to Dev. Appl. Tech. Anal. Surfaces, Interfaces Thin Film. 40 (2008) 1760–1763.

[80] T. Akita, M. Kohyama, M. Haruta, Electron microscopy study of gold nanoparticles deposited on transition metal oxides, Acc. Chem. Res. 46 (2013) 1773–1782.

[81] W. Gao, S. Sivaramakrishnan, J. Wen, J.-M. Zuo, Direct observation of interfacial Au atoms on TiO_2 in three dimensions, Nano Lett. 15 (2015) 2548–2554.

[82] M. Mavrikakis, P. Stoltze, J.K. Nørskov, Making gold less noble, Catal. Letters. 64 (2000) 101–106.

[83] H. Chen, P. Li, N. Umezawa, H. Abe, J. Ye, K. Shiraishi, A. Ohta, S. Miyazaki, Bonding and electron energy-level alignment at metal/TiO_2 interfaces: A density functional theory study, J. Phys. Chem. C. 120 (2016) 5549–5556.

[84] T.V.W. Janssens, B.S. Clausen, B. Hvolbæk, H. Falsig, C.H. Christensen, T. Bligaard, J.K. Nørskov, Insights into the reactivity of supported Au nanoparticles: combining theory and experiments, Top. Catal. 44 (2007) 15.

[85] Z.-P. Liu, X.-Q. Gong, J. Kohanoff, C. Sanchez, P. Hu, Catalytic Role of Metal Oxides in Gold-Based Catalysts: A First Principles Study of CO Oxidation on TiO_2 Supported Au, Phys. Rev. Lett. 91 (2003) 266102.

[86] E. Wahlström, N. Lopez, R. Schaub, P. Thostrup, A. Rønnau, C. Africh, E. Lægsgaard, J.K. Nørskov, F. Besenbacher, Bonding of Gold Nanoclusters to Oxygen Vacancies on Rutile T iO_2 (110), Phys. Rev. Lett. 90 (2003) 26101.

[87] J. Guzman, S. Kuba, J.C. Fierro-Gonzalez, B.C. Gates, Formation of gold clusters on TiO_2 from adsorbed $Au(CH_3)_2$ $(C_5H_7O_2)$: Characterization by X-ray absorption spectroscopy,

Catal. Letters. 95 (2004) 77–86.

[88] D. Matthey, J.G. Wang, S. Wendt, J. Matthiesen, R. Schaub, E. Lægsgaard, B. Hammer, F. Besenbacher, Enhanced bonding of gold nanoparticles on oxidized TiO_2 (110), Science. 315 (2007) 1692–1696.

[89] Z. Jiang, W. Zhang, L. Jin, X. Yang, F. Xu, J. Zhu, W. Huang, Direct XPS evidence for charge transfer from a reduced rutile TiO_2 (110) surface to Au clusters, J. Phys. Chem. C. 111 (2007) 12434–12439.

[90] Y. Adachi, H.F. Wen, Q. Zhang, M. Miyazaki, Y. Sugawara, Y.J. Li, Elucidating the charge state of an Au nanocluster on the oxidized/reduced rutile TiO_2 (110) surface using non-contact atomic force microscopy and Kelvin probe force microscopy, Nanoscale Adv. (2020).

[91] S.J. Tauster, S.C. Fung, R.L. Garten, Strong metal-support interactions. Group 8 noble metals supported on titanium dioxide, J. Am. Chem. Soc. 100 (1978) 170–175.

[92] H. Tang, Y. Su, B. Zhang, A.F. Lee, M.A. Isaacs, K. Wilson, L. Li, Y. Ren, J. Huang, M. Haruta, Classical strong metal–support interactions between gold nanoparticles and titanium dioxide, Sci. Adv. 3 (2017) e1700231.

[93] S. Liu, W. Xu, Y. Niu, B. Zhang, L. Zheng, W. Liu, L. Li, J. Wang, Ultrastable Au nanoparticles on titania through an encapsulation strategy under oxidative atmosphere, Nat. Commun. 10 (2019) 1–9.

[94] J. Zhang, H. Wang, L. Wang, S. Ali, C. Wang, L. Wang, X. Meng, B. Li, D.S. Su, F.-S. Xiao, Wet-chemistry strong metal–support interactions in titania-supported Au Catalysts, J. Am. Chem. Soc. 141 (2019) 2975–2983.

[95] L. Liu, C. Ge, W. Zou, X. Gu, F. Gao, L. Dong, Crystal-plane-dependent metal–support interaction in Au/TiO_2, Phys. Chem. Chem. Phys. 17 (2015) 5133–5140.

[96] D.B. Williams, C.B. Carter, The transmission electron microscope, in: Transm. Electron Microsc., Springer, 1996, 3–17.

[97] B.B. He, Two-dimensional X-ray diffraction, Wiley Online Library, 2009.

[98] H. Grimmer, W. T Bollmann, D.H. Warrington, Coincidence-site lattices and complete pattern-shift in cubic crystals, Acta Crystallogr. Sect. A Cryst. Physics, Diffraction, Theor. Gen. Crystallogr. 30 (1974) 197–207.

[99] W.L. Winterbottom, Equilibrium shape of a small particle in contact with a foreign substrate, Acta Metall. 15 (1967) 303–310.

[100] J. Evans, X-ray absorption spectroscopy for the chemical and materials sciences, Wiley, Hoboken, NJ, 2018..

[101] J.A. Bearden, A.F. Burr, Reevaluation of X-ray atomic energy levels, Rev. Mod. Phys. 39 (1967) 125.

[102] M.L. Baker, M.W. Mara, J.J. Yan, K.O. Hodgson, B. Hedman, E.I. Solomon, K-and L-edge X-ray absorption spectroscopy (XAS) and resonant inelastic X-ray scattering (RIXS) determination of differential orbital covalency (DOC) of transition metal sites, Coord. Chem. Rev. 345 (2017) 182–208.

[103] Y. Joly, X-ray absorption near-edge structure calculations beyond the muffin-tin approximation, Phys. Rev. B. 63 (2001) 125120.

[104] A. Filipponi, Deconvolution of the lifetime broadening from X-ray absorption spectra of atomic and molecular species, J. Phys. B At. Mol. Opt. Phys. 33 (2000) 2835.

[105] H. Wang, M. Yen, X. Er, P. Liu, F. Wan, Y.-H. Chu, Q. Zhan, Self-assembled gold nanostructures in complex oxide thin films, Mater. Charact. 159 (2020) 110069.

[106] S. Yao, M. Wen, G. Zhu, Bimodal size distribution of dewetted gold nanoparticles with regrown oxide bases, Appl. Surf. Sci. 501 (2020) 144227.

[107] K. Momma, F. Izumi, VESTA 3 for three-dimensional visualization of crystal, volumetric and morphology data, J. Appl. Crystallogr. 44 (2011) 1272–1276.

[108] A. Halder, N. Ravishankar, Ultrafine single-crystalline gold nanowire arrays by oriented attachment, Adv. Mater. 19 (2007) 1854–1858.

[109] T.X.T. Sayle, C.R.A. Catlow, D.C. Sayle, S.C. Parker, J.H. Harding, Computer simulation of thin film heteroepitaxial ceramic interfaces using a near-coincidence-site lattice theory,

Philos. Mag. A. 68 (1993) 565–573.

[110] S. Vasisht, J. Shirokoff, Preferred orientations in nano-gold/silica/silicon interfaces, Appl. Surf. Sci. 256 (2010) 4915–4923.

[111] M. Kracker, W. Wisniewski, C. Rüssel, Textures of Au, Pt and Pd/PdO nanoparticles thermally dewetted from thin metal layers on fused silica, RSC Adv. 4 (2014) 48135–48143.

[112] R. Daudin, T. Nogaret, T.U. Schülli, N. Jakse, A. Pasturel, G. Renaud, Epitaxial orientation changes in a dewetting gold film on Si (111), Phys. Rev. B. 86 (2012) 94103.

[113] D. Faurie, P.-O. Renault, E. Le Bourhis, P. Goudeau, Study of texture effect on elastic properties of Au thin films by X-ray diffraction and in situ tensile testing, Acta Mater. 54 (2006) 4503–4513.

[114] Y. Golan, L. Margulis, S. Matlis, I. Rubinstein, Vacuum-Deposited Gold Films: II. Role of the Crystallographic Orientation of Oxide-Covered Silicon Substrates, J. Electrochem. Soc. 142 (1995) 1629.

[115] C. V Thompson, Solid-state dewetting of thin films, Annu. Rev. Mater. Res. 42 (2012) 399–434.

[116] C.M. Müller, R. Spolenak, Microstructure evolution during dewetting in thin Au films, Acta Mater. 58 (2010) 6035–6045.

[117] F. Niekiel, S.M. Kraschewski, P. Schweizer, B. Butz, E. Spiecker, Texture evolution and microstructural changes during solid-state dewetting: A correlative study by complementary in situ TEM techniques, Acta Mater. 115 (2016) 230–241.

[118] J.J. Métois, K. Heinemann, H. Poppa, Evidence of translations and rotations of gold crystallites vacuum deposited on (111) MgO surfaces at room temperature, Philos. Mag. A J. Theor. Exp. Appl. Phys. 35 (1977) 1413–1416.

[119] M. Reinbold, H. Hoffmann, Determination of orientation of small crystallites in thin nickel films on UHV-cleaved mica, Thin Solid Films. 32 (1976) 367–369.

[120] H.J. Fecht, H. Gleiter, A lock-in model for the atomic structure of interphase boundaries between metals and ionic crystals, Acta Metall. 33 (1985) 557–562.

[121] A. Kosinova, D. Wang, P. Schaaf, O. Kovalenko, L. Klinger, E. Rabkin, Fabrication of hollow gold nanoparticles by dewetting, dealloying and coarsening, Acta Mater. 102 (2016) 108–115.

[122] N. Gazit, G. Richter, A. Sharma, L. Klinger, E. Rabkin, Engineering of hollow $AlAu_2$ nanoparticles on sapphire by solid state dewetting and oxidation of Al, Mater. Des. 165 (2019) 107557.

[123] M. Ramamoorthy, D. Vanderbilt, R.D. King-Smith, First-principles calculations of the energetics of stoichiometric TiO_2 surfaces, Phys. Rev. B. 49 (1994) 16721.

[124] M.A. Fortes, Orientation relationships between two crystal lattices: matrix description, Acta Crystallogr. Sect. A Found. Crystallogr. 40 (1984) 642–645.

[125] M. De Graef, M.E. McHenry, Structure of materials: an introduction to crystallography, diffraction and symmetry, Cambridge University Press, 2012.

[126] S. Mahajan, Twinning matrices and their application in analyzing electron diffraction patterns from twinned bcc and fcc lattices, Metallography. 4 (1971) 43–49.

[127] A. Bronson, J. Chessa, An evaluation of vaporizing rates of SiO_2 and TiO_2 as protective coatings for ultrahigh temperature ceramic composites, J. Am. Ceram. Soc. 91 (2008) 1448–1452.

[128] W.O. Groves, M. Hoch, H.L. Johnston, Vapor–solid equilibria in the titanium–oxygen system, J. Phys. Chem. 59 (1955) 127–131.

[129] A. Kolmakov, M. Moskovits, Chemical Sensing and Catalysis By One-Dimensional Metal-Oxide Nanostructures, Annu. Rev. Mater. Res. 34 (2004) 151–180.

[130] X. Feng, K. Zhu, A.J. Frank, C.A. Grimes, T.E. Mallouk, Rapid charge transport in dye-sensitized solar cells made from vertically aligned single-crystal rutile TiO_2 nanowires, Angew. Chemie - Int. Ed. 51 (2012) 2727–2730.

[131] A. Bzowski, T.K. Sham, Electronic structure of Au–Ti intermetallics, J. Vac. Sci. Technol. A Vacuum, Surfaces, Film. 11 (1993) 2153–2157.

[132] A. Bzowski, Y.M. Yiu, T.K. Sham, Charge redistribution in Au-metalloid intermetallics: A

Au L 2, 3-edge X-ray-absorption study, Phys. Rev. B. 51 (1995) 9515.

[133] R.E. Benfield, D. Grandjean, M. Kröll, R. Pugin, T. Sawitowski, G. Schmid, Structure and bonding of gold metal clusters, colloids, and nanowires studied by EXAFS, XANES, and WAXS, J. Phys. Chem. B. 105 (2001) 1961–1970.

[134] S. Gražulis, A. Daškevič, A. Merkys, D. Chateigner, L. Lutterotti, M. Quiros, N.R. Serebryanaya, P. Moeck, R.T. Downs, A. Le Bail, Crystallography Open Database (COD): an open-access collection of crystal structures and platform for world-wide collaboration, Nucleic Acids Res. 40 (2012) D420–D427.

[135] S. Matsuo, T. Tsukamoto, A. Kamigaki, Y. Okaue, T. Yokoyama, H. Wakita, X-ray absorption spectroscopic study on gold particles formed on titania and alumina, X-Ray Spectrom. An Int. J. 32 (2003) 158–160.

[136] E.A. Willneff, S. Braun, S.L.M. Schroeder, Bridging the Material Gap between Model and Practical Au/TiO_x Catalysts Using X-ray Spectroscopies, Gold Bull. 37 (2004) 72.

[137] S. Datta, A.M. Rule, J.N. Mihalic, S.N. Chillrud, B.C. Bostick, J.P. Ramos-Bonilla, I. Han, L.M. Polyak, A.S. Geyh, P.N. Breysse, Use of X-ray absorption spectroscopy to speciate manganese in airborne particulate matter from five counties across the United States, Environ. Sci. Technol. 46 (2012) 3101–3109.

[138] N. Weiher, E.A. Willneff, C. Figulla-Kroschel, M. Jansen, S.L.M. Schroeder, Extended X-ray absorption fine-structure (EXAFS) of a complex oxide structure: a full multiple scattering analysis of the Au L3-edge EXAFS of Au_2O_3, Solid State Commun. 125 (2003) 317–322.

[139] H. Nitani, M. Yuya, T. Ono, T. Nakagawa, S. Seino, K. Okitsu, Y. Mizukoshi, S. Emura, T.A. Yamamoto, Sonochemically synthesized core-shell structured Au–Pd nanoparticles supported on γ-Fe_2O_3 particles, J. Nanoparticle Res. 8 (2006) 951–958.

[140] C. Wu, M.S.J. Marshall, M.R. Castell, Surface structures of ultrathin TiO_x films on Au (111), J. Phys. Chem. C. 115 (2011) 8643–8652.

[141] R.C. Thiel, R.E. Benfield, R. Zanoni, H.H.A. Smit, M.W. Dirken, The physical properties of the metal cluster compound $Au_{55}(PPh_3)_{12}Cl_6$, in: Struct. Biol. Eff., Springer, 1993, 1–39.

[142] H.-G. Fritsche, T. Büttner, Modification of the lattice contraction of small metallic particles by chemical and/or geometrical stabilization, Zeitschrift Für Phys. Chemie. 209 (1999) 93–101.

[143] T.V.W. Janssens, A. Carlsson, A. Puig-Molina, B.S. Clausen, Relation between nanoscale Au particle structure and activity for CO oxidation on supported gold catalysts, J. Catal. 240 (2006) 108–113.

Appendix A: Sample Preparation

For the fabrication of rutile nanowires, original samples, i.e., rutile substrates with deposited gold films, were sealed within a quartz tube. The procedures of tube sealing and heat treatment are illustrated in Figure A.1. First, a quartz tube with one end closed was placed horizontally. 1 cm was selected for the diameter of the tube so that rutile substrates could be accommodated to the tube. After placing the sample into the open end with a tweezer, the tube was slowly tilted to vertical direction, during which the sample would glide down to tube bottom. Next, the tube was connected to a vacuum system as shown by step ③ in Figure A.1. With valve 2 open and valve 1 closed, a mechanical pump was used to evacuate air in the system, followed by refilling of Ar after opening valve 1 and closing valve 2. Finally, tube sealing was completed with acetylene flame in regions far away from the sample. As a result, an enclosed tube filled with Ar could be obtained. For further heat treatment, the tube was transferred to a tube furnace. The position of the sample was adjusted to the center of the isothermal region of the furnace to provide a stable heating condition.

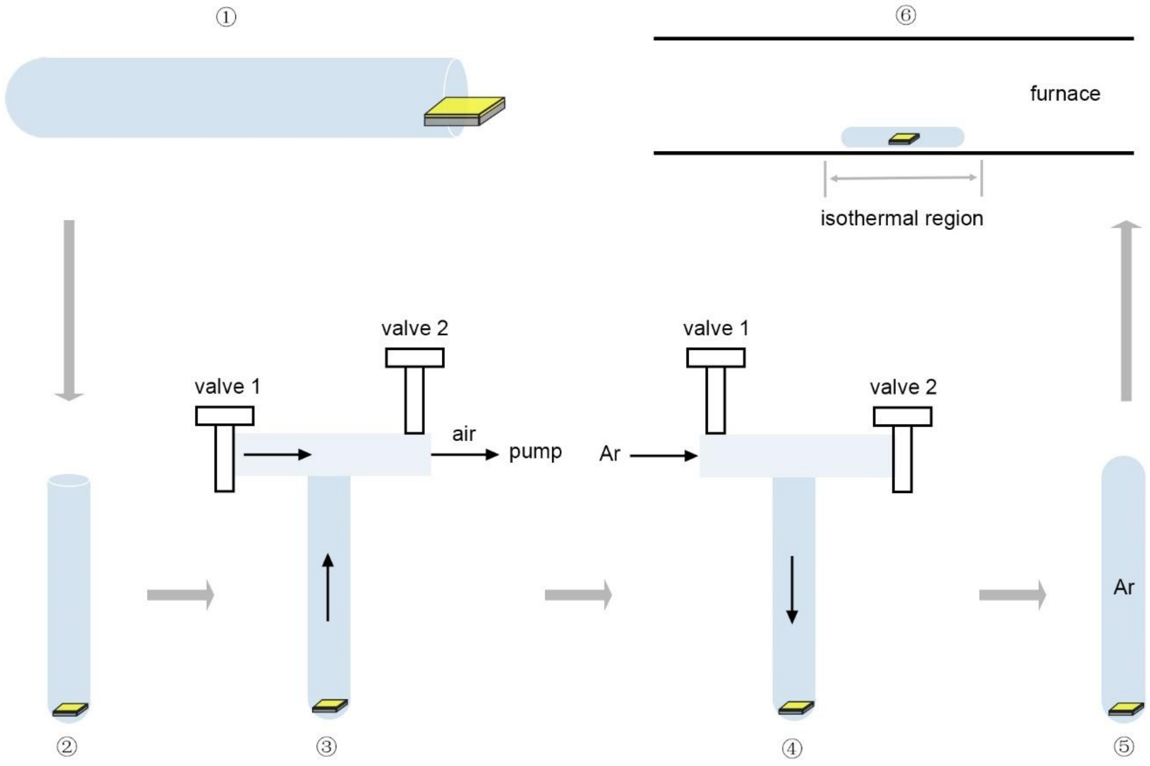

Figure A.1 Procedures of tube sealing and heat treatment.

Appendix B: Distribution of NCSs at Au-TiO_2 Interface for ORa-ORg

Figure B.1-B.3 present the distribution of Ti, O, Au and NCSs for ORa-ORg at various lattice parameters of Au. Figure B.1 is based on CSL theory with a lattice parameter of 4.0780 Å. Figure B.2-B.3 are from CCSL theory where constraints of -2.44% and 0.76% are applied to Au lattice respectively. The larger number of NCSs for CCSL-based calculations compared to that of CSL for some ORs indicates the validity of the predicted ORs.

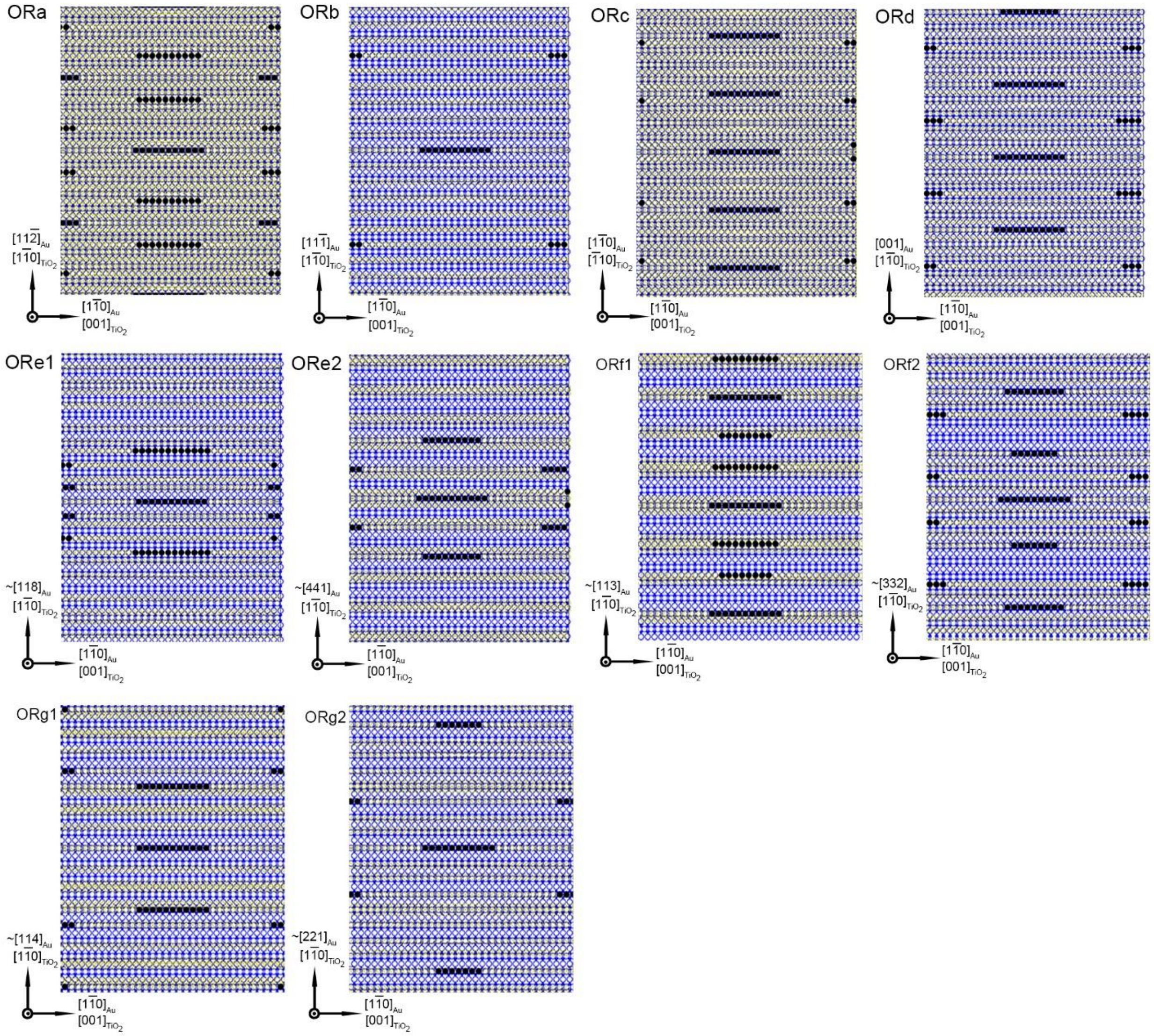

Figure B.1 The distribution of NCSs at gold-rutile interface calculated with CSL theory for ORa-ORg. The open yellow and blue circles represent atoms of Au and Ti, the solid blue circles represent O atoms, and the solid black circles are NCSs.

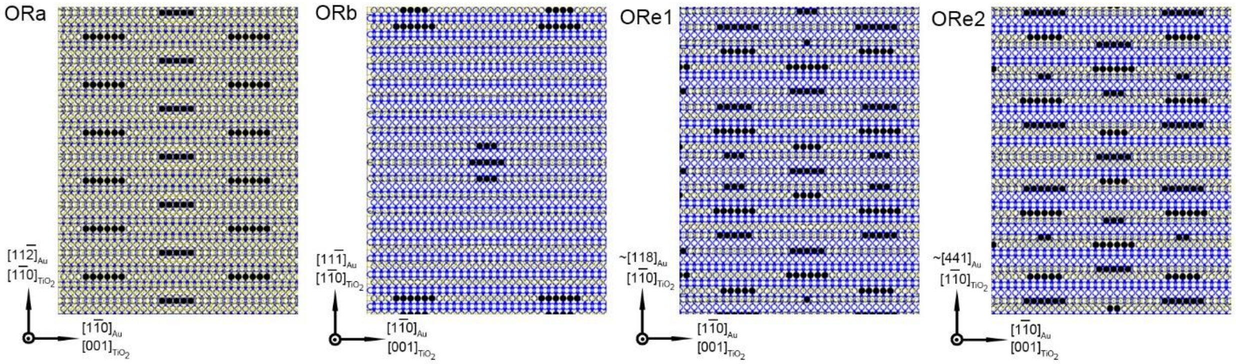

Figure B.2 The distribution of NCSs at gold-rutile interface calculated with CCSL theory for ORa-ORg. Au lattice was compressed with a lattice constant of 3.9786 Å. The open yellow and blue circles represent atoms of Au and Ti, the solid blue circles represent O atoms, and the solid black circles are NCSs.

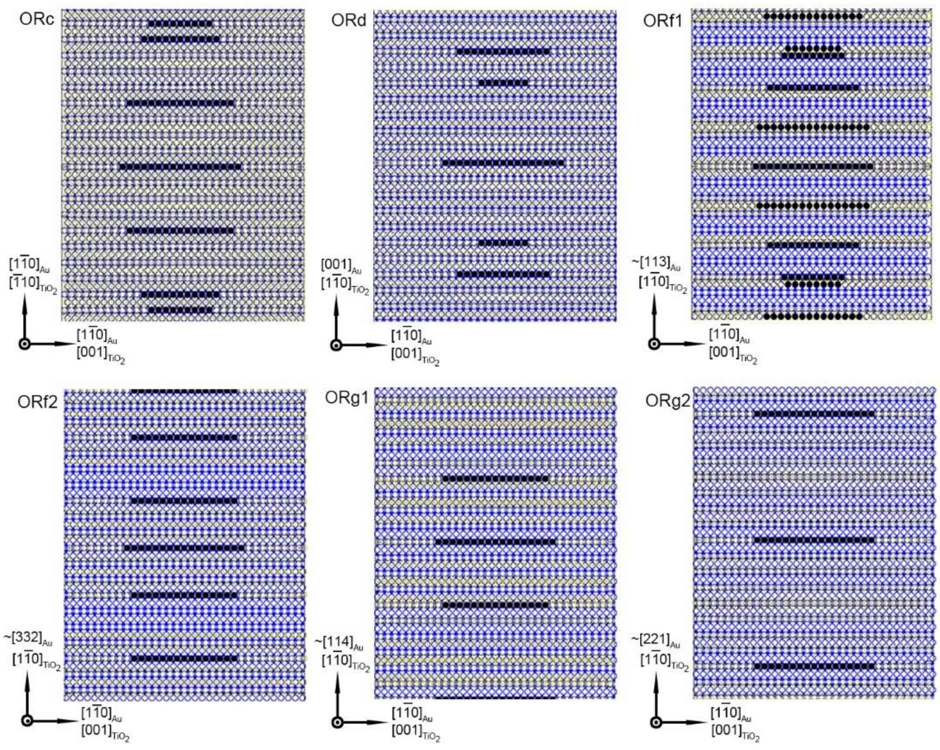

Figure B.3 The distribution of NCSs at gold-rutile interface calculated with CCSL theory for ORa-ORg. Au lattice was expaneded with a lattice constant of 4.1091 Å. The open yellow and blue circles represent atoms of Au and Ti, the solid blue circles represent O atoms, and the solid black circles are NCSs.

Appendix C: Transformation Matrix of Orientation Relationships between Au and TiO2

The procedures to determine OR transformation matrices are described here. A set of basis vectors were defined for each lattice with row vector $[\boldsymbol{e_1}\ \boldsymbol{e_2}\ \boldsymbol{e_3}]$ (denoted with $\boldsymbol{e}$ in the following text)for rutile and $[\boldsymbol{e'_1}\ \boldsymbol{e'_2}\ \boldsymbol{e'_3}]$ (denoted with $\boldsymbol{e'}$**)** for gold. Since any lattice vector in either direct or reciprocal space could be described by the bases, the 3×3 transformation OR matrix, X, relating the two lattice is given by:

$$[\boldsymbol{e'_1}\ \boldsymbol{e'_2}\ \boldsymbol{e'_3}] = [\boldsymbol{e_1}\ \boldsymbol{e_2}\ \boldsymbol{e_3}]\, X \tag{C.1}$$

or written as:

$$\boldsymbol{e'} = \boldsymbol{e}\, X \tag{C.2}$$

Then any direction in the lattice (denoted by $\boldsymbol{h}$) that could be expressed with crystallographic indices $[h_1;\ h_2;\ h_3]$ (column vector, denoted by h) is given by:

$$\boldsymbol{h} = \boldsymbol{e}h \tag{C.3}$$

Accordingly, the length of this vector, L, can be derived from:

$$L^2 = h^T G h \tag{C.4}$$

where G is a 3×3 matrix known as the metric matrix that is often used in crystallographic calculations. The expression of G depends on the crystal system and unit cell parameters $(a, b, c, \alpha, \beta, \gamma)$ of the crystal with a general form of:

$$G = \begin{bmatrix} a^2 & ab\ cos\,\gamma & ac\ cos\,\beta \\ ba\cos\gamma & b^2 & bc\cos\alpha \\ ca\ cos\,\beta & cb\ cos\,\alpha & c^2 \end{bmatrix} \tag{C.5}$$

Therefore the first condition for OR matrix, the parallel direction pairs, $[110]_{Au}\ //[101]_{TiO2}$ can be expressed with:

$$\boldsymbol{e'}h' = \lambda \boldsymbol{e}h \tag{C.6}$$

where λ is a value that represents the ratio of modulus for the two vectors. Combining equations (C.4) and (C.6) the value of λ can be obtained from:

$$h'^T G' h' = \lambda^2 h^T G h \tag{C.7}$$

Combining equations (C.2) and (C.6) gives an equation that contains X:

$$X h' = \boldsymbol{\lambda} h \tag{C.8}$$

The second condition for OR matrix, the pair of parallel planes, $[u_1;\ u_2;\ u_3]$ (column vector, denoted by u), e.g. $[1; -1; -1]_{Au}$ // $[0; 1; 0]_{TiO2}$ here, can be considered in similar way if reciprocal vectors were used to describe lattice planes. The reciprocal basis vector, $\boldsymbol{r}$, which is $[\boldsymbol{r_1}\ \boldsymbol{r_2}\ \boldsymbol{r_3}]$, is related with $\boldsymbol{e}$ through:

$$\boldsymbol{r} = \boldsymbol{e} G^{-1} \tag{C.9}$$

Therefore the parallel relationship of the two planes can be written as:

$$\boldsymbol{r}' u' = \mu \boldsymbol{r} u \tag{C.10}$$

$$X G'^{-1} u' = \mu G^{-1} u \tag{C.11}$$

Similar to (C.7), the value of μ is calculated with the equation below in which G^{-1} is the metric matrix of reciprocal lattice:

$$u'^T G'^{-1} u' = \mu^2 u^T G^{-1} u \tag{C.12}$$

In addition the previous two conditions, a third one can be established based on the direction perpendicular to the parallel direction and plane normal as $\boldsymbol{y}$ and $\boldsymbol{y}'$, and they are supposed to be parallel too. This can be realized by cross product of the other two vectors. First transform the reciprocal vector of the plane to a vector in direct space, $\boldsymbol{k}$:

$$\boldsymbol{r} u = \boldsymbol{k} = \boldsymbol{e} k \tag{C.13}$$

Relate with (C.9) and we have:

$$G^{-1} u = k, \quad G'^{-1} u' = k' \tag{C.14}$$

Then the cross product between $\boldsymbol{h}$ and $\boldsymbol{k}$, $\boldsymbol{h}'$ and $\boldsymbol{k}'$ are:

$$\boldsymbol{y} = \boldsymbol{h} \times \boldsymbol{k}, \quad \boldsymbol{y}' = \boldsymbol{h}' \times \boldsymbol{k}' \tag{C.15}$$

while the computation of cross product follows:

$$\boldsymbol{y} = \boldsymbol{h} \times \boldsymbol{k} = V \begin{vmatrix} \boldsymbol{r_1} & \boldsymbol{r_2} & \boldsymbol{r_3} \\ h_1 & h_2 & h_3 \\ k_1 & k_2 & k_3 \end{vmatrix} = V\boldsymbol{r}(h \times k) = V\boldsymbol{r}y \tag{C.16}$$

$$\boldsymbol{y}' = \boldsymbol{h}' \times \boldsymbol{k}' = V'\boldsymbol{r}'y' \tag{C.17}$$

V is the volume of the unit cell that is given by:

$$V^2 = det(G) \tag{C.18}$$

Together with (C.6), (C.10), (C.16), and (C.17) we have:

$$\boldsymbol{y}' = \lambda\mu\boldsymbol{y} \tag{C.19}$$

Combining with (C.16) and (C.17), there is:

$$\boldsymbol{r}'y' = \frac{\lambda\mu V}{V'}\boldsymbol{r}y \tag{C.20}$$

If we define:

$$\xi = \frac{\lambda\mu V}{V'} \tag{C.21}$$

Then equation (C.20) becomes:

$$\boldsymbol{r}'y' = \xi\boldsymbol{r}y \tag{C.21}$$

This is similar to (C.10) thus a relation like (C.11) can be acquired as:

$$XG'^{-1}y' = \xi G^{-1}y \tag{C.22}$$

From the three equations including (C.8), (C.11), and (C.22), OR transformation matrix X can be obtained with following equation after calculating λ, μ, ξ, y, y'.

$$X[h'\ G'^{-1}u'\ G'^{-1}y'] = [\ \boldsymbol{\lambda}h\ \mu G^{-1}u\ \xi G^{-1}y] \tag{C.23}$$

With this matrix, any direction in rutile, $[u;\ v;\ w]$, can be converted to gold with an index of $[u';\ v';\ w']$ that satisfies:

$$[\ u'; v'; w'] = X^{-1}\ [u; v; w] \tag{C.24}$$

And the transformation of lattice plane is given by:

$$[h'; k'; l'] = G'X^{-1}G^{-1}[h; k; l] \tag{C.25}$$